

Universidade Federal do Rio Grande – FURG

Instituto de Oceanografia

Programa de Pós-Graduação em Oceanologia

ÁGUAS INTERMEDIÁRIAS DO OCEANO AUSTRAL: ANÁLISE HISTÓRICA E PROJEÇÕES

LUCAS RODRIGUES DE ALMEIDA

Tese apresentada ao Programa de Pós-Graduação em Oceanologia, como parte dos requisitos para a obtenção do Título de Doutor.

Orientador: *Prof. Dr. MAURICIO MAGALHÃES MATA*

Universidade Federal do Rio Grande (FURG), Brasil.

Coorientador: *Dr. MATTHEW MAZLOFF*

Scripps Institution of Oceanography, University of California San Diego (UCSD), Estados Unidos

Rio Grande, RS, Brasil

Março 2022

ÁGUAS INTERMEDIÁRIAS DO OCEANO AUSTRAL: ANÁLISE HISTÓRICA E PROJEÇÕES

Tese apresentada ao Programa de Pós-Graduação em Oceanologia, como
parte dos requisitos para a obtenção do Título de Doutor

por

LUCAS RODRIGUES DE ALMEIDA

Rio Grande, RS, Brasil

Março 2022

© A cópia parcial e a citação de trechos desta tese são permitidas sobre a condição de que qualquer pessoa que a consulte reconheça os direitos autorais do autor. Nenhuma informação derivada direta ou indiretamente desta obra deve ser publicada sem o consentimento prévio e por escrito do autor.

RODRIGUES DE ALMEIDA, LUCAS
ÁGUAS INTERMEDIÁRIAS NO OCEANO AUSTRAL: ANÁLISE HISTÓRICA E
PROJEÇÕES FUTURAS / Lucas Rodrigues de Almeida. – Rio Grande:
FURG, 2022.140 p.

Tese – Universidade Federal do Rio Grande. Doutorado em Oceanologia. Área de Concentração: Oceanografia Física.

1. Oceano Austral. 2. Massas de Água. 3. Mudanças Climáticas.
**I. ÁGUAS INTERMEDIÁRIAS NO OCEANO AUSTRAL: ANÁLISE HISTÓRICA
E PROJEÇÕES FUTURAS.**



ATA ESPECIAL DE DEFESA DE TESE DE DOUTORADO – 02/2022

Às 14:00h do dia 21 de março do ano de dois mil e vinte e dois, por videoconferência, reuniu-se a Comissão Examinadora da Tese de **DOUTORADO** intitulada: "Águas intermediárias do oceano Austral: análise histórica e projeções, do Acad. Lucas Rodrigues de Almeida". A Comissão Examinadora foi composta pelos seguintes membros: Prof. Dr. Mauricio M. Mata – Orientador (IO/FURG), Prof. Dr. José Luiz Lima de Azevedo (IO/FURG), Prof. Dr. Rodrigo Kerr (IO/FURG) e Prof. Dr. Luciano Ponzi Pezzi (INPE). O Prof. Dr. Matthew R. Mazloff (Scripps Inst. of Oceanography - UCSD) atuou como coorientador da Tese, mas não participou da banca examinadora. Dando início à reunião, o Orientador e Presidente da sessão, Prof. Dr. Mauricio M. Mata, agradeceu a presença de todos e fez a apresentação da Comissão Examinadora. Logo após esclareceu que o Candidato teria um tempo de 45 a 60 min para explanação do tema, e cada membro da Comissão Examinadora, um tempo máximo de 30 min para perguntas e considerações. A seguir, passou a palavra ao Candidato, que apresentou o tema e respondeu às perguntas formuladas. Após ampla explanação, a Comissão Examinadora reuniu-se em reservado para discussão do conceito a ser atribuído ao Candidato. Foi estabelecido que as sugestões de todos os membros da Comissão Examinadora, que seguem em pareceres em anexo, foram aceitas pelo Orientador/Candidato para incorporação na versão final da Tese. Finalmente, a Comissão Examinadora considerou o candidato **APROVADO**, por unanimidade. Nada mais havendo a tratar, foi lavrada a presente ATA que, após lida e aprovada, será assinada pela Comissão Examinadora, pelo Candidato e pelo Coordenador do Programa de Pós-Graduação em Oceanologia.

Prof. Dr. Mauricio M. Mata
Presidente

Prof. Dr. Rodrigo Kerr
Prof. Dr. Luciano Ponzi Pezzi
Prof. Dr. Rodrigo Kerr
Coordenador PPGO
Prof. Dr. José Luiz L. de Azevedo
Acad. Lucas Rodrigues de Almeida

*“O que sabemos é uma gota, o que ignoramos é um oceano
Mas o que seria o oceano se não infinitas gotas? ”*

Isaac Newton

Agradecimentos

Este trabalho é o encerramento de mais uma importante etapa na minha vida e carreira acadêmica, que jamais seria concretizado apenas com duas mãos. Foi necessário uma série de pessoas que me influenciaram, ajudaram, ensinaram e apoiaram ao longo desta caminhada. E a todos, eu deixo aqui meu mais profundo agradecimento.

Ao longo da minha vida acadêmica tive a sorte de aprender com grandes professores e pesquisadores que me guiaram neste processo. O meu orientador, Prof. Dr. Mauricio Mata, a quem agradeço pela confiança, pelas oportunidades e por ter me ajudado ao longo destes quatro anos de trabalho com sua grande visão científica e suporte que foram essenciais para este projeto. Ao Prof. Dr. José Luiz, que me ensina e acompanha desde meus primeiros passos na iniciação científica. E agradeço ao Dr. Matthew Mazloff que me recebeu no exterior e muito contribuiu com os resultados aqui alcançados.

O ambiente acadêmico foi essencial para o desenvolvimento desta tese, seja através das aulas, dúvidas em apresentações ou conversas na hora do cafézinho. Neste sentido, agradeço à toda a equipe do LEOC, ao programa de pós-graduação em Oceanologia, a todos os profissionais da FURG e ao *Scripps Institution of Oceanography*, que me recebeu para o período do sanduíche.

Este caminho não foi trilhado apenas dentro da universidade e fora dela minha família sempre foi essencial. Meus agradecimentos a Ricardo, Rozana, Igor, Thales e Ana. Sem o apoio e suporte de vocês eu nada realizaria. Ficar longe de vocês é sempre a parte mais difícil.

Agradeço também a todos os amigos, seja nos momentos de descontração presencial ou reuniões online nestes novos tempos. Desocupar a mente às vezes também faz parte do desenvolvimento de um bom trabalho.

Muito obrigado a todos os membros da banca por aceitarem participar desta etapa final. A contribuição de vocês é valiosa para este trabalho.

Agradeço aos grupos que me proporcionaram grandes oportunidades nestes quatro anos: Grupo de Oceanografia de Altas Latitudes (GOAL), Southern Ocean Carbon and Climate Observations and Modeling (SOCCOM), Scientific Committee on Antarctic Research (SCAR). E à CAPES

(88887.368463/2019-00) pelo financiamento da bolsa de doutorado e CAPES/Print (88887.370051/2019-00) pelo financiamento do doutorado sanduíche.

Índice

Agradecimentos.....	viii
Índice.....	x
Lista de Figuras.....	xiii
Lista de Tabelas.....	xviii
Lista de Acrônimos, Abreviações.....	xix
Resumo.....	xxi
Abstract.....	xxiii
Capítulo I: Introdução.....	01
Capítulo II: Hipótese.....	09
Capítulo III: Objetivos.....	11
3.1. Objetivo.....	11
3.2. Objetivos específicos	11
Capítulo IV: Metodologia	13
4.1 Os Modelos Climáticos.....	13
4.2 Definição das Massas de Água.....	18
4.3 Fluxos na interface oceano-atmosfera.....	19
4.4 Análise Multivariada.....	20
Capítulo V: Transportes médios das AAIW/SAMW.....	24
5.1 Síntese do artigo.....	25
5.2 Artigo.....	27
5.2.1 Abstract.....	28

5.2.2 Plain Language Summary.....	29
5.2.3 Introduction.....	29
5.2.4 Material and Methods.....	33
5.2.4.1 Models.....	33
5.2.4.2 Definition of water masses.....	35
5.2.4.3 Ekman Pumping.....	37
5.2.4.4 Heat and Freshwater Fluxes.....	37
5.2.4.5 Multivariate Regression Procedure, Including Lags.....	38
5.2.3 Results.....	40
5.2.3.1 Mean State.....	40
5.2.3.2 Time Variability.....	44
5.2.5.3 Future Scenarios.....	52
5.2.5.4 Predictability.....	60
5.2.4 Conclusions.....	62
5.2.5 Acknowledgments.....	65
Capítulo VI: Análise Regional das AAIW/SAMW	66
6.1 Síntese do artigo.....	67
6.2 Artigo.....	68
6.2.1 Abstract.....	69
6.2.2 Plain Language Summary.....	70
6.2.3 Introduction.....	70
6.2.4 Material and Methods.....	72
6.2.4.1 Models.....	72

6.2.4.2 Definition of Water masses.....	74
6.2.4.3 Air-Sea Fluxes.....	76
6.2.4.4 Multivariate Regression.....	77
6.2.5 Results.....	79
6.2.5.1 SO characteristics.....	79
6.2.5.2 Regional Formation.....	82
6.2.5.3 Meridional Transports.....	87
6.2.5.4 Future Scenarios.....	89
6.2.6 Conclusions.....	93
6.2.7 Aknowledgments.....	97
Capítulo VII: Síntese da Discussão e conclusões.....	98
Capítulo VIII: Recomendações para trabalhos futuros.....	107
Referências Bibliográficas.....	109

Lista de Figuras

Figura 1.1. Esquema da circulação de revolvimento meridional (MOC) a partir de uma perspectiva do Oceano Austral, com as massas d'água que compõe cada camada desta cédula. Na camada intermediária (representada em vermelho) está presente a Água Modal Subantártica (*Subantarctic Mode Water* – SAMW), a Água Intermediária Antártica (*Antarctic Intermediate Water* – AAIW) e a Água Intermediária do Pacífico Norte (*North Pacific Intermediate Water* – NPIW), as águas da camada profunda são Água Profunda do Índico (*Indian Deep Water* – IDW) e a Água Profunda do Pacífico (*Pacific Deep Water* – PDW) ambas representadas em laranja, e em verde a Água Profunda do Atlântico Norte (*North Atlantic Deep Water* – NADW), e na camada de fundo está esquematizado em azul a Água de Fundo Antártica (*Antarctic Bottom Water* – AABW). Retirado de Talley, 2013.**2**

Figura 1.2. Esquema dos processos dominantes que ocorrem no Oceano Austral. Neste trabalho o foco é o ressurgimento das águas profundas na região Circumpolar, a atuação dos ventos e oeste combinados com os fluxos de calor oceano-atmosfera, que darão origem às águas intermediárias. Figura retirada de Talley 2013.**5**

Figura 1.3. Representado em vermelho está as regiões de subducção do Oceano Austral. As linhas em preto são as três principais frentes da ACC: PF, SAF e SAF-N. Figura retirada de Sallée et al. 2010..**6**

Figure 5.1. The upper three panels are the CMIP6 ensemble mean fluxes in the Southern Ocean calculated using the last 30 years of historical experiment. The top two are Ekman pumping and freshwater flux, and the mid panel is the heat flux. The lower panel is a schematic showing the mean fluxes, where W_{ek} is the mean Ekman transport of $-7.4 \cdot 10^{-7} \text{ cm s}^{-1}$, E is evaporation of $4.5 \cdot 10^{-6} \text{ Kg m}^{-2} \text{ s}^{-1}$, and H is the mean heat flux of 3.5 W m^{-2} . This lower panel gives a vertical perspective of Antarctic water masses and circulation, with an inflow of Circumpolar Deep Water (CDW) into the Southern Ocean and an export of

Antarctic Bottom Water (AABW), AAIW and SAMW. The CMIP6 models mean export of SAMW is 14 Sv and of AAIW is 7 Sv.....**31**

Figure 5.2. Mean water mass volume transports at 30°S for each model (units are Sv). Dark blue and light blue bars show the CMIP6 and CMIP5 models, respectively. The orange dashed line is the multimodel mean transport. The left panel shows AAIW transport and the right panel shows SAMW. The whiskers are the transports standard deviation. Mean correlations (R^2) between mean fluxes and mean transports across models are noted in the plot. Also included is the R^2 for the multivariate regression.....**40**

Figure 5.3. The mean air-sea fluxes between 30° - 55°S from historical and picontrol experiments for each model, normalized by the maximum value (-8.6x10⁻⁷ cm s⁻¹ for Ekman pumping from model BCC-CSM2-MR; -7.6x10⁻⁶ kg m⁻² s⁻¹ for freshwater from the model EC-Earth3-Veg and 6.19 W m⁻² for heat flux from MIROC6). The bars are the Ekman pumping (green), freshwater (blue) and heat (red) fluxes.....**43**

Figure 5.4. Lag correlations for Ekman pumping, freshwater and heat fluxes for each water mass, with AAIW (SAMW) displayed in the top (bottom) panels. Red lines are the model BCC-ESM1, green BCC-CSM2-MR, blue CAMS-CSM1-0, pink Can-ESM5, cyan GISS-E2-1-H, brown MIROC6 and in black SAM0-UNICON.....**45**

Figure 5.5. The upper two panels show the R^2 for each flux component to the respective water mass transports (AAIW on top and SAMW below). The multivariate correlation is in gray bars, and individual components are shown in green (Ekman pumping), blue (freshwater), and red (heat) bars. The bottom two panels show the same R^2 for the multivariate correlation in gray, and the R^2 for the partial correlations are given for each individual flux component in color.....**46**

Figure 5.6. Coefficients from the multivariate regression for each model analyzed, the green bar represents the coefficient for Ekman pumping, blue for

freshwater flux, and red for heat flux. AAIW is the top panel and SAMW below. The black contour represents the coefficients with partial correlations higher than 0.3 for models with multivariate R² values higher than 0.5.....51

Figure 5.7. 21st century projections for the fluxes considered in this study. Top to bottom: Ekman pumping, freshwater, and heat fluxes. The S4.5 scenario is shown in blue and the S8.5 in orange, with the shading denoting the ensemble standard deviation.53

Figure 5.8. Same as Figure 2, but for future projections. At the top (bottom) the S4.5 (RS8.5) scenario. The dark blue bars represent CMIP6 and the light blue CMIP5 models. The mean historical export for each model (Figure 2) are shown in gray bars. The average transports are highlighted in dashed orange lines, reaching values of 7.5~Sv for AAIW and 14~Sv for SAMW in S4.5, and values of 7.9~Sv for SAMW and 14.8~Sv in S8.5.....55

Figure 5.9. 21st century projections for transports of AAIW (top) and SAMW (bottom). The scenario S4.5 are presented on the left and S8.5 on the right. In blue are shown the exports calculated with temperature, salinity, and velocity outputs from future scenario experiment and in orange are the exports estimated for the future scenarios using the future fluxes and correlation coefficients derived from the PiControl/Historical. The shading gives the standard deviation of the ensemble.....56

Figure 5.10. Multivariate regression coefficients for each model analyzed in the future scenario runs. The green bars represent the coefficients for Ekman pumping, blue for freshwater flux, and red for heat flux. The top two panels are, respectively, AAIW and SAMW coefficients for S4.5; and the bottom two panels are the same but for S8.5 scenario. The bars with a black contour represent the coefficients with partial correlations higher than 0.3 and multivariate R² values higher than 0.5.....57

Figure 6.1. Cross-model mean of the air-sea fluxes between 30°S and 70°S. The green line denotes Ekman pumping ($m.s^{-1}$), the blue line represents the

freshwater flux ($\text{kg.m}^{-2}.\text{s}^{-1}$), and the red line represents the heat flux (W.m^{-2}). The shadows are the standard deviation for the respective color.....**76**

Figure 6.2. Winter mixed-layer depth (in meters) averaged over the historical experiment for each model, the last one is the winter mixed-layer estimated with the Argo climatology, using the September mean from 2004 to 2018.....**78**

Figure 6.3. The top two panels are the multi-model mean R^2 from the multivariate correlation for each water mass (AAIW left and SAMW right) using the historical experiment. The multivariate correlation are between the Export of each water masses and the combination of Ekman pumping, freshwater flux and heat flux. The bottom panels are the standard deviation between the R^2 result of each model.....**80**

Figure 6.4. The top three panels are the individual correlations of Ekman pumping, heat and freshwater fluxes with the export of AAIW. The bottom panels are the same correlation but with the SAMW transport.....**82**

Figure 6.5. The top two panels are the multi-model mean of meridional transport at 30°S in the layers of AAIW (top panel) and SAMW (middle panel), with positive values representing a northward export. The last panel is the difference between the transport of AAIW and SAMW. Each color represents one experiment, gray are historical, blue are SSP4.5 and orange are SSP8.5.....**84**

Figure 6.6. The top two panels are the multi-model mean R^2 from the multivariate correlation for each water masses (AAIW left and SAMW right) using the mitigation future scenario (SSP4.5). The multivariate correlation are between the Export of each water masses and the combination of Ekman pumping, freshwater and heat fluxes. The bottom panels are the difference between these R^2 and the

multivariate correlation in the historical experiment, where positive values means
a correlation increase for the future scenario.....**86**

Figure 6.7. The top two panels are the multi-model mean R^2 from the multivariate correlation for each water masses (AAIW left and SAMW right) using the mitigation future scenario (SSP8.5). The multivariate correlation are between the Export of each water masses and the combination of Ekman pumping, freshwater flux and heat flux. The bottom panels are the difference between these R^2 and the correlation in the historical experiment.....**88**

Listas de Tabelas

Tabela 4.1: Detalhamento dos modelos utilizados neste estudo. A primeira coluna é o nome do modelo. A segunda apresenta a sua geração, as colunas <i>Oceano</i> e <i>Atmosfera</i> as suas resoluções horizontais, enquanto a coluna <i>Vertical</i> indica o seu número de níveis verticais, a coluna seguinte é a instituição de origem do modelo e a última coluna traz uma referência de introdução ao modelo.....	14
Table 5.1. Climate Coupled Models used in this study. Some details for each model are presented: name, generation, ocean and atmospheric horizontal resolution, ocean vertical coordinate and number of levels (Z are traditional depth coordinates, Z* are re-scaled depth coordinates, S are sigma coordinates, and SZ are hybrids) and main reference.....	33
Table 5.2. Trends of water mass export for the future scenarios. AAIWm and SAMWm are the export trends calculated with temperature, salinity, and velocity model outputs from future scenario experiment (blue lines in Figure 11), while AAIWs and SAMWs are the export trends statistically estimated for the future scenarios using the future fluxes and correlation coefficients derived from the3PiControl/Historical (orange lines in Figure 11). The p-value of the trend fit is given in parentheses, with a value less than 0.05 implying significance.....	59
Table 6.1. Climate Coupled Models used in this study. Some details for each model are presented: name, ocean and atmospheric horizontal resolution, ocean vertical coordinate and number of levels, the origin institution and main reference.....	71

Lista de Acrônimos e Abreviações

A

AABW – Água de Fundo Antártica
(*Antarctic Bottom Water*)

AAIW – Água Intermediária Antártica
(*Antarctic Intermediate Water*)

ACC – Corrente Circumpolar
Antártica (*Antarctic Circumpolar
Current*)

C

CDW – Água Profunda Circumpolar
(*Circumpolar Deep Water*)

CMIP – Projeto de Intercomparação
de Modelos Acoplados (*Coupled
Model Intercomparison Project*)

E

ESM – Modelos do Sistema
Climático (*Climate and Earth System
Models*)

ENSO – El Nino Oscilação Sul (*El
Nino Southern Oscilation*)

G

GCM – Modelos Climáticos Globais
(*Global Climate Model*)

H

Historical – Cenário nos modelos
que comprehende o período atual
(1850 à 2015)

I

IDW – Água Profunda do Índico
(*Indian Deep Water*)

IPCC – Painel Intergovernamental
de Mudanças Climáticas
(*Intergovernmental Panel on Climate
Change*)

N

NPIW – Água Intermediária do
Pacífico Norte (*North Pacific
Intermediate Water*)

NADW – Água Profunda do Atlântico
Norte (*North Atlantic Deep Water*)

M

MOC – Célula de Revolvimento
Meridional (*Meridional Ocean
Circulation*)

MWFR – Regiões de Formação das Águas Modais (*Mode Water Formation Regions*)

MLD – Profundidade da Camada de Mistura (*Mixed Layer Deep*)

WCRP – Programa Mundial de Pesquisas Climáticas (*World Climate Research Programm*)

WGCM – Grupo de Trabalho de Modelos Acoplados (*Working Group on Coupled Modelling*)

P

PDW – Água Profunda do Pacífico (*Pacific Deep Water*)

PF – Frente Polar (*Polar Front*)

PiControl – Experimento pré-período da revolução industrial

PV – Vorticidade Potencial (*Potential Vorticity*)

R

RCP – Caminhos de Concentração Representativa (*Representative Concentration Pathways*)

S

SAMW – Água Modal Subantártica (*Subantarctic Mode Water*)

SSP – Caminhos Socioeconómicos Compartilhados (*Shared Socioeconomics Pathways*)

SO – Oceano Austral (*Southern Ocean*)

SAM – Modo Anular Sul (*Southern Annular Mode*)

W

Resumo

As massas de água denominadas Água Intermediária Antártica (AAIW) e Água Modal Subantártica (SAMW) são formadas em regiões específicas ao redor do oceano Austral pelo processo de subducção. A teoria prediz que, em decorrência da atuação intensa dos ventos de oeste, combinado com perda de flutuabilidade, essas águas afundam para abaixo da camada de mistura e ventilam as regiões subtropicais do hemisfério sul, levando consigo grandes quantidades de calor e gás carbônico, sendo um processo chave para o sistema climático global. Neste estudo, é investigado como os modelos do Projeto de Intercomparação de Modelos Acoplados (CMIP) estão representando estas massas de água, focando nos processos envolvidos na sua variabilidade temporal e também nas regiões onde estas águas são formadas no oceano Austral. Para isto foram analisados os transportes de volume das AAIW/SAMW em 30°S e os fluxos oceano-atmosfera envolvidos neste processo (i.e., bombeamento de Ekman, fluxo de calor e de água doce), levando em conta tanto suas variações ao longo do tempo como suas distribuições espaciais. Foi encontrada uma alta variabilidade na intensidade dos transportes entre os modelos, sendo que a maioria superestima estes valores quando comparado com dados obtidos *in situ*. Através de uma correlação multivariada, foi demonstrado que as variabilidades destas massas de água são melhores explicadas utilizando os três fluxos em conjunto e os coeficientes resultantes destas análises são não-estacionários, variando ao longo do tempo, o que significa que eles inclusive alternam de dominância quando considerados em cenários climáticos futuros. Em relação às regiões de formação das massas de água, foi encontrada uma acurada performance dos modelos, considerando que na maioria destes elas se formam nas regiões apontadas em estudos observacionais: leste do setor Índico, Passagem de Drake e ao sul da África. E então, elas são exportadas para norte, principalmente pelas bordas dos três grandes oceanos, acompanhando a circulação dominante. Essas áreas não parecem mudar nos cenários futuros, apresentando apenas um pequeno decréscimo nos coeficientes das correlações multivariadas. Portanto, apesar de os modelos ainda apresentarem algumas carências nas representações das exportações das AAIW/SAMW, eles parecem formar estas

massas de água nas regiões corretas e seguindo a relação com os fluxos oceano-atmosfera esperados.

Palavras-Chave: Oceano Austral, MOC, Circulação Oceânica, Massas de Água, Modelos Climáticos, AAIW, SAMW.

Abstract

Subduction in the Antarctic circumpolar region of the Southern Ocean (SO) results in the formation of Antarctic Intermediate Water (AAIW) and Subantarctic Mode Water (SAMW). The AAIW/SAMW are formed in specific regions of the SO as a result from the combination of intense winds and buoyancy fluxes which lead to thick mixed layers and thus subduction. The objective of this study is to evaluate the extent to which AAIW and SAMW temporal and spatial variability are correlated to Southern Ocean air-sea fluxes (Ekman pumping, freshwater and heat fluxes), using the Coupled Model Intercomparison Project (CMIP). The main focus is to explore how potential changes to those forcings would impact the future water mass export rates. In this sense, the export of these water masses vary across models, with most overestimating the total transport when compared to the climatology. Correlation coefficients between the air-sea fluxes and exports are consistent with theoretical expectations. Moreover, multivariate regressions show that both AAIW and SAMW export variability are better explained using the combination of all three fluxes, but the dominant forcing components were found to be non-stationary, changing from the present simulations to the future scenario runs (i.e. end of XXI century). It was identified that the highest correlations are found in the eastern Indian sector of the SO. The results also show high correlations to air-sea fluxes close to Drake Passage and south of Africa, suggesting a good representation of AAIW/SAMW formation regions in CMIP6 models when compared to climatology. The future scenarios depict the same pattern of formation regions when compared to the historical runs, but with a slight correlation coefficient decrease as time progresses towards year 2100.

Keywords: Southern Ocean, MOC, Water mass, Ocean Circulation, Climate Model

Capítulo I: Introdução

1.1 O oceano Austral e o clima

Os oceanos possuem um importante papel na dinâmica climática global, transportando calor entre diferentes regiões do planeta. Este transporte ocorre de duas formas: superficialmente pelos grandes giros oceânicos, responsáveis por levar calor das regiões tropicais para as polares, e nas camadas mais profundas, através da chamada circulação termohalina ou Célula de Revolvimento Meridional (*Meridional Overturning Circulation* - MOC), formada por águas afundadas nas regiões de altas latitudes e que dominam das profundidades intermediárias até as camadas abissais dos oceanos [Talley, 2013]. A intensidade da MOC está diretamente ligada à capacidade do oceano de absorver e armazenar calor, carbono antropogênico e demais gases. Associado a esta circulação, o oceano armazenou cerca de 85% do aumento total de calor observado na Terra desde a segunda metade do século XX, o que impediu um maior aquecimento dos baixos níveis da atmosfera [Levitus et al. 2005]. Além

disso, o afundamento das águas intermediárias, profundas e de fundo, nas regiões de altas latitudes, captura e armazena grandes quantidades de CO₂ por parte das águas, diminuindo a concentração deste gás na atmosfera [Sabine et al. 2004]. A Figura 1.1 apresenta um esquema da circulação da MOC e as respectivas massas de água para cada bacia oceânica. Mudanças nos padrões da MOC têm sido associados com drásticas mudanças climáticas [Clark et al. 2002] e, portanto, um profundo entendimento de seus padrões e consequências é fundamental para estudos dos processos climáticos planetários.

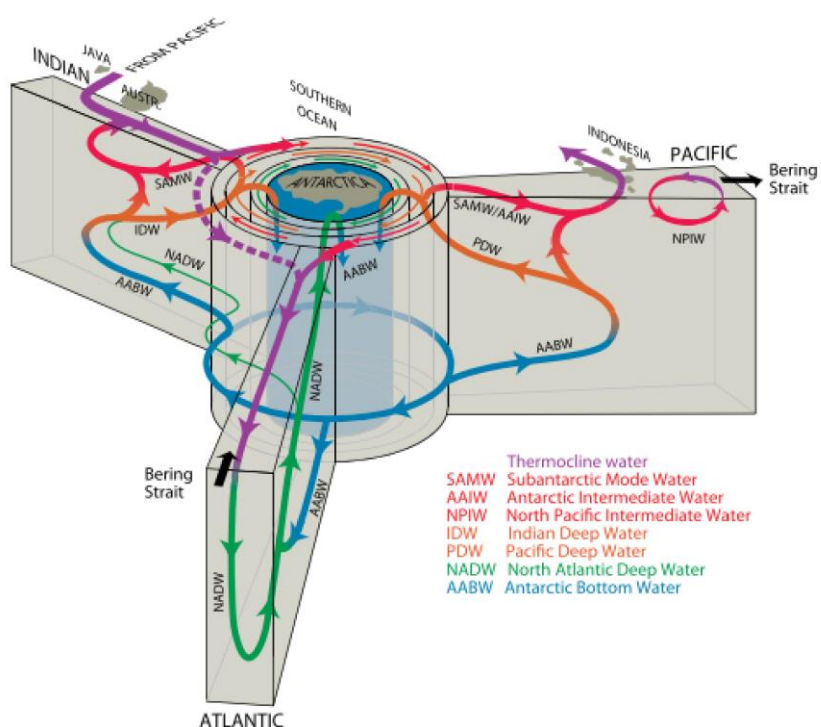


Figura 1.1. Esquema da circulação de revolvimento meridional (MOC) a partir de uma perspectiva do oceano Austral, com as massas d'água que compõe cada camada desta cédula. Na camada intermediária (representada em vermelho) está presente a Água Modal Subantártica (*Subantarctic Mode Water* – SAMW), a Água Intermediária Antártica (*Antarctic Intermediate Water* – AAIW) e a Água Intermediária do Pacífico Norte (*North Pacific Intermediate Water* – NPIW), as águas da camada profunda são Água Profunda do Índico (*Indian Deep Water* – IDW) e a Água Profunda do Pacífico (*Pacific Deep Water* – PDW) ambas representadas em laranja, e em verde a Água Profunda do Atlântico Norte (*North Atlantic Deep Water* – NADW), e na camada

de fundo está esquematizado em azul a Água de Fundo Antártica (*Antarctic Bottom Water* – AABW). Retirado de [Talley, 2013](#).

Como destacado na Figura 1.1, o oceano Austral, região ao sul da Frente Subantártica, tem um papel fundamental na circulação da MOC e, de acordo com [Roemmich et al. \[2015\]](#), é nele que ocorreu entre 67 – 98% do aumento de conteúdo de calor nos oceanos globais, alterando significativamente as propriedades físico-química das águas desta região. Neste mesmo contexto, em outro processo fundamental para o equilíbrio climático do planeta, é próximo às plataformas do continente Antártico que águas de menor temperatura da região serão bombeadas para o fundo dando origem a Água de Fundo Antártica (*Antarctic Bottom Water* – AABW), através do processo de convecção profunda [[Gordon 1986](#)]. Diversos estudos têm reportado mudanças nas características da AABW, como redução na sua salinidade e na densidade [e.g. [Azaneu et al. 2013](#), [Talley 2013](#), [Dotto et al. 2016](#)], potencialmente impactando as características globais da MOC.

Na região circumpolar antártica, a atuação persistente dos ventos de oeste combinada com fluxos de calor na interface ar-mar, onde as águas perderão calor para a atmosfera, resultando em densidades maiores. Dando origem às massas de água da camada intermediária dos oceanos do hemisfério sul, a Água Modal Subantártica (*Subantarctic Mode Water* – SAMW) e a Água Intermediária Antártica (*Antarctic Intermediate Water* – AAIW), através do processo chamado de subducção [[Sallée et al. 2010](#)]. Diversos estudos também têm reportado alterações nestas águas, como aquecimento e aprofundamento nas últimas décadas [e.g. [Gao et al. 2018](#); [Qu et al. 2020](#)]. Porém, apesar de sua importância para o sistema climático sendo um grande reservatório de calor e dióxido de

carbono e ocupar a célula superior da MOC, os processos de formação destas massas de água da camada intermediária e as possíveis mudanças em suas características ainda são pouco estudados e não são completamente entendidos. Desta forma, o aumento do conhecimento do comportamento e variabilidade destas massas de água e dos processos associados no contexto acima são o foco principal do presente estudo.

1.2 As Águas Intermediárias do oceano Austral

A camada profunda da MOC é caracterizada principalmente por um escoamento profundo para sul de águas provenientes do hemisfério norte, massa d'água denominada de Água Profunda do Atlântico Norte (APAN; ou *North Atlantic Deep Water - NADW*). Ao chegar no oceano Austral, estas águas entram no regime da Corrente Circumpolar Antártica (*Antarctic Circumpolar Current - ACC*), onde se misturam e se transformam, passando a receber a denominação de Água Circumpolar Profunda (*Circumpolar Deep Water – CDW*). Ao encontrarem águas mais frias elas serão advectadas para profundidades menores, até ressurgirem na superfície, processo que ocorre em torno de 60°S [Talley 2011]. Nesta região há uma atuação constante dos ventos de oeste, que induzem transporte de Ekman direcionado para norte, como demonstrado no esquema da Figura 1.2. Combinado com este transporte causado pelo vento, essas águas perdem calor para atmosfera e tenderão a afundar até ocuparem seu estrato de densidade na camada intermediária [Marshal & Radko, 2013]. Quando o processo de subducção é intenso o suficiente para bombear estas águas abaixo da profundidade da camada de mistura, elas darão origem às massas de água

AAIW e SAMW, processo que ocorre predominantemente durante o inverno do hemisfério sul [Sallée et al. 2010].

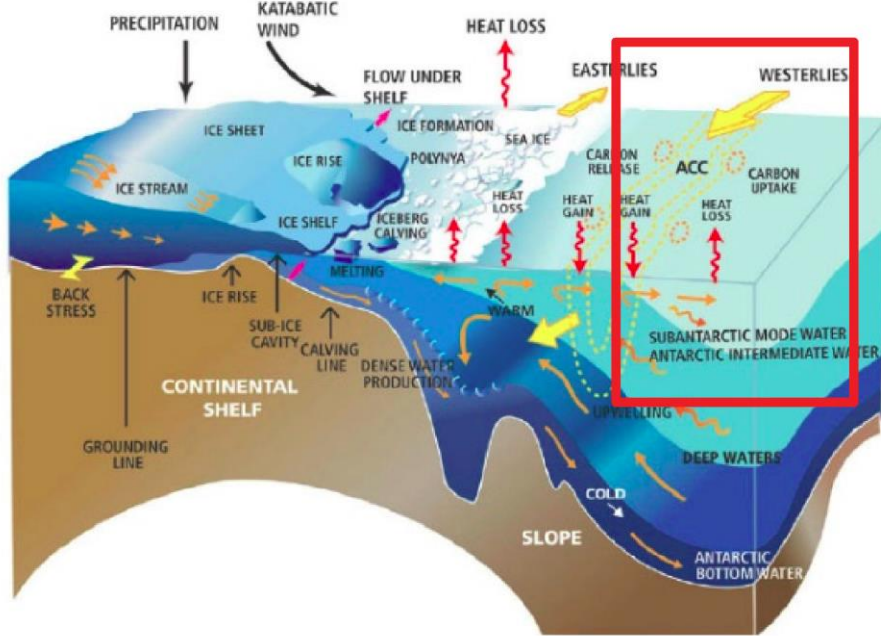


Figura 1.2. Esquema dos processos dominantes que ocorrem no oceano Austral. Incluindo o ressurgimento das águas profundas na região Circumpolar, a atuação dos ventos e oeste combinados com os fluxos de calor oceano-atmosfera, que darão origem às águas intermediárias, estes processos estão destacados pelo retângulo vermelho. Figura adaptada de [Talley \[2013\]](#).

De acordo com [McCarthy et al. \[2017\]](#) este processo de formação das massas de água tem origem ao sul da Frente Polar (*Polar Front – PF*), como destacado na Figura 1.3, que apresenta as principais zonas frontais do oceano Austral e as regiões de subducção. Outros trabalhos acrescentam que a formação destas massas d'água ocorrem entre a PF e a Frente Subantártica [e.g. [Rintoul & Bullister, 1999](#); [Hartin et al. 2011](#)]. Nestas regiões, em cada bacia oceânica, as águas tendem a diminuir de temperatura de oeste para leste. Logo possuem maiores densidades na porção oeste dos oceanos, onde tenderão a formar as

massas de água intermediárias, sendo que a SAMW será originada um pouco ao norte da AAIW [Sallée et al. 2010]. Diversos estudos têm identificado o sudeste dos oceanos Atlântico, Pacífico e Índico como regiões chave na formação destas massas de água [e.g. Hartin et al. 2011; Gao et al. 2018; Boland et al. 2021].

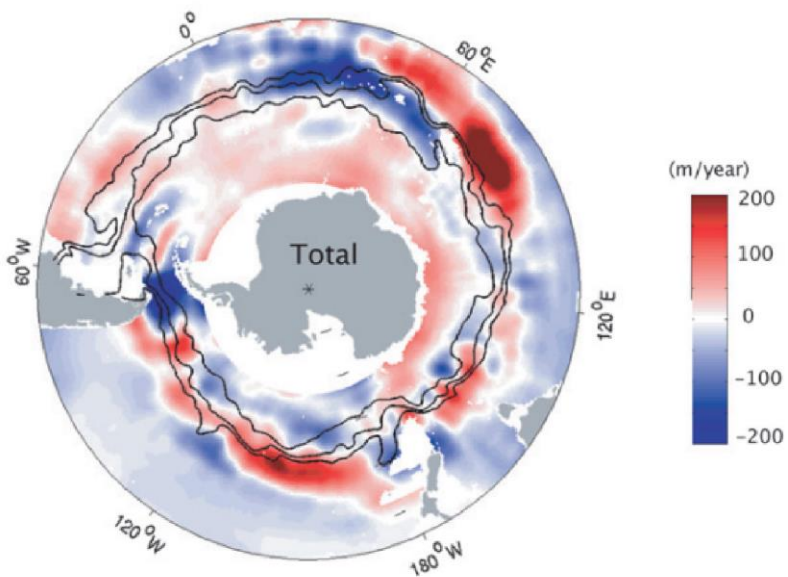


Figura 1.3. A figura representa as velocidades verticais no Oceano Austral, onde em vermelho estão as regiões de subdução e em azul as áreas de ressurgência. As linhas em preto são as três principais frentes da ACC: Frente Subantártica Norte, Frente Subantártica e Frente Polar, em ordem de norte a sul. Figura retirada de Sallée et al. [2010].

As águas AAIW/SAMW possuem um papel vital no sistema climático, seja por serem o principal componente da célula superior da MOC, mas também pela sua característica de absorver e armazenar carbono, oxigênio e calor da atmosfera e transportá-los da superfície para o interior dos oceanos [e.g. MacCarthy 1977; 1982; Roemmich et al. 2015; Gao et al. 2018]. Suas formações, distribuições e características têm sido estudadas em trabalhos passados, principalmente, com

dados *in situ* [e.g. [Sallée et al. 2010](#); [Hartin et al. 2011](#); [Boland et al. 2021](#)].

Estima-se que apenas durante o período de monitoramento pós implementação do programa de flutuadores autônomos ARGO (www.argo.ucsd.edu), estas massas d'água apresentaram mudanças em profundidade, volume e conteúdo de calor [e.g. [Gao et al. 2018](#); [Meijers et al. 2019](#); [Qu et al. 2020](#)]. Com isto, e dada sua importância no contexto terrestre explicada anteriormente, se faz necessário melhorar o conhecimento de quais as consequências das mudanças climáticas sobre os padrões destas massas de água e como possíveis mudanças nestes padrões destas águas podem interagir com o clima global.

Devido às condições extremas e dificuldade de amostragem do oceano Austral, combinado com o curto período de tempo de monitoramento da região, a realização das análises deste trabalho depende do uso de modelos climáticos globais (*Global Climate Models – GCMs*). Estes modelos são ferramentas que possibilitam uma resolução espacial e temporal necessária para analisar a variabilidade natural do sistema climático terrestre, particularmente do transporte de massas de água, com a realização de estimativas de suas características e variabilidades em diferentes cenários de mudanças climáticas. Neste trabalho será utilizado uma série de GCM's que fazem parte do *Coupled Model Intercomparison Project* (CMIP)¹, tanto da geração 5 (CMIP5) como os da mais nova geração (CMIP6). Com os experimentos destes modelos é possível simular os processos de circulação oceânica e atmosférica anterior ao período pré-industrial, com os modelos apresentando de 500 a 2000 anos antes de 1860, simular também o período atual, chamado de histórico, que compreende de 1860 até 2016. Desta forma, é obtido tanto a oscilação natural do sistema como o comportamento dos processos de interesse no oceano Austral nestas escalas.

Além disso, são utilizadas projeções destes modelos para, então, verificar os efeitos das mudanças climáticas sobre estes processos, nos quatro principais cenários possíveis considerados pelo último relatório do IPCC (*Intergovernmental Panel on Climate Change*) testados nestes modelos, com situações otimistas até possibilidades mais catastróficas [IPCC, 2014].

1.4 Estrutura da tese

Este documento terá seguimento da seguinte forma: no próximo capítulo (capítulo 2) será detalhada a hipótese que guia este trabalho e a seguir (capítulo 3) os objetivos. No Capítulo 4 é descrita toda a metodologia para alcançar os resultados mostrados nesta tese. Este documento é apresentado no formato de artigos científicos, apresentados nos Capítulos 5 e 6. O primeiro artigo investiga a importância dos fluxos oceano-atmosfera para o transporte das AAIW/SAMW, como este transporte está oscilando e a evolução dos modelos geração 6 do CMIP em relação àqueles da geração 5. No segundo artigo é investigado as regiões de formação de cada massa de água em todo oceano Austral e analisado suas mudanças nos futuros cenários de mudanças climáticas. O Capítulo 7, por sua vez, apresenta uma síntese da discussão dos principais aspectos deste estudo, junto das principais conclusões. E, por fim, no Capítulo 8 são apresentadas algumas sugestões para trabalhos futuros.

Capítulo II: Hipótese

Levando em consideração o cenário atual de mudanças climáticas, a especial sensibilidade do oceano Austral a este processo e, associado a isto, a importância que as massas de água da camada intermediária possuem no sistema climático, a hipótese deste trabalho é:

“O bombeamento de Ekman e fluxos de calor e água doce na interface oceano-atmosfera, que influenciam a formação e transporte das massas de água AAIW e SAMW, estão sendo significativamente impactados pelas mudanças climáticas

em curso. E consequentemente, alterando os transportes de volume destas massas de água exportadas do oceano Austral. ”

Capítulo III: Objetivos

3.1 Objetivo

O objetivo geral desta tese é quantificar o quanto a variabilidade dos transportes das massas de água AAIW e SAMW respondem aos principais fluxos oceano-atmosfera, bombeamento de Ekman, calor e água doce. E identificar as principais regiões que estas massas de água se formam no Oceano Austral. Por fim verificar como estes processos podem estar sendo impactados pelas mudanças climáticas em curso.

3.2 Objetivos específicos

- Estimar a variabilidade temporal do transporte de volume das AAIW/SAMW;

- Quantificar o impacto da variabilidade do bombeamento de Ekman, fluxo de calor e fluxo de água doce na variabilidade dos transportes de volume das águas da camada intermediária do oceano Austral;
- Estimar a evolução da representação destas massas de água entre as gerações 5 e 6 dos modelos CMIP;
- Localizar as regiões preferenciais de formação destas massas de água nos modelos CMIP;
- Estimar e quantificar as consequências das mudanças climáticas no transporte de volume da AAIW e SAMW ao longo do século XXI.

Capítulo IV: Metodologia

4.1 Os Modelos Climáticos

No contexto da hipótese deste trabalho, desde 2008, um grupo de trabalho do Programa Mundial de Pesquisas Climáticas (WCRP) chamado de *Working Group on Coupled Modelling* (WGCM), que envolve mais de 20 equipes de modelagem dos principais centros de previsão de tempo e clima no mundo, coordena os experimentos de modelagem climática, resultando no CMIP. A cada nova geração de modelos, os seus desenvolvedores levam em consideração os problemas que foram levantados em artigos científicos sobre o tema e o avanço da tecnologia para que o modelo apresente uma representação cada vez mais próxima ao oceano real. Atualmente, os modelos estão na geração 6 (CMIP6).

Neste trabalho são utilizados modelos desta nova geração e também outros da geração anterior (CMIP5) para possibilitar avaliar a evolução entre estas gerações de modelos. No total, são utilizados 35 modelos, apresentados com mais detalhes na Tabela 4.1. Os modelos obedecem aos mesmos padrões de saída de dados e realizam os mesmos experimentos. O propósito destes experimentos é responder questões científicas levantadas nos relatórios do IPCC [Taylor et al. 2009] como, por exemplo, entender mais profundamente o sistema climático e os processos responsáveis por suas mudanças e variabilidade.

Neste trabalho são utilizados os experimentos de longo período do CMIP, chamados de multicentenário de controle pré-industrial (*PiControl*) para quantificar a variabilidade dos processos citados anteriormente. Nestes experimentos, há modelos com alcance temporal de 250 até 1750 anos. A seguir são utilizados os experimentos chamados de decadais ou *Historical*, que compreendem os anos 1860 até 2005 (CMIP5), ou até 2016 (CMIP6). Com estes experimentos é possível verificar quais modelos estão representando os processos atuais de forma acurada e como suas variabilidades já estão sentindo os efeitos das mudanças do clima ao longo do século XX. A série temporal tem resolução mensal, compreendendo o número de anos que cada modelo fornece. A resolução espacial dos modelos é variável, sendo que a maioria dos modelos CMIP5 apresenta uma resolução horizontal oceânica em torno de $2^\circ \times 2^\circ$ (longitude x latitude), enquanto para os modelos CMIP6 é de em torno de $1^\circ \times 1^\circ$. No entanto, alguns possuem resolução um pouco mais refinada conforme especificado na Tabela 4.1. A resolução não ser padrão pode ser um importante fator na avaliação de quais modelos representarão a circulação no oceano

Austral mais próximo ao oceano real. Por exemplo, Heywood et al. [2014] apontam que os modelos climáticos apresentam dificuldade em representar alguns processos na plataforma Antártica devido às suas baixas resoluções espaciais.

Tabela 4.1: Detalhamento dos modelos utilizados neste estudo. A primeira coluna é o nome do modelo. A segunda apresenta a sua geração, as colunas *Oceano* e *Atmosfera* as suas resoluções horizontais, enquanto a coluna *Vertical* indica o seu número de níveis verticais, a coluna seguinte é a instituição de origem do modelo e a última coluna traz uma referência de introdução ao modelo.

Modelo	Geração	Oceano	Atmosfera	Vertical	Instituição	Referência
ACCESS1-0	CMIP5	1.88° x1.24°	1.88° x1.25°	50	CSIRO	Collier & Uhe (2012)
ACCESS1-3	CMIP5	1.88° x1.24°	1.92° x1.45°	50	CSIRO	Collier & Uhe (2012)
ACCESS-CM2	CMIP6	1.00° x1.00°	1.88° x1.25°	50	CSIRO	Dix et al., 2019
ACCESS-ESM1-5	CMIP6	1.00° x1.00°	1.88° x1.25°	50	CSIRO	Ziehn et al., (2019)
BCC-CSM2-MR	CMIP6	1.00° x1.00°	1.12° x1.10°	40	BCC	Wu et al., (2018)
BCC-ESM1	CMIP6	1.00° x1.00°	2.81° x2.81°	40	BCC	Zhang et al., (2018)
CAMS-CSM1-0	CMIP6	1.00° x1.00°	1.00° x1.00°	50	CAMS	Rong (2019)
CanESM2	CMIP5	2.81° x2.81°	2.81° x2.81°	40	CCCma	CCCM & CCCm (2015)
CanESM5	CMIP6	1.00° x1.00°	2.81° x2.81°	45	CCCma	Swart et al., (2019)
CanESM5-CanOE	CMIP6	1.00° x1.00°	2.81° x2.81°	45	CCCma	Swart et al., (2019)
CESM2	CMIP6	1.12° x0.46°	0.90° x1.25°	60	CESM	Danabasoglu et al., (2019)
CMCC-CM2-SR5	CMIP6	1.00° x1.00°	1.12° x1.12°	50	CMCC	Cherchi et al., (2019)
CNRM-CM5	CMIP6	1.41° x1.41°	1.41° x1.41°	42	CERFACS	Volodire et al., (2013)

CNRM-CM6-1	CMIP6	$1.00^\circ \times 1.00^\circ$	$1.40^\circ \times 1.40^\circ$	75	CERFACS	Voldoire (2018)
CNRM-ESM2-1	CMIP6	$1.00^\circ \times 1.00^\circ$	$1.40^\circ \times 1.40^\circ$	75	CERFACS	Seferian (2018)
CSIRO-Mk3.6.0	CMIP5	$1.88^\circ \times 1.88^\circ$	$1.87^\circ \times 1.87^\circ$	31	CSIRO	Jeffrey et al., (2013)
EC-Earth-Veg	CMIP6	$1.00^\circ \times 1.00^\circ$	$0.70^\circ \times 0.70^\circ$	75	EC-Earth	EC-Earth (2019)
GFDL-ESM2G	CMIP5	$2.50^\circ \times 2.00^\circ$	$2.50^\circ \times 2.00^\circ$	63	NOAA GFDL	Dunne et al., (2014)
GFDL-ESM2M	CMIP5	$2.50^\circ \times 2.00^\circ$	$2.50^\circ \times 2.00^\circ$	50	NOAA GFDL	GFDL (2018)
GISS-E2-1-G	CMIP6	$1.25^\circ \times 1.00^\circ$	$2.50^\circ \times 2.00^\circ$	32	GISS	NASA/GISS (2018)
GISS-E2-1-H	CMIP6	$1.00^\circ \times 1.00^\circ$	$2.50^\circ \times 2.00^\circ$	32	GISS	NASA/GISS (2018)
HadGEM2-ES	CMIP5	$1.88^\circ \times 1.25^\circ$	$1.88^\circ \times 1.25^\circ$	40	MOHC/UK	Meto e Rede Clima (2013)
INM-CM4-8	CMIP6	$1.00^\circ \times 0.56^\circ$	$2.00^\circ \times 1.50^\circ$	48	INM	Volodin et al., (2019)
INM-CM4	CMIP5	$2.00^\circ \times 1.50^\circ$	$2.00^\circ \times 1.50^\circ$	40	INM	Volodin et al., (2010)
MIROC5	CMIP5	$1.41^\circ \times 1.41^\circ$	$1.41^\circ \times 1.41^\circ$	50	AORI	AORI et al., (2013)
MIROC6	CMIP6	$1.00^\circ \times 0.70^\circ$	$0.70^\circ \times 0.70^\circ$	62	AORI	Tatebe & Watanabe (2018)
MIROC-ESM	CMIP5	$2.81^\circ \times 2.81^\circ$	$2.81^\circ \times 2.81^\circ$	44	AORI	Watanabe et al., (2011)
MPI-ESM1-2-HR	CMIP6	$0.44^\circ \times 0.44^\circ$	$0.94^\circ \times 0.94^\circ$	40	MPI	Schupfner et al., (2019)
MPI-ESM1-2-LR	CMIP6	$0.40^\circ \times 0.40^\circ$	$2.00^\circ \times 2.00^\circ$	40	MPI	Mauritzen et al., (2019)
MPI-ESM-LR	CMIP5	$1.88^\circ \times 1.88^\circ$	$1.88^\circ \times 1.88^\circ$	40	MPI	Giorgetta et al., (2012)
MRI-CGCM3	CMIP5	$1.13^\circ \times 1.13^\circ$	$1.13^\circ \times 1.13^\circ$	50	MRI	Yukimoto et al., (2012)
MRI-ESM2-0	CMIP6	$1.00^\circ \times 0.50^\circ$	$1.13^\circ \times 1.13^\circ$	61	MRI	Yukimoto et al., (2019)

NESM3	CMIP6	$0.98^\circ \times 0.49^\circ$	$1.90^\circ \times 1.90^\circ$	46	NUIST	Cao et al., (2018)
SAM0-UNICON	CMIP6	$1.12^\circ \times 0.47^\circ$	$1.24^\circ \times 0.94^\circ$	60	SNU	Park & Shin (2019)
UKESM1-0-LL	CMIP6	$1.00^\circ \times 1.00^\circ$	$1.88^\circ \times 1.25^\circ$	75	MOHC/UK	Tang et al., 2019

Para avaliar os possíveis efeitos das mudanças climáticas nos processos de interesse, são utilizados dois cenários futuros para cada geração de modelos.

Para o CMIP5, os cenários futuros são chamados de RCP's (*Representative Concentration Pathways*; [Taylor et al. 2012](#)), e aqui foram utilizados o RCP4.5, considerado o cenário em que são realizadas mitigações, e o RCP8.5, considerado o cenário mais catastrófico. Para os modelos CMIP6, os cenários futuros são chamados de SSP's (*Shared Socioeconomics Pathways*; [Eyring et al. 2016](#)), e são utilizadas as mesmas definições de cenários referentes ao CMIP5, porém denominadas de SSP4.5 e SSP8.5. Os cenários fornecem uma estimativa para a forçante radioativa até o ano 2100, tendo como referência as condições pré-industriais. Os cenários que contam com atividades de mitigação, sendo considerados os mais otimistas (RCP4.5 e SSP4.5), são aqueles que as forçantes radioativas chegariam a um máximo no meio do século XXI e estabilizariam em $4,5 \text{ W m}^{-2}$. Os outros dois cenários catastróficos (RCP8.5 e SSP8.5) apresentam um mecanismo semelhante, mas estabilizam em $8,5 \text{ W.m}^{-2}$ [\[Taylor et al. 2012\]](#) em meados deste século. Assim, é possível avaliar quais as possíveis consequências sobre a circulação no oceano Austral que as mudanças climáticas estão causando e ainda podem vir a causar.

4.2 Definição das Massas de Água

As massas de água AAIW e SAMW representadas nos modelos CMIP, podem apresentar valores de densidade diferentes do real no oceano, por isso é necessário identificar as características das massas de água em cada modelo de maneira padronizada. Para realizar esta identificação, neste trabalho foi aplicada a metodologia apresentada por [Sallée et al. \[2013\]](#), que define as massas de água exportadas a partir de propriedades hidrográficas. A AAIW está associada com a mínima salinidade no cinturão circumpolar [[Tomczak et al. 2007](#)], e a SAMW com estratificação mínima, logo associado a uma baixa Vorticidade Potencial (*Potential Vorticity – PV*).

Para delimitar os limites superior e inferior da AAIW é identificada a salinidade mínima local em cada perfil (S_{min}) e a salinidade máxima logo acima ($S_{max(acima)}$) e abaixo ($S_{max(abaixo)}$). Os limites da AAIW serão definidos em termos de densidade, com um quarto da distância entre S_{min} e $S_{max(acima)}$ para o limite superior da massa de água, e um quarto da distância entre S_{min} e $S_{max(abaixo)}$ para o limite inferior. As Equações 1 e 2 abaixo detalham o critério adotado:

$$\sigma_2(acima) = (3\sigma_2(S_{min}) + \sigma_2(S_{max(acima)})) / 4 \quad (1)$$

$$\sigma_2(abaixo) = (3\sigma_2(S_{min}) + \sigma_2(S_{max(abaixo)})) / 4 \quad (2)$$

Os volumes de transporte das massas de água foram calculados para cada longitude ao longo de todo o perfil de 30°S. Logo, os limites das densidades foram utilizados para delimitar a área da massa de água, a qual multiplicada

pelas velocidades meridionais é possível obter o transporte total de volume de água apresentados em Sv (1 Sverdrup $\equiv 10^6 \text{ m}^3 \text{ s}^{-1}$).

No caso da SAMW, que está diretamente associada a um mínimo de PV na coluna d'água logo acima da AAIW, primeiramente foi definido o limite superior da AAIW como o limite inferior da SAMW. A seguir, foi localizado o PV mínimo associado com uma diferença vertical de densidade menor do que $0,03 \text{ kg m}^{-3}$ em relação à superfície. Então o limite superior da SAMW foi definido como contendo pelo menos 90% do total do mínimo local de PV. Após identificar os limites superiores e inferiores foi calculado o transporte total através das velocidades meridionais para cada modelo, assim como no caso da AAIW. Todo este processo foi realizado para cada modelo e em cada um dos experimentos utilizados neste estudo.

4.3 Fluxos na interface oceano-atmosfera

Todos os fluxos foram calculados para cada mês e em cada ponto de grade de cada modelo entre as latitudes de 30°S e 70°S . O bombeamento de Ekman, W_e (cm s^{-1}), foi calculado a partir dos ventos zonais na região circumpolar, sendo que todos os modelos utilizados a tensão de cisalhamento (stress) do vento na superfície como uma de suas saídas. As velocidades verticais foram calculadas a partir da Equação 3, mostrada a seguir, onde τ é o stress do vento, ρ_o é a densidade de referência da água do mar e f é o parâmetro de Coriolis.

$$W_e = \nabla \times \left(\frac{\tau}{\rho f} \right) \quad (3)$$

Para o cálculo do fluxo total de calor, Q (W m^{-2}), foi somado o fluxo de cada componente fornecido pelos modelos, que incluem os fluxos de calor sensível ($hfss$) e latente ($hfsl$), a radiação de onda longa, nos sentidos para cima ($rlds$) e

para baixo ($rlus$), e a radiação de onda curta, também nos sentidos para cima ($rsds$) e para baixo ($rsus$). Neste trabalho foi seguida a convenção de Q positivo significa fluxo de calor para o oceano. A soma dos fluxos de calor é mostrada na Equação 4:

$$Q = -hfss - hfls + rlds - rlus + rsds - rsus \quad (4)$$

O fluxo de água doce, F ($\text{kg m}^{-2} \text{s}^{-1}$), é calculado pelo balanço direto entre precipitação (P) e evaporação (E), conforme demonstrado na Equação 5. Logo, neste trabalho, um F positivo representa uma maior entrada de água doce no oceano, diminuindo a salinidade local.

$$F = P - E \quad (5)$$

4.4 Análise Multivariada

Primeiramente, para permitir a comparação entre variáveis com diferentes magnitudes, as séries temporais dos três fluxos (bombeamento de Ekman, água doce e calor) e da exportação das massas de água foram normalizadas retirando a média de cada variável, e foi dividido o resultado pelo desvio padrão da série.

Após, foi computada uma regressão multivariada para determinar o quanto da variabilidade do transporte de volume de cada massa de água pode ser explicada pelo Bombeamento de Ekman e pelos fluxos de calor e água doce.

Conforme a Equação 6 a seguir:

$$y = \mathbf{Ex} + \varepsilon \quad (6)$$

onde, y é o transporte de volume mensal de cada massa de água, \mathbf{E} é a matriz das variáveis preditoras (W_e , Q , F), e então a dimensão $NT \times 3$, onde NT é a

dimensão da série temporal e x é o vetor de coeficientes de regressão com dimensão 3×1 . Como demonstrado por [Wunsch \[2006\]](#), a solução para x que minimiza os mínimos quadrados, ε , é:

$$x = (\mathbf{E}^T \mathbf{E})^{-1} \mathbf{E}^T y \quad (7)$$

Logo, a variância normalizada do transporte das massas de água que pode ser explicado pelos fluxos W_e , Q e F é:

$$R^2 = 1 - (y - \mathbf{Ex})^T (y - \mathbf{Ex}) (y^T y) \quad (8)$$

Onde um $R^2=1$ significa que 100% da variância dos transportes de volume pode ser explicada pelos fluxos considerados. Também foi calculada a correlação individual direta de cada fluxo com os transportes para verificar se algum dos fluxos poderia explicar melhor a variabilidade observada de forma individual. Além disso, considerando que os transportes das massas de água poderiam responder à variação nos fluxos com algum tempo de atraso, ou seja, não instantaneamente, foram testadas algumas defasagens (*lags*) para as correlações individuais. Então, para cada fluxo, foram testados de 0 – 5 meses de *lag* em relação ao transporte de volume e determinado que o *lag* com a maior correlação seria utilizado nas análises posteriores.

Para encontrar a representatividade da variação latitudinal da superfície dos fluxos que afetam a formação da AAIW e SAMW ao longo do oceano Austral foi realizado o seguinte teste: foi computada a regressão multivariada, utilizando os três fluxos, com diferentes limites sul de latitude. Foram testadas as variações desta regressão considerando as faixas latitudinais de 30°S até 55°S, 65°S e 70°S. Como uma maior amplitude latitudinal não apresentou uma melhoria significativa no R^2 , para fins de otimização computacional, foi decidido utilizar a latitude de 55°S como limite sul para as análises das séries temporais. No

entanto, para a análise das áreas de formação das massas de água foi utilizado o limite latitudinal mais ao sul (70°S).

Como as variáveis preditoras utilizadas neste estudo não são completamente independentes entre si, foi calculado também as correlações parciais, para inferir sobre o grau de independência entre as forçantes analisadas. Para isto, é removido o sinal correlacionado com as outras variáveis antes de calcular o R^2 total. Logo, primeiramente é determinado por uma regressão o componente de y que é ortogonal às outras duas variáveis (i.e. W_e , F , Q), e então determinado a variância explicada R_P^2 do sinal residual, y' , que pode ser explicada pela variável preditora de interesse (i.e. Q). Logo, para se obter a correlação parcial do Bombeamento de Ekman com o transporte de volume das massas de água, por exemplo, primeiramente é removido o sinal da exportação correlacionado com fluxo de calor e água doce, e só então com o transporte residual é calculada a correlação parcial com W_e . Isto foi calculado para cada uma das variáveis de interesse conforme as Equações 9 e 10, onde \mathbf{E}_{ij} é a regressão multivariada utilizando duas variáveis preditoras. Neste contexto, a Equação 8, acima, fornece o R^2 da variável preditora remanescente.

$$y' = y - \mathbf{E}_{ij}x \quad (9)$$

$$R_P^2 = 1 - (y' - \mathbf{E}_k x)^T (y' - \mathbf{E}_k x) (y'^T y')^{-1} \quad (10)$$

Para a determinação de quais variáveis são mais importantes no transporte de volume da AAIW e SAMW, e como estão variando ao longo do tempo e entre os cenários, foram utilizadas as médias das áreas analisadas obtendo um resultado para cada fluxo para cada mês, e então comparado com a série temporal do

transporte médio das massas de água em 30°S. Para a identificação das áreas de formação e exportação das massas de água foi calculado o valor médio de cada fluxo em cada ponto de grid para cada experimento, e então computada a correlação multivariada com os transportes das AAIW/SAMW. Desta forma, foi possível identificar as áreas de maior correlação e, assim, inferir sobre o aspecto regional da formação das massas de água estudadas.

Capítulo V: Transportes médios das

AAIW/SAMW

Para a obtenção do título de Doutor pelo Programa de Pós-Graduação em Oceanologia, é requerido que o discente realize a submissão de pelo menos dois artigos científicos como primeiro autor em periódico com corpo indexado e que estes artigos estejam pelo menos em revisão. Desse modo, os resultados da pesquisa desenvolvida durante o período de doutorado e a discussão dos resultados serão apresentados em capítulos distintos na forma de dois artigos. O primeiro artigo, de autoria de Almeida L., Mazloff M., Mata M.M. é intitulado “***The Impact of Southern Ocean Ekman Pumping, Heat and Freshwater flux Variability on Intermediate and Mode Water Export in CMIP models: Present***

and Future Scenarios” e foi publicado no periódico “***Journal of Geophysical Research: Oceans***” (DOI: 10.1029/2021JC017173).

5.1 Síntese do artigo

Neste artigo foram avaliados os processos dominantes na variabilidade temporal dos transportes de volume médios das AAIW/SAMW em 30°S, utilizando os GCM's CMIP, gerações 5 e 6. Além disso, investigou-se como as mudanças climáticas afetam estes processos nos cenários futuros. A teoria prediz que estas massas de água são subduzidas pelo estresse do vento combinado com a perda de flutuabilidade pelos fluxos de calor e água doce na interface ar-mar. Primeiramente, foi encontrado uma alta variabilidade entre os resultados de transporte das massas de água ao longo dos modelos, onde a maioria deles superestima estes valores. Entretanto, os modelos parecem reproduzir a formação das massas de água de interesse pela combinação correta dos fluxos oceano-atmosfera. Nos cenários atuais, a forçante dominante para a AAIW foi o fluxo de calor, enquanto para a SAMW foi o bombeamento de Ekman causado pelo estresse dos ventos de oeste, estes característicos da região circumpolar Antártica. Porém, uma análise de correlação multivariada demonstrou que as exportações de ambas as massas de água são melhores explicadas combinando os três fatores (bombeamento de Ekman, fluxo de água doce e fluxo de calor). Nos cenários futuros, é demonstrado que estes fluxos passam por mudanças de tendências significativas, o que impacta os transportes das AAIW/SAMW. Ambos transportes seguem significativamente correlacionados com os fluxos considerados, porém são evidenciadas mudanças nos coeficientes de correlação causadas, provavelmente, por mudanças nas forçantes dominantes.

Logo, as correlações são não-estacionárias e, portanto, não podem ser estimadas com estatística básica, ressaltando a importância das estimativas dos modelos climáticos, e da relevância de uma representação mais acurada por parte dos GCM's.

5.2 Artigo 1

The Impact of Southern Ocean Ekman Pumping, Heat and Freshwater flux Variability on Intermediate and Mode Water Export in CMIP models: Present and Future Scenarios

Lucas Almeida¹, Matthew R. Mazloff², Mauricio M. Mata¹

1 Laboratório de Estudos dos Oceanos e Clima - LEOC, Instituto de Oceanografia, Universidade Federal do Rio Grande-FURG, Rio Grande, RS, Brazil

2 Scripps Intituation of Oceanography, University of California San Diego, San Diego, CA, USA

Corresponding author: Lucas Almeida, lucasralm@gmail.com

Key Points:

- AAIW and SAMW export is highly variable and correlated with multiple flux components.
- The volume export variability follows expected theoretical relationships with fluxes.
- Export is projected to increase, and was not skillfully predicted assuming stationary statistics.

5.2.1 Abstract

Subduction in the Antarctic circumpolar region of the Southern Ocean results in the formation of Antarctic Intermediate Water (AAIW) and Subantarctic Mode Water (SAMW). Theoretical understanding predicts that subduction rates of these water masses is driven by wind stress curl and buoyancy fluxes. The objective of this work is to evaluate the extent to which AAIW and SAMW variability are correlated to Southern Ocean air-sea fluxes and how potential changes to those forcings would impact the future water mass export rates. We correlate the water mass volume transport at 30°S with Ekman pumping, freshwater and heat fluxes in the Coupled Model Intercomparison Project (CMIP). The export of these water masses varies across models, with most overestimating the total transport. Correlation coefficients between the air-sea fluxes and exports are consistent with theoretical expectations. In the picontrol/historical scenarios, the highest correlations with AAIW export variability are heat flux, while Ekman pumping best explains SAMW. However, multivariate regressions show that both AAIW and SAMW export variability are better explained using the combination of all three fluxes. In future scenario simulations air-sea fluxes trend significantly in the catastrophic scenario (RCP8.5 and SSP8.5). Both AAIW and SAMW are still highly correlated to the fluxes, but with different correlation coefficients. The dominant forcing components even change from the present simulations to the future scenario runs. Thus correlations between AAIW and SAMW transports and air-sea fluxes are not stationary in time, limiting the predictive skill of statistical models and highlighting the importance of using complex climate models.

5.2.2 Plain Language Summary

The ocean plays a fundamental role in the climate system, storing and transporting heat and carbon. In particular, water mass changes that occur in the Southern Ocean play an important role in setting the properties of the global ocean interior. Here we use climate models to investigate aspects of the system affecting this oceanic transport and storage of interior water masses, focusing on the ocean's intermediate layer. These intermediate waters that are exported from the Southern Ocean to the rest of the global oceans are known as Antarctic Intermediate Water (AAIW) and Subantarctic Mode Water (SAMW). The main goal of this study is to determine what processes are driving their temporal variability and how those water masses would be impacted in the future due to climate change. We find that AAIW and SAMW are highly correlated with wind stress, heat and freshwater exchanges between the ocean and atmosphere. Future scenarios project significant changes for those fluxes, leading to warmer and saltier waters and more intense winds. These cause relevant alterations in the volume transport of both water masses in the future scenarios, especially for the scenario with the most extreme changes, with implications for stability of the climate system.

5.2.3 Introduction

The Meridional Overturning Circulation (MOC) is driven by wind and buoyancy forcing [Marshall et al. 2003]. Intense winds and buoyancy fluxes result in thick mixed layers [De Boyer et al. 2004], providing a route for sequestering heat and carbon dioxide from the atmosphere to the deep ocean [Sabine et al. 2004; Sallée et al. 2012]. According to Roemmich et al. [2015] the Southern Ocean (SO)

accounts for 67%-98% of the observed increase of heat content in the global ocean. Antarctic Intermediate Water (AAIW) and Subantarctic Mode Water (SAMW) masses acquire their physical characteristics in these deep mixed layers, and then are subducted to the north where they ventilate the subtropical gyres [Sallée et al. 2010]. This equatorward advection in the subtropics takes place along the eastern boundaries of all major oceans [Stramma, 1999] being a major component of the upper limb of the MOC, and hence fundamental to maintaining the climate state [Talley 2003; Pahnke et al. 2008].

Several studies have shown that Southern Ocean intermediate waters originate at high latitudes, south of Polar Front [PF; e.g. McCartney et al. 1977], with some arguing that formation occurs between the PF and Subantarctic Front [Rintoul et al. 1999, Hartin et al. 2011]. The processes governing the formation rates of AAIW and SAMW are still not well characterized, but several mechanism have been proposed [Zhu et al. 2018]. The residual mean theory applied by Marshall & Radko [2003] combines patterns of wind forcing, buoyancy forcing, and stratification to infer the MOC, and thus subduction magnitudes to intermediate layers. According to this framework, the volume of AAIW and SAMW exported from the Southern Ocean should be strongly associated with wind stress and air-sea fluxes of freshwater and heat. This work investigates these associations in climate models from the Coupled Modeling Intercomparison Project Phase 5 and 6 (CMIP5 and CMIP6). The model ensemble mean air-sea fluxes at the Southern Ocean are presented in Figure 3, together with a schematic of vertical water mass circulation at the same region. These values suggest a reasonable representation of these processes in the CMIP6 models.

Previous works have shown that CMIP5 models reproduce the maximum wind stress forcing at the circumpolar region, which is an improvement from generation 3 [Beadling et al. 2019]. Other studies have quantified the volume transport of water masses exported from the Southern Ocean in previous CMIP simulations (generation 3 and 5). For example, it was shown that there are large biases in the export of AAIW in CMIP5 models [Sallée et al. 2013; Zhu et al. 2018]. Moreover, Sallée et al. [2013] studied the mean water mass transport across 30°S in a multi-model ensemble and related it to mean outcrop window, heat and freshwater fluxes. Here, we consider the transport at that same section, but build on the analysis by including the new generation of CMIP models and, importantly, we assess the transport time variability in each model. We relate this variability to the wind stress curl, freshwater flux, and heat flux in each respective model. Specifically, we are interested in which forcing mechanisms are most correlated with the AAIW and SAMW transports, if the corresponding correlation coefficients are physically plausible, and whether the relationships are robust across CMIP generations.

Finally, Climate and Earth System Models (ESMs) are important tools for making quantitative climate projections to the end of 21st century, enabling assessment of the impact of different scenarios of anthropogenic activity on climate [Bracegirdle et al. 2020]. In this sense, we also used CMIP5/CMIP6 models to estimate the potential future changes in fluxes, AAIW and SAMW export, and their relationships to the end of 21st century and under different scenarios of climate change.

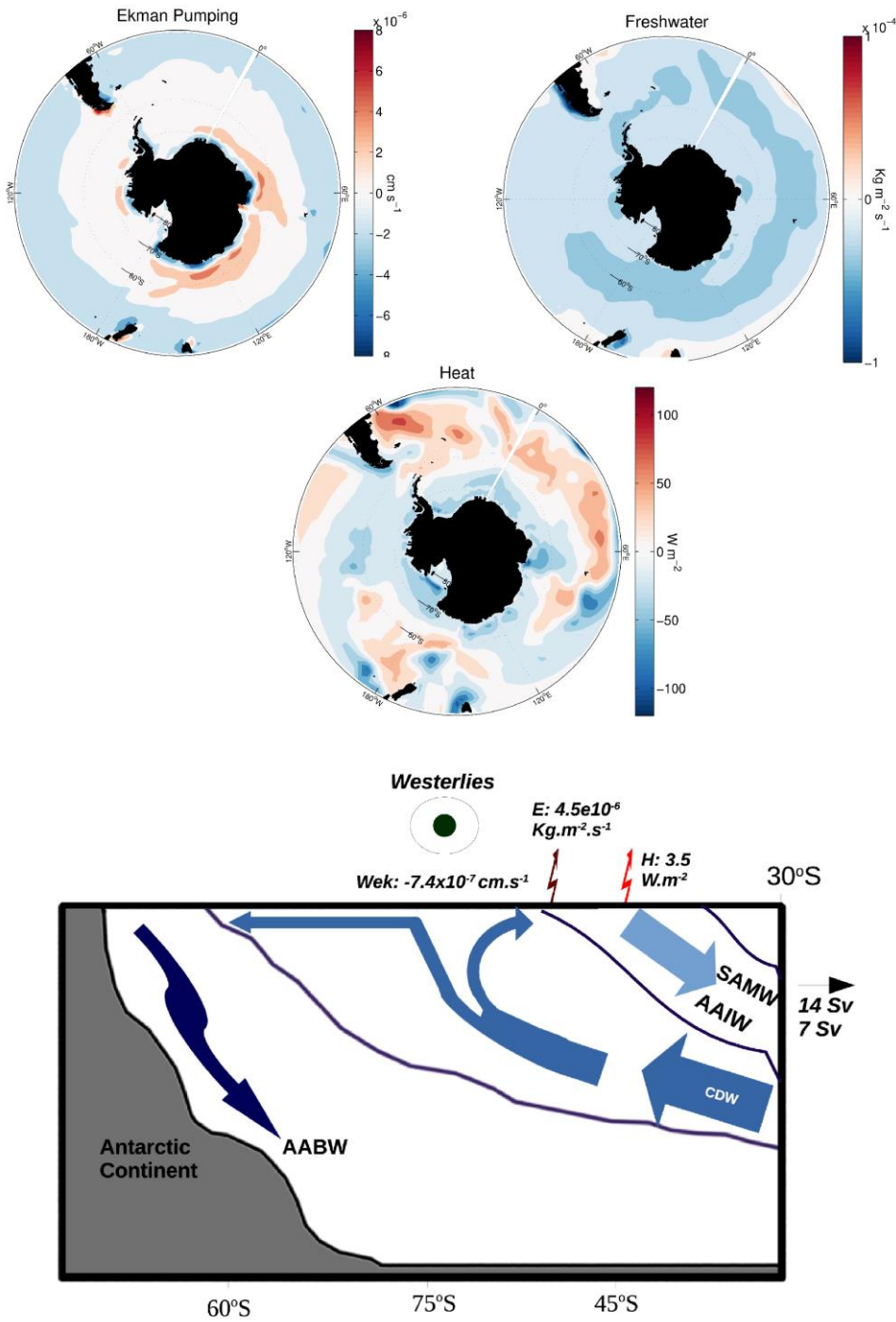


Figure 5.1. The upper three panels are the CMIP6 ensemble mean fluxes in the Southern Ocean calculated using the last 30 years of historical experiment. The top two are Ekman pumping and freshwater flux, and the mid panel is the heat flux. The lower panel is a schematic showing the mean fluxes, where W_{ek} is the mean Ekman transport of $-7.4 \times 10^{-7} \text{ cm s}^{-1}$, E is evaporation of $4.5 \times 10^{-6} \text{ Kg m}^{-2} \text{s}^{-1}$, and H is the mean heat flux of 3.5 W m^{-2} . This lower panel gives a vertical perspective of Antarctic water masses and circulation, with an inflow of Circumpolar Deep Water

(CDW) into the Southern Ocean and an export of Antarctic Bottom Water (AABW), AAIW and SAMW. The CMIP6 models mean export of SAMW is 14 Sv and of AAIW is 7 Sv.

5.2.4 Materials and Methods

5.2.4.1 Models

Outputs from 27 CMIP models from version 5 [Taylor et al. 2012] and 6 [Eyring et al. 2016] were used in this study. Atmospheric and oceanic component variables were downloaded from the Deutsches Klimarechenzentrum Data Center portal (<https://esgf-data.dkrz.de>). The list of models and respective resolutions is presented in Table 2. To analyse the models performance and the natural time variability, we used monthly averages of the ocean state from the “historical” runs, which is a scenario forced by natural and anthropogenic factors during the 20th century. To provide a basis of comparison, we also evaluated the pre-industrial revolution experiment denoted “picontrol” [Taylor et al. 2012]. Finally, we used CMIP models future scenarios runs to estimate the behavior of AAIW and SAMW transports up to the end of the 21st century. These future runs are generated using prescribed radiative forcing values from the Representative Concentration Pathways (RCPs) for generation 5 models [Meinshausen et al. 2011]. In this case, we used the scenarios 4.5 W m^{-2} (RCP4.5) and 8.5 W m^{-2} (RCP8.5) which are the medium range and the most catastrophic ones, respectively. For CMIP6 models, the equivalent scenarios used in this study are called Shared Socioeconomic Pathways (SSP4.5 and SSP8.5; Eyring et al. 2016). We adopt the nomenclature Scenario 4.5 (S4.5) and Scenario 8.5 (S8.5) when referring to the future scenarios from both generations.

Table 5.1. Climate Coupled Models used in this study. Some details for each model are presented: name, generation, ocean and atmospheric horizontal resolution, ocean vertical coordinate and number of levels (Z are traditional depth coordinates, Z* are re-scaled depth coordinates, S are sigma coordinates, and SZ are hybrids) and main reference.

Model	Generation	Ocean (Lat x	Atmospheric	Vertical	Reference
		Lon)	(Lat x Lon)	(levels)	
ACCESS1-0	CMIP5	1.88° x 1.24°	1.88° x 1.24°	Z(50)	Collier & Uhe (2012)
ACCESS1-3	CMIP5	1.88° x 1.24°	1.92° x 1.45°	Z(50)	Collier & Uhe (2012)
ACCESS-CM2	CMIP6	1.00° x 1.00°	1.88° x 1.25°	Z*(50)	Dix et al. (2019)
ACCESS-ESM1-5	CMIP6	1.00° x 1.00°	1.88° x 1.25°	Z*(50)	Ziehn et al. (2019)
BCC-CSM2-MR	CMIP6	1.00° x 1.00°	1.13° x 1.10°	Z(40)	Wu et al., (2018)
BCC-ESM1	CMIP6	1.00° x 1.00°	2.81° x 2.81°	Z(40)	Zhang et al. (2018)
CAMS-CSM1-0	CMIP6	1.00° x 1.00°	1.00° x 1.00°	Z(50)	Rong (2019)
CanESM2	CMIP5	2.81° x 2.81°	2.81° x 2.81°	Z(40)	CCCM & CCCm (2015)
CanESM5	CMIP6	1.00° x 1.00°	2.81° x 2.81°	Z(45)	Swart et al. (2019)
CNRM-CM5	CMIP5	1.41° x 1.41°	1.41° x 1.41°	Z(42)	Volodire et al. (2013)
CNRM-CM6-1	CMIP6	1.00° x 1.00°	1.40° x 1.40°	Z*(75)	Volodire (2018)
CNRM-ESM2-1	CMIP6	1.00° x 1.00°	1.40° x 1.40°	Z*(75)	Seferian (2018)
CSIRO-Mk3-6-0	CMIP5	1.88° x 1.88°	1.88° x 1.88°	Z(31)	Jeffrey et al., (2013)
EC-Earth3-Veg	CMIP6	1.00° x 1.00°	0.70° x 0.70°	Z*(75)	EC-Earth (2019)
GFDL-ESM2G	CMIP5	2.50° x 2.00°	2.50° x 2.00°	S(63)	Dunne et al. (2014)
GFDL-ESM2M	CMIP5	2.50° x 2.00°	2.50° x 2.00°	Z(50)	GFDL (2018)

GISS-E2-1-H	CMIP6	$1.00^\circ \times 1.00^\circ$	$2.50^\circ \times 2.00^\circ$	SZ(32)	NASA/GISS (2018)
Had-GEM2-ES	CMIP5	$1.88^\circ \times 1.25^\circ$	$1.88^\circ \times 1.25^\circ$	Z(40)	METO & R2de Clima (2013)
INM-CM4-8	CMIP6	$1.00^\circ \times 0.56^\circ$	$2.00^\circ \times 1.50^\circ$	S(48)	Volodin et al. (2019)
INM-CM4	CMIP5	$2.00^\circ \times 1.50^\circ$	$2.00^\circ \times 1.50^\circ$	S(40)	Volodin et al. (2010)
MIROC5	CMIP5	$1.41^\circ \times 1.41^\circ$	$1.41^\circ \times 1.41^\circ$	SZ(50)	AORI et al. (2013)
MIROC6	CMIP6	$1.00^\circ \times 0.70^\circ$	$0.70^\circ \times 0.70^\circ$	SZ(62)	Tatebe & Watanabe (2018)
MIROC-ESM	CMIP5	$2.81^\circ \times 2.81^\circ$	$2.81^\circ \times 2.81^\circ$	SZ(44)	Watanabe et al. (2011)
MPI-ESM1-2-HR	CMIP6	$0.44^\circ \times 0.44^\circ$	$0.94^\circ \times 0.94^\circ$	Z(40)	Schupfner et al. (2019)
MPI-ESM-LR	CMIP5	$1.88^\circ \times 1.88^\circ$	$1.88^\circ \times 1.88^\circ$	Z(40)	Giorgetta et al. (2012)
MRI-CGCM3	CMIP5	$1.13^\circ \times 1.13^\circ$	$1.13^\circ \times 1.13^\circ$	Z(50)	Yukimoto et al. (2012)
SAM0-UNICON	CMIP6	$1.13^\circ \times 0.47^\circ$	$1.25^\circ \times 0.94^\circ$	Z(50)	Park & Shin (2019)

5.2.4.2 Definition of Water Masses

The AAIW and SAMW water masses exported from the Southern Ocean in each CMIP model may be of different density classes than observed in the real ocean. Thus, to identify these water masses, we applied the methodology presented in [Sallée et al. \[2013\]](#) to find the most appropriate potential densities delimiting them in each CMIP model. The methodology defines the water masses by hydrographic properties: AAIW is associated with a minimum salinity in the circumpolar belt region [[Tomczak et al. 2007](#)], while the SAMW is related to a minimum in stratification, and hence minimum Potential Vorticity (PV).

The process first identifies a minimum salinity location (S_{min}) with local salinity maxima directly above ($S_{max(above)}$) and below ($S_{max(below)}$). The limits of AAIW are, in terms of density space, a quarter of the distance between S_{min} and S_{above} (S_{below}) for the upper (lower) end, as shown in the following equations:

$$\sigma_2(acima) = (3\sigma_2(S_{min}) + \sigma_2(S_{max(acima)})) / 4 \quad (1)$$

$$\sigma_2(abaixo) = (3\sigma_2(S_{min}) + \sigma_2(S_{max(abaixo)})) / 4 \quad (2)$$

This was carried out for each model at 30°S, where the total thickness, H , and transport of AAIW, VH , was calculated.

To identify the SAMW, we analyzed the PV at 30°S. First, the upper limit of AAIW is identified as being the lower limit of SAMW. Then, we search for a minimum PV level associated with a density vertical gradient smaller than 0.1 kg m⁻³. The SAMW layer is determined as having an upper density limit that contains at least 90% of the total minimum local PV.

After determining the upper and lower potential density limits, it is straightforward to calculate the thickness, H , and export, VH of SAMW for each climate model.

To obtain the total volume of each water mass crossing 30°S, we vertically integrate the monthly mean meridional velocity over each water mass layer. Thus, we determine the total intermediate and modal water volume transport at 30°S as a monthly time-series. This time series is then used to investigate the formation process in CMIP models.

5.2.4.3 Ekman Pumping

All the coupled climate models used here provide the monthly mean zonal and meridional components of surface wind stress. From these outputs we calculate the vertical Ekman pumping (W_e) in the region following Equation 2:

$$W_e = \nabla_x \left(\frac{\tau}{\rho_0 f} \right) \quad (3)$$

Where τ is the wind stress component, ρ_0 is the reference seawater density and f is the Coriolis parameter. A monthly average Ekman pumping time series is made by integrating W_e between latitudes 30°S and 55°S.

5.2.4.4 Heat and Freshwater Fluxes

The total ocean and atmosphere heat exchange is averaged monthly and integrated between latitudes 30°S and 55°S. The total heat flux, Q , is given by:

$$Q = -hfss - hfls + rlds + rlus + rsds + rsus \quad (4)$$

Where $hfss$ and $hfls$ are the sensible and latent heat fluxes, $rlds$ and $rlus$ are the downwelling and upwelling net longwave radiation, $rsds$ and $rsus$ are the downwelling and upwelling net shortwave radiation. All these parameters are outputs from the CMIP models. This follows the convention of positive Q being heat fluxed into the ocean (i.e. warming ocean temperatures), thus making the ocean more buoyant.

The freshwater fluxes are calculated by the difference between precipitation and evaporation, $F = P - E$, integrated over the same area (i.e. 30°S to 55°S). Thus, F follows the convention that positive values decrease ocean salinity content,

thus making the ocean more buoyant. [Griffies et al. \[2016\]](#) states that salinity restoring is necessary as global climate models typically drift over decadal timescales. Here, all models used salinity surface restoring with different implementations [[Danabasoglu et al. 2014](#); [Rahaman et al. 2020](#)], which potentially influence the estimates of freshwater fluxes. However, we do not expect a strong impact on our results as the typical restoring timescales are far longer than the monthly variability considered in the present study.

5.2.4.4 Multivariate Regression Procedure, Including Lags

To enable direct comparison of all variables of interest (VH , W_e , F , Q), we remove the mean from the time series, and then normalize by dividing the time series by its standard deviation. We then carry out a multi-variate regression to inform how much the variation of water masses transport, $y = VH$, can be explained by the Ekman Pumping and fluxes of freshwater and heat:

$$y = \mathbf{E}x + \varepsilon \quad (5)$$

Here \mathbf{E} is the matrix of predictor variables (W_e , F , Q), and thus size $NT \times 3$, where NT is the length of the time series, and x is a 3×1 vector of regression coefficients. As shown in [Wunsch \[2006\]](#), the solution for x that minimizes the squared residuals, ε , is

$$x = (\mathbf{E}^T \mathbf{E})^{-1} \mathbf{E}^T y \quad (6)$$

The normalized variance of VH that can be explained by (W_e , F , Q) is:

$$R^2 = 1 - (y - \mathbf{E}x)^T (y - \mathbf{E}x) (y^T y)^{-1} \quad (7)$$

with $R^2 = 1$ implying 100% of the variance can be explained.

We also carry out this analysis for each independent predictor variable alone to evaluate if one variable can do a similar job explaining the variance as to what is

accomplished using all three. We also test which time lags best explain the water mass transports for each individual component. Calculations were carried out using 0 to 5 month lags for each component, and the lags with the largest R^2 were used in the combined analysis.

To test the representativeness of the latitudinal range used here for surface forcing that affects the AAIW and SAMW transports, we computed the multivariate regression using all three fluxes (Ekman Pumping, Freshwater and Heat) using different southern limits. We tested the latitudinal ranges 30°S to 65°S and 30°S to 70°S, and found very similar results to the 30°S to 55°S range used in the present study. Moreover, no substantial improvements in the R^2 were found in both tested cases. Based on the slightly higher R^2 values and due to computational efficiency, we opted to use the 30°S to 55°S latitudinal range throughout this study

The fluxes analyzed are not completely independent between themselves. To address this problem, we calculate partial correlations in an attempt to infer the level of independence between the forcing components. To achieve this goal, we first remove the signal correlated with other variables before determining R^2 . Thus, we first determine the component of y that is orthogonal to the two other predictor variables (e.g. We , F) via regression, and then determine the variance explained, R^2 , of this residual signal, y' , that can be explained by the remaining predictor (e.g. Q). For example, to assess the partial correlation of the Ekman pumping with the water mass exports, we first remove the signal of export correlated to freshwater and heat fluxes, and then determine an R^2 for the residual export signal with Ekman pumping. The same was done for each flux component.

$$y' = y - \mathbf{E}_{ij}x \quad (8)$$

$$R_P^2 = 1 - (y' - \mathbf{E}_k x)^T (y' - \mathbf{E}_k x) (y'^T y')^{-1} \quad (9)$$

where the $\mathbf{E}_{ij}x$ is the multivariate regression using 2 predictor variables, i and j , and Equation 10 gives the R^2 value for the partial correlation of the third variable, k .

5.2.5 Results

5.2.5.1 Mean State

The mean volume transport of Intermediate and Mode waters at 30°S varies widely across models (Figure 5.2), with AAIW mean transports ranging from 2 to 18 Sv and SAMW mean transports ranging from 3 to 30 Sv. [Sallée et al. \[2013\]](#) show that, compared to observations, these recently ventilated water mass layers have the largest biases of all the Southern Ocean layers in the CMIP models generation 5. In addition, [Zhu et al. \[2018\]](#) also identified significant biases in the properties of AAIW for CMIP5 models. Some models show very low mean transport values for AAIW (CSIRO-Mk3-6-0, INM-CM4, MIROC5), while MIROC6 has the highest values. SAMW transports have a lower spread around the multi-model mean value of about 11 Sv. The INM-CM4 and MPI-ESM1-2-HR models have low SAMW transports, and INM-CM4-8 and MIROC5 have notably high transports. In the present work, we find a mean transport of 6.15 ~Sv for AAIW and 11.29 ~Sv for SAMW, values close to the 5.85 ~Sv and 11.55 ~Sv presented in [Sallée et al. \[2013\]](#). Several factors explain the differences between both studies. First, we use a somewhat different group of models. [Sallée et al. \[2013\]](#) did not analyze CMIP6 models and also we used some CMIP5 models not considered in their analyses (e.g the ACCESS models, CanESM2, INM-CM4,

MRI-CGCM3). Moreover, they also used some other models not considered here (GISS-E2-R, HadCM3, HadGEM2-CC, MIROC-ESM-CHEM). Also, we are interested in the time variability, so we used the entire available simulation period for each experiment and for each model, while [Sallée et al. \[2013\]](#) analyzed the mean of the last 30 years of each experiment.

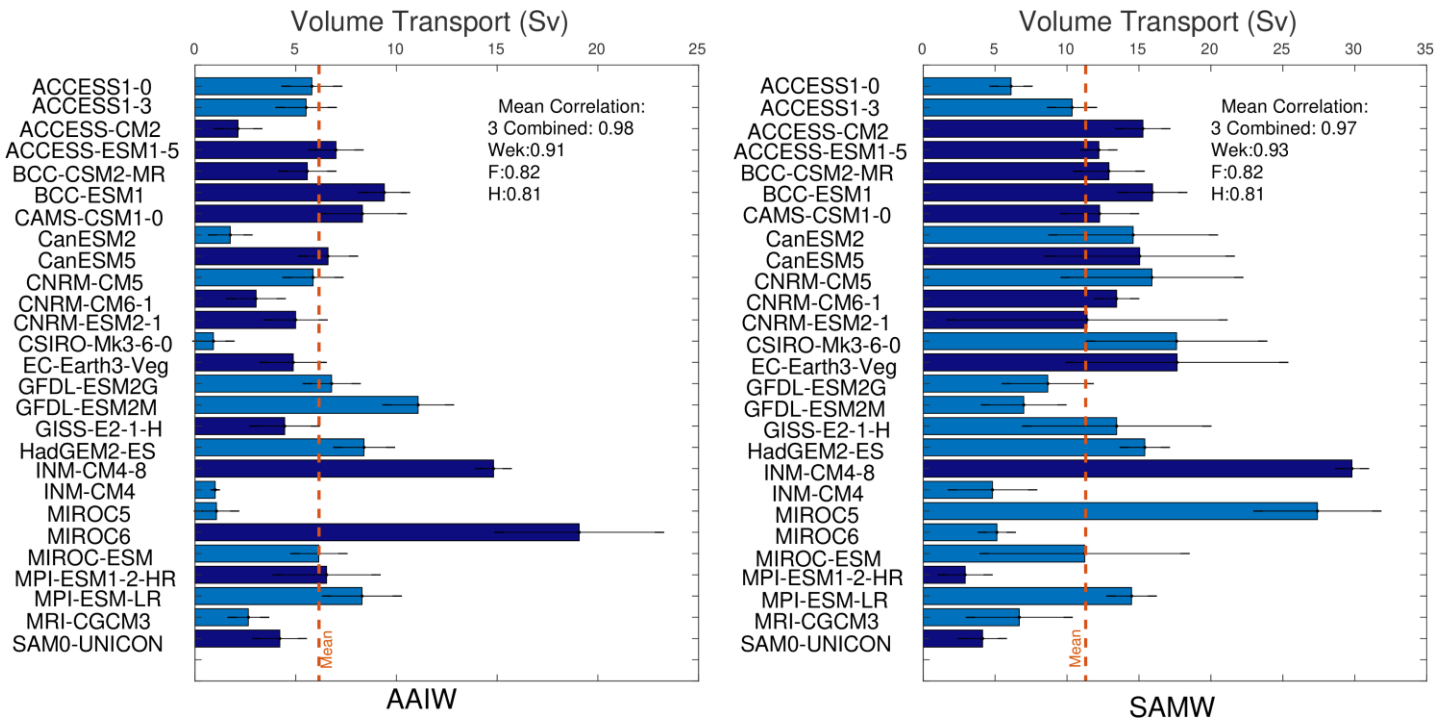


Figura 5.2. Mean water mass volume transports at 30°S for each model (units are Sv). Dark blue and light blue bars show the CMIP6 and CMIP5 models, respectively. The orange dashed line is the multimodel mean transport. The left panel shows AAIW transport and the right panel shows SAMW. The whiskers are the transports standard deviation. Mean correlations (R^2) between mean fluxes and mean transports across models are noted in the plot. Also included is the R^2 for the multivariate regression.

The volume transport of AAIW and SAMW water masses in CMIP6, with a mean of 7 Sv for AAIW and 10 Sv for SAMW, are more consistent with inferences from data than the results from CMIP5. The combined model mean (CMIP6) is higher than the observationally estimated combined mean of 10 Sv reported by [Talley \[2003\]](#) and [Talley et al. \[2003\]](#), but is closer to the estimated 14 Sv of the MOC

upper limb transport reported by [Ferster et al. \[2018\]](#). This may be due to a better representation of atmospheric circulation in the new generation models. [Beadling et al. \[2020\]](#) state that all metrics pertaining to the surface wind stress forcing have improved and [Bracegirdle et al. \[2020\]](#) showed improvements in the representation of westerly jets. To understand the variability in the mean AAIW and SAMW transports, we calculate the correlation across models between these mean transports and the mean fluxes (Figure 5.2). The results imply a covariance between mean water mass export and mean air-sea fluxes in the climate models, with the strongest correlation being to Ekman pumping (AAIW: $R^2=0.91$; SAMW $R^2=0.93$). This result is similar to the correlation found by [Sallée et al. \[2013\]](#) comparing the multimodel mean of mode water transport and the outcrop area (correlation coefficient of 0.84). In addition, this analysis showed that multivariate correlation to the fluxes resulted in a higher R^2 and suggested that these fluxes are able to explain almost all the variance in the mean water mass transports (AAIW $R^2=0.98$; SAMW: $R^2=0.97$).

The mean picontrol/historical fluxes for each model are presented in Figure 5.3. For ease in comparison they are all normalized using the maximum value of each flux. The Ekman pumping in most cases presented consistent values between model results, BCC-CSM2-MR has a higher value while MIROC5 and MIROC6 have the lowest. For the freshwater flux there are two models that seems to be overestimating this value, CAMS-CSM1-0 and EC-Earth-Veg, while other models present similar values. The heat fluxes vary between models, with MIROC6 presenting higher values, which may reflect the higher AAIW export in that model. Another interesting point about the mean water mass exports is that the models with higher vertical resolution (presented in Table 5.1) have more realistic

transports. The number of vertical levels is proportional to the vertical grid spacing of the uppermost ocean cell, with most models having 40 to 50 vertical levels and an approximately 10-m thick upper layer. The models with higher vertical resolution have upper layer thicknesses of reaching down to 1-m. The models with lowest vertical resolution, independent of coordinate type, presented the largest differences from the multimodel means (6.15~Sv for AAIW and 11.29~Sv for SAMW). The CSIRO-Mk3-6-0 has the lowest resolution among the models analyzed in this study (31 vertical levels, upper layer thickness of 10-m) and underestimates the AAIW transport by about 4~Sv and overestimates SAMW by about 5 Sv compared to the multimodel mean values. Another example is the INM-CM4-8 (sigma coordinate with 40 levels) which overestimates both water masses, reaching values of~15 Sv for AAIW and 30~Sv for SAMW. Meanwhile INM-CM4, with the same characteristics, underestimates the transports by about 4~Sv and 6~Sv for AAIW and SAMW respectively, when compared with the multi-model mean value. The high vertical resolution simulations (e.g. CNRM-CM6-1, CNRM-ESM2-1, and EC-Earth3-Veg models, all with 75 vertical levels) had transports closer to the multi-model mean than the coarse models, though there are some exceptions and a robust correlation was unattainable. An example exception is MIROC6, which has a higher resolution (62 levels with hybrid coordinates) but overestimates AAIW transport with an export of about 19 Sv, and underestimates SAMW with an export of only 5 Sv. Meanwhile BCC-CSM2-MR, which has a low vertical resolution (40 levels), performs well with respect to reproducing the multi-model mean transport values. Nevertheless, in general, the higher vertical resolution models considered in this study simulate AAIW/SAMW volume transports closer to observed values.

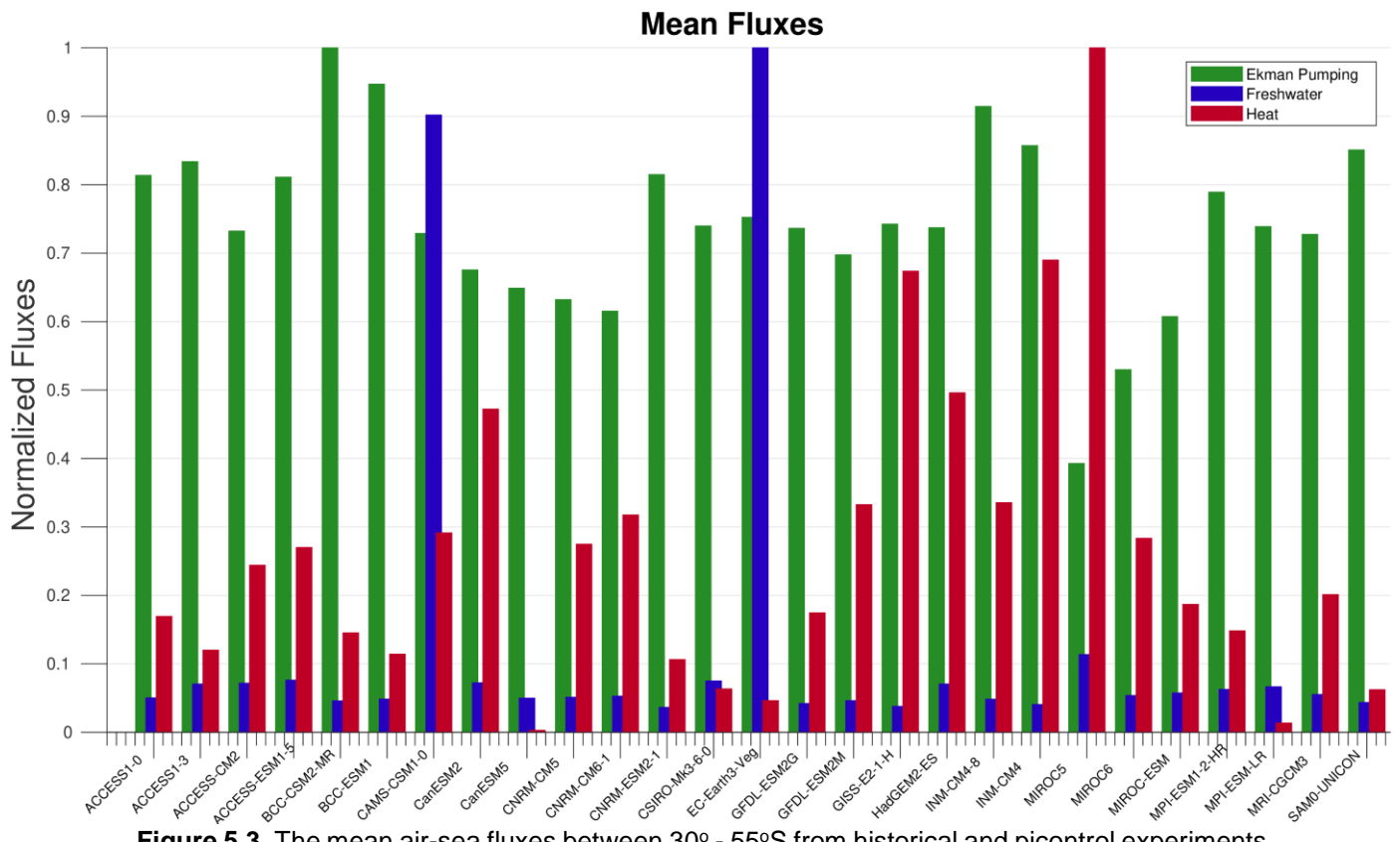


Figure 5.3. The mean air-sea fluxes between 30° - 55° S from historical and picontrol experiments for each model, normalized by the maximum value (-8.6×10^{-7} cm s $^{-1}$ for Ekman pumping from model BCC-CSM2-MR; -7.6×10^{-6} kg m $^{-2}$ s $^{-1}$ for freshwater from the model EC-Earth3-Veg and 6.19 W m $^{-2}$ for heat flux from MIROC6). The bars are the Ekman pumping (green), freshwater (blue) and heat (red) fluxes.

5.2.5.2 Time Variability

We showed that model mean transports are strongly correlated to mean fluxes.

Here we test whether the variability of the transport within each model correlates with the air-sea flux variability. As a first assessment, we consider lag correlations of transport to individual flux components in seven of the models (Figure 5.4). We tested 0 to 5 month lags, and did not test longer lags as the correlations diminish by month 5. For Ekman pumping the correlation was strongest without using any lag, implying that water mass transport co-varies strongest with wind stress on timescales less than a month. Most models had maximum R 2 using 2 month lags when considering freshwater fluxes, the only exception is SAM0-UNICON where

3 and 4 months lags showed a greater R^2 . For heat flux there is more variation, and we do not find a relevant difference between 2 or 3 month lags. The results presented below were carried out with both 2 and 3 months lags for heat flux and gave the same qualitative results, though the correlations were slightly greater for 3 months. Based on these results, in the following analysis we present correlations using no lag for Ekman pumping, a 2 months lag for freshwater fluxes, and a 3 months lag for heat fluxes.

The fluxes presented a higher correlation with AAIW transport in most climate models (Figure 5.5, upper panel). For multivariate regression to AAIW, many models have a R^2 higher than 0.6 (ACCESS1-3, BCC-CSM2-MR, BCC-ESM1, CAMS-CSM1-0, CNRM-CM5, CNRM-CM6-1, CNRM-ESM2-1, EC-Earth3-Veg, GFDL-ESM2M, HadGEM2-ES, INM-CM4-8, INM-CM4, MIROC5, MIROC6), and BCC-ESM1 and CAMS-CSM1-0 were higher than 0.8. However, the fluxes did not correlate with transport in GISS-E2-1-H, MRI-CGCM3 and SAM0-UNICON. Regarding single variables, heat fluxes are best able to account for AAIW variability, with freshwater fluxes also correlating strongly in some models. Meanwhile, Ekman pumping does not correlate with AAIW transport variability.

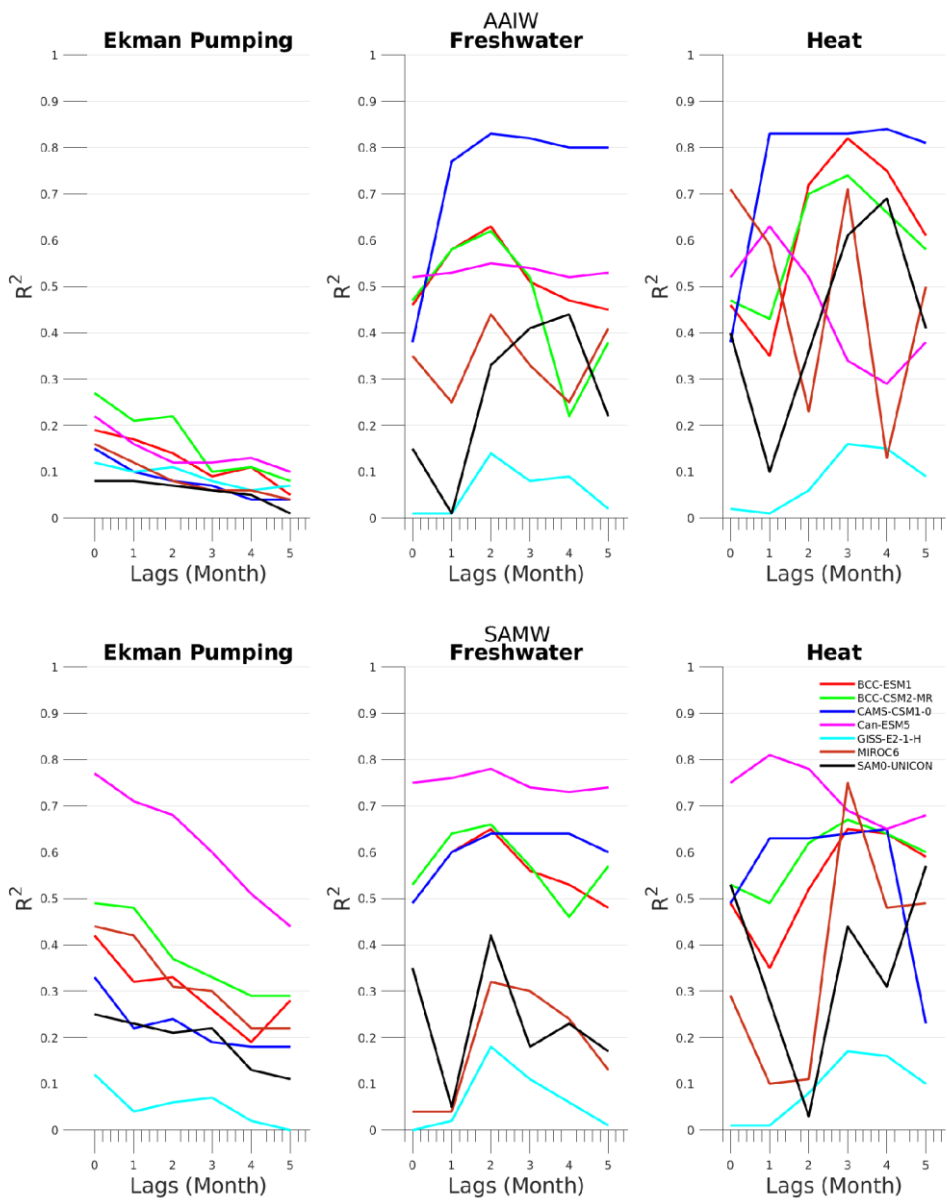


Figure 5.4. Lag correlations for Ekman pumping, freshwater and heat fluxes for each water mass, with AAIW (SAMW) displayed in the top (bottom) panels. Red lines are the model BCC-ESM1, green BCC-CSM2-MR, blue CAMS-CSM1-0, pink Can-ESM5, cyan GISS-E2-1-H, brown MIROC6 and in black SAM0-UNICON.

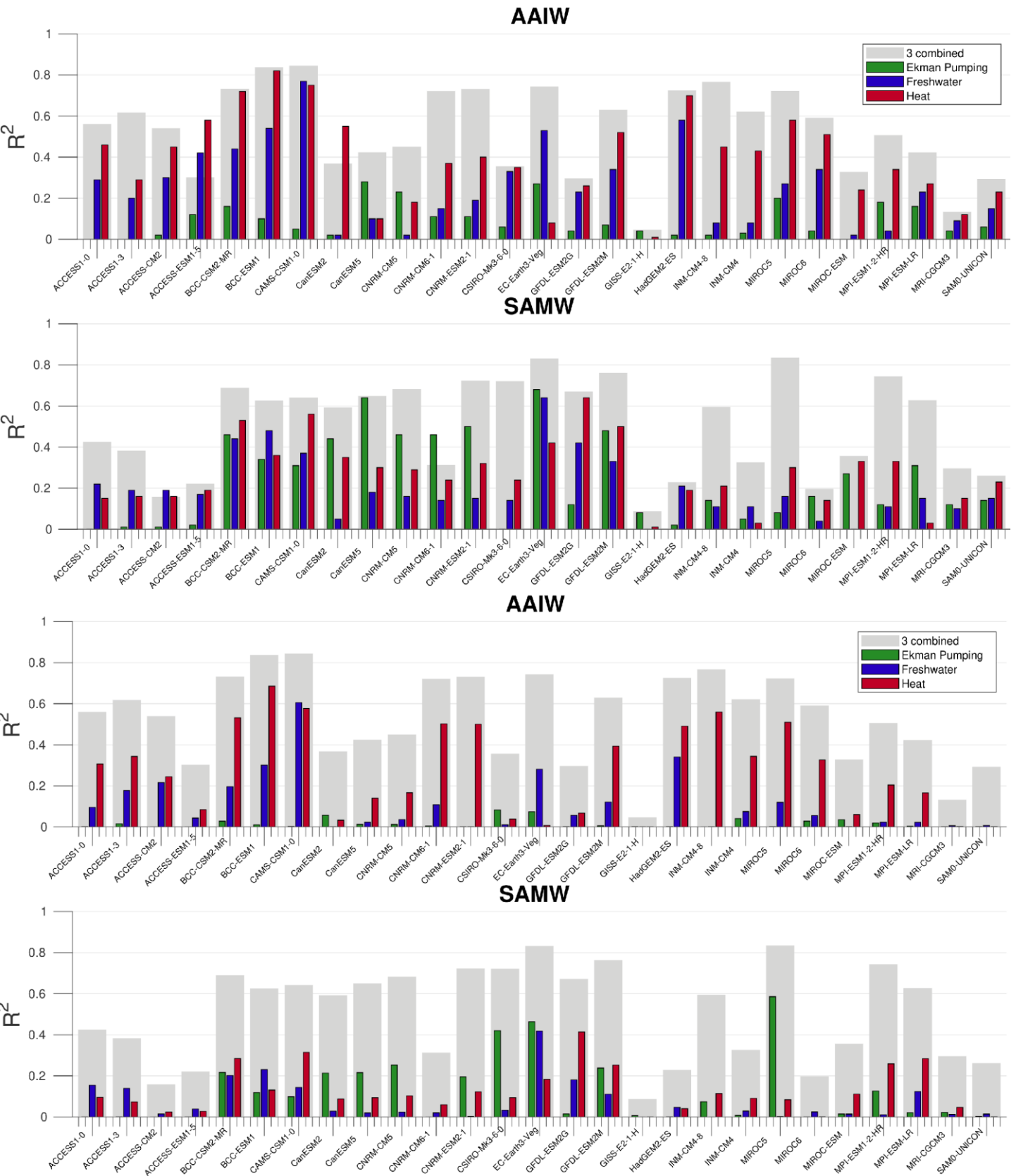


Figure 5.5. The upper two panels show the R^2 for each flux component to the respective water mass transports (AAIW on top and SAMW below). The multivariate correlation is in gray bars,

and individual components are shown in green (Ekman pumping), blue (freshwater), and red (heat) bars. The bottom two panels show the same R^2 for the multivariate correlation in gray, and the R^2 for the partial correlations are given for each individual flux component in color.

The multivariate correlation of forcing to SAMW transport shows similarly high R^2 values, with a large number of the climate models having values greater than 0.6 (BCC-CSM2-MR, BCC-ESM1, CAMS-CSM1-0, CaneSM2, CanESM5, CNRM-CM5, CNRM-ESM2-1, CSIRO-Mk3-6-0, EC-Earth3-Veg, GFDL-ESM2G, GFDL-ESM2M, INM-CM4-8, MIROC5, MPI-ESM1-2-HR, MPI-ESM-LR), and EC-Earth3-Veg and MIROC5 having values greater than 0.8. Low R^2 values are found for ACCESS-CM2, GISS-E2-1-H and SAM0-UNICON. It is better to consider multiple flux components when considering SAMW transport correlations, as no single flux component dominated the correlation across models. Unlike with AAIW, Ekman pumping is highly correlated to SAMW transport in many models, but more variability can be explained by also considering the other flux terms.

To address the issue of the air-sea forcing fluxes covering between themselves (i.e. not being independent), partial correlations between the water mass transports and each flux were computed. The results yield the relative importance of the orthogonal components of the air-sea fluxes to the intermediate water mass export (Figure 5.6, bottom two panels). The partial correlation is assessed by first removing the export signal correlated to the other flux components, and then correlating the specific flux with the water mass export. The results for partial correlation to AAIW transport are consistent with those previously presented, showing heat flux to be the most important component. There are some exceptions: EC-Earth3-Veg in which the freshwater fluxes have a higher partial correlation R^2 ; and CAMS-CSM1-0 that freshwater and heat fluxes have the

same importance. Ekman Pumping adds no value in explaining AAIW transport variance in most models, but for CanESM5 it does have the same partial correlation as heat flux and in CSIRO-Mk3-6-0 it has the highest partial correlation among all fluxes.

Ekman pumping is more important for explaining the high R^2 with SAMW transport in most models, particularly for MIROC5, which has a high R^2 and the partial correlation is dominated by this term. The partial correlation is highest for heat flux in a few models, including MPI-ESM1-2-HR and INM-CM4-8. However, there are many models where forcing components are strongly correlated to each other, leading to low partial correlations for all terms. A clear example is CAMS-CSM1-0, where each individual flux yield partial correlations with R^2 of 0.2 or less, whereas the total multivariate R^2 is close to 0.6. Freshwater flux presents a lower partial correlation in most of the models, but in some models this component is of secondary importance. One example is in EC-Earth3-Veg, where the heat flux does not have a higher partial correlation yet Ekman pumping alone cannot explain the multivariate correlation R^2 of 0.8.

To inform the mechanisms by which these flux components impact AAIW and SAMW transport, the coefficients from the multivariate regression are presented (Figure 5.6). Since all time-series have been normalized, here a regression coefficient of 1 implies that a 1 standard deviation anomaly in surface flux would be associated with a 1 standard deviation anomaly of water mass export. While the R^2 value estimates the skill in predicting the response, the correlation coefficients give the amplitude of the response. Since almost all calculated coefficients are less than 1, this means that the export response to flux anomalies is damped.

The analyses also demonstrates an important agreement of the coefficient sign with theoretical expectations [Marshal & Radko \[2003\]](#), where the export of water masses in intermediate layers increases with increasing Ekman pumping (i.e. increasing Ekman pumping implies a stronger upper limb overturning circulation). Meanwhile, stronger buoyancy input restricts subduction processes necessary to form intermediate water masses, thus reducing export. In consistency, we find positive regression coefficients for Ekman pumping and negative regression coefficients for heat or freshwater input with respect to the variability of mode and intermediate water export.

The regression coefficients for AAIW transport reinforce our finding regarding the sensitivity to heat flux, as it is larger in magnitude than the other components. Similarly, it is clear that Ekman pumping is of minimal importance for explaining the variability. In a few models freshwater flux regression coefficients are of equal magnitude to heat flux: BCC-ESM1, CSIRO-Mk3-6-0, GFDL-ESM2G. The most notable exception is EC-Earth3-Veg, where freshwater flux has a larger coefficient and heat flux has a coefficient with an opposite sign than expected. These regression coefficient exceptions are important given that all these models have higher R^2 correlation for this water mass. SAMW regression coefficient magnitudes are also in consistency with expectations from the previous results: Ekman pumping has slightly higher impact than the other fluxes, but nevertheless, the other flux components are still relevant.

It is also interesting how these coefficients relate to the mean fluxes (Figure 5.4), and mean transports (Figure 5.2). For example, BCC-CSM2-MR presented a SAMW transport very close to the inter-model mean value, but with a very high Ekman pumping, however the partial correlation showed that for this model heat

fluxes are important too, with a low heat value that could compensate the higher Ekman pumping. The EC-Earth3-Veg seems to be overestimating the freshwater fluxes, and that probably reflects in the high importance in the partial correlation of these flux for both water masses. INM-CM4 presented a high Ekman pumping, but not a higher SAMW export, which may be explained by a low multivariate R^2 , and with a very low partial correlation with this specific flux. Also, MIROC5 showed a very low AAIW export, in agreement with a high partial correlation to heat flux and a low value of heat flux. The same model has a significant partial coefficient for Ekman pumping and SAMW transport, implying the high Ekman pumping helps explain the very high mean SAMW transport.

We attempted to understand relationships between model properties leading to higher correlations, and hence compared the R^2 values with several mean properties including volume transports, flux components, correlation coefficients, and the vertical resolution (not shown). The AAIW multivariate R^2 has a reasonable correlation with the number of vertical levels ($R^2=0.28$) and with the mean buoyancy fluxes ($R^2=0.35$ for freshwater and $R^2=0.27$ for heat). The highest correlation in the SAMW case was the freshwater flux ($R^2=0.30$). Nevertheless, we did not consider any of these correlations to be a robust result; we were unable to find consistent indicators across models for the sensitivity of water mass transport to flux variability.

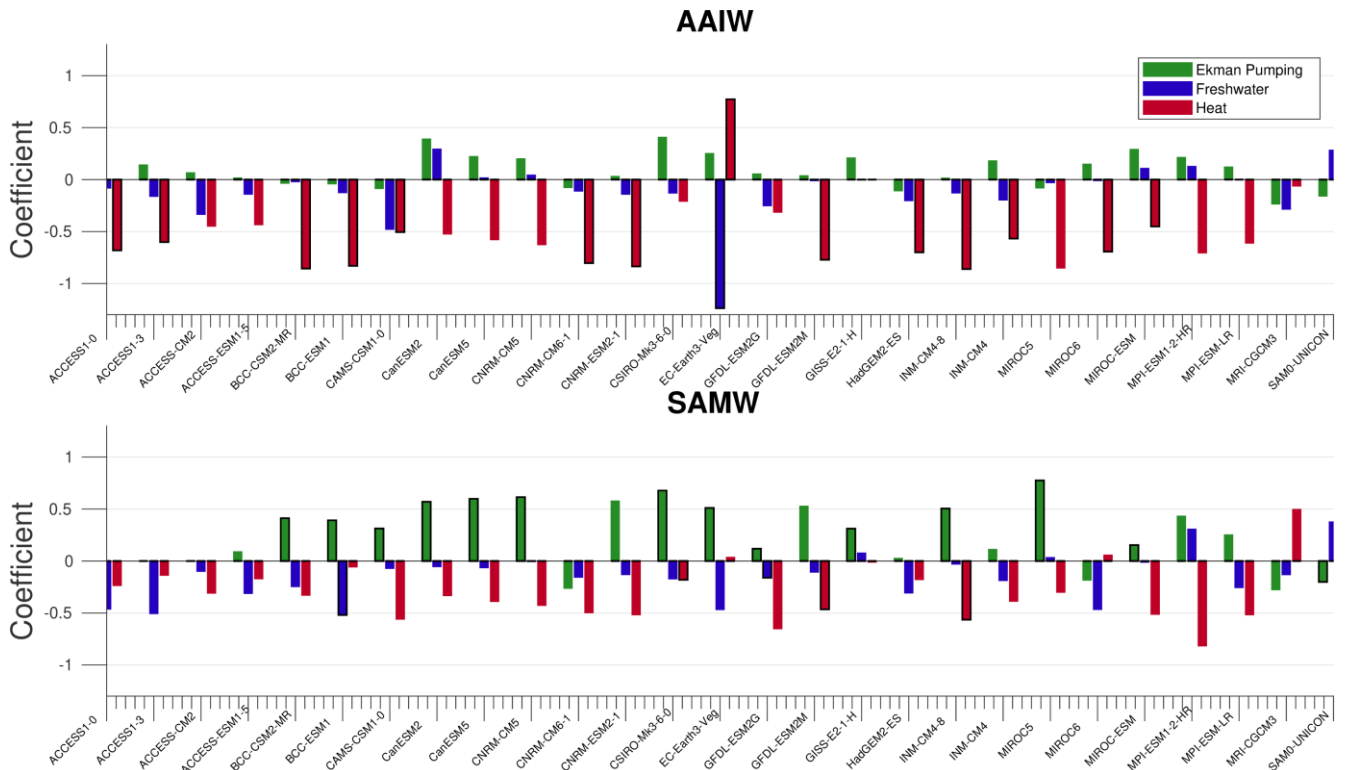


Figure 5.6. Coefficients from the multivariate regression for each model analyzed, the green bar represents the coefficient for Ekman pumping, blue for freshwater flux, and red for heat flux. AAIW is the top panel and SAMW below. The black contour represents the coefficients with partial correlations higher than 0.3 for models with multivariate R^2 values higher than 0.5.

5.2.5.3 Future Scenarios

To evaluate the future behavior of the AAIW and SAMW transports, we first analyzed the temporal changes in the air-sea fluxes during the 21st century for both S4.5 and S8.5 Scenarios (Figure 5.7). Almost all flux components showed changes for the future projections, presenting significant linear trends ($p<0.05$) over this period, with the only exception being the heat flux in the S4.5 scenario. Here, we determine the trend significance using a Mann-Kendall test, where a p-value lower than 0.05 confirms the statistical significance of the trend considered. Ekman pumping becomes more negative in time in both scenarios, following the southward displacement and intensification of the Southern Ocean westerlies with higher radiative atmospheric forcing, as shown by [Wang et al. 2013;

Bracegirdle et al. 2013]. The freshwater flux time series reveals a weakening trend in both scenarios, implying the difference between precipitation and evaporation is becoming smaller with time, which can potentially affect the low salinity signature of the AAIW core. The heat flux shows strong variability, but does not present a clear trend in the S4.5, while a clear increasing trend can be observed for the S8.5. The latter suggests the Southern Ocean may warm during the 21st century [Sen et al. 2009; Armour et al. 2016].

The changes in the fluxes are well correlated to the changes in AAIW and SAMW transports. The future export of these water masses has been calculated by the method described in Section 2.2. Thus, the water mass volume transport is derived directly from the model scenarios S4.5 and S8.5 output as was done earlier to calculate the water mass volume transports with PiControl and Historical outputs. Figure 5.10 reveals the AAIW export for scenario S4.5.

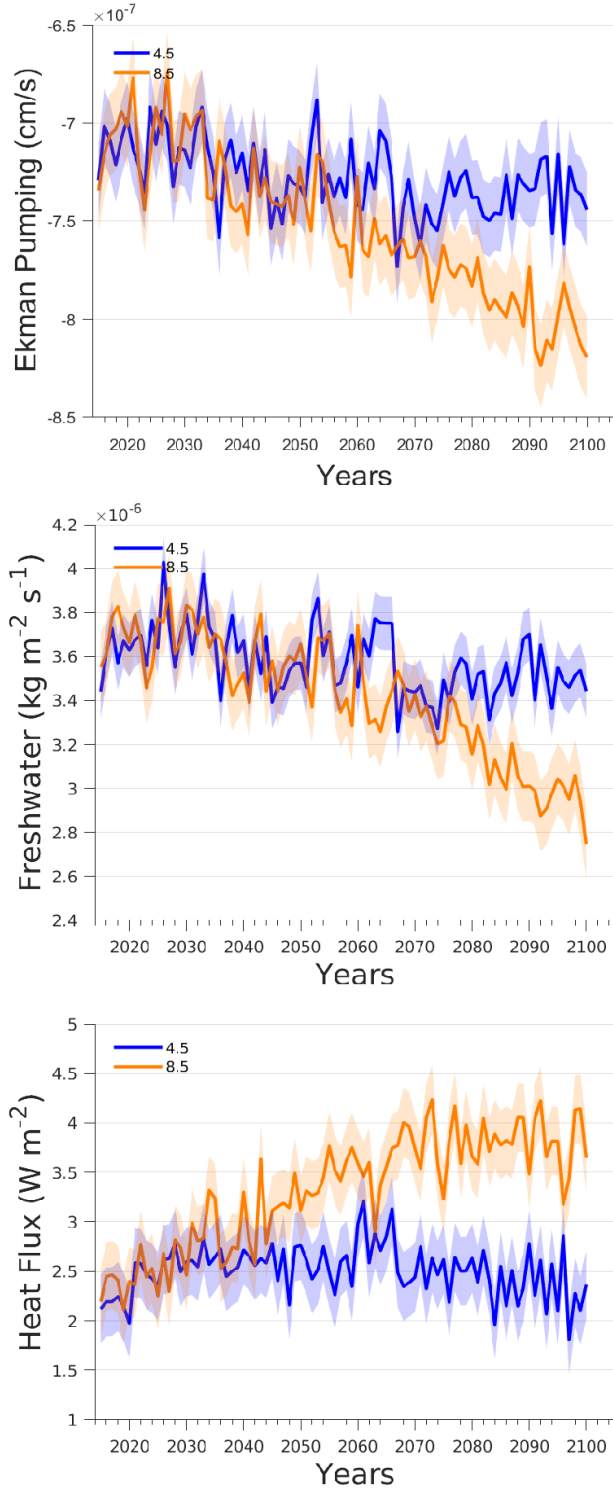


Figure 5.7. 21st century projections for the fluxes considered in this study. Top to bottom: Ekman pumping, freshwater, and heat fluxes. The S4.5 scenario is shown in blue and the S8.5 in orange, with the shading denoting the ensemble standard deviation.

The average transport is ~7.5 Sv. CSIRO-Mk3-6-0, INM-CM4-8 and MIROC5 have transports well below average, and GFDL-ESM2M, INM-CM4, and MPI-

ESM1-2-HR have values considerably higher than the average. In the S8.5 scenario the AAIW mean transport is ~7.8 Sv, with GFDL-ESM2M, INM-CM4, and MPI-ESM1-2-HR again showing values greater than the multi-model average. Comparing to the historical mean, an AAIW average transport increase of about ~1.5 Sv and ~1.8 Sv is observed for the S4.5 and S8.5 scenarios respectively (Figure 4). Regarding SAMW, the future mean export for the S4.5 is about ~14 Sv, with ACCESS-CM2, ACCESS-ESM1-5, and GFDL-ESM2M yielding transports well under the multi-model average. For scenario S8.5 the multimodel SAMW mean transport rises to ~14.8 Sv, with the same models cited above presenting lower than average values, while INM-CM4-8 and MIROC5 have values exceeding ~20 Sv. Compared to the historical mean, a SAMW average transport increase of ~3 Sv is observed by the end of the 21st century for S4.5, and the catastrophic S8.5 scenario has a modestly larger increase of ~3.8 Sv (Figure 4).

Figure 5.9 shows in blue lines the multi-model average AAIW and SAMW volume transport time series for the S4.5 and S8.5 scenarios. The AAIW export increases in both scenarios, presenting significant trends ($p<0.05$), going from 6.8~Sv to ~7.3 Sv in S4.5 and to 7.5~Sv in S8.5 by the end of the 21st century. That means an increase of ~0.006 Sv year⁻¹ in S4.5 and ~0.010 Sv year⁻¹ in S8.5. It is also noticeable that the S8.5 time series shows a slightly smaller transport than S4.5 up to around year 2050, but then accelerates and overtakes the S4.5 line by the end of the period. Conversely, the SAMW transport S4.5 time series does not show any significant trend, instead showing strong interannual variability around a mean of approximately ~12 Sv. In the same period, the S8.5 scenario presents a significant trend, estimating a ~0.5 Sv higher transport for SAMW by the end of

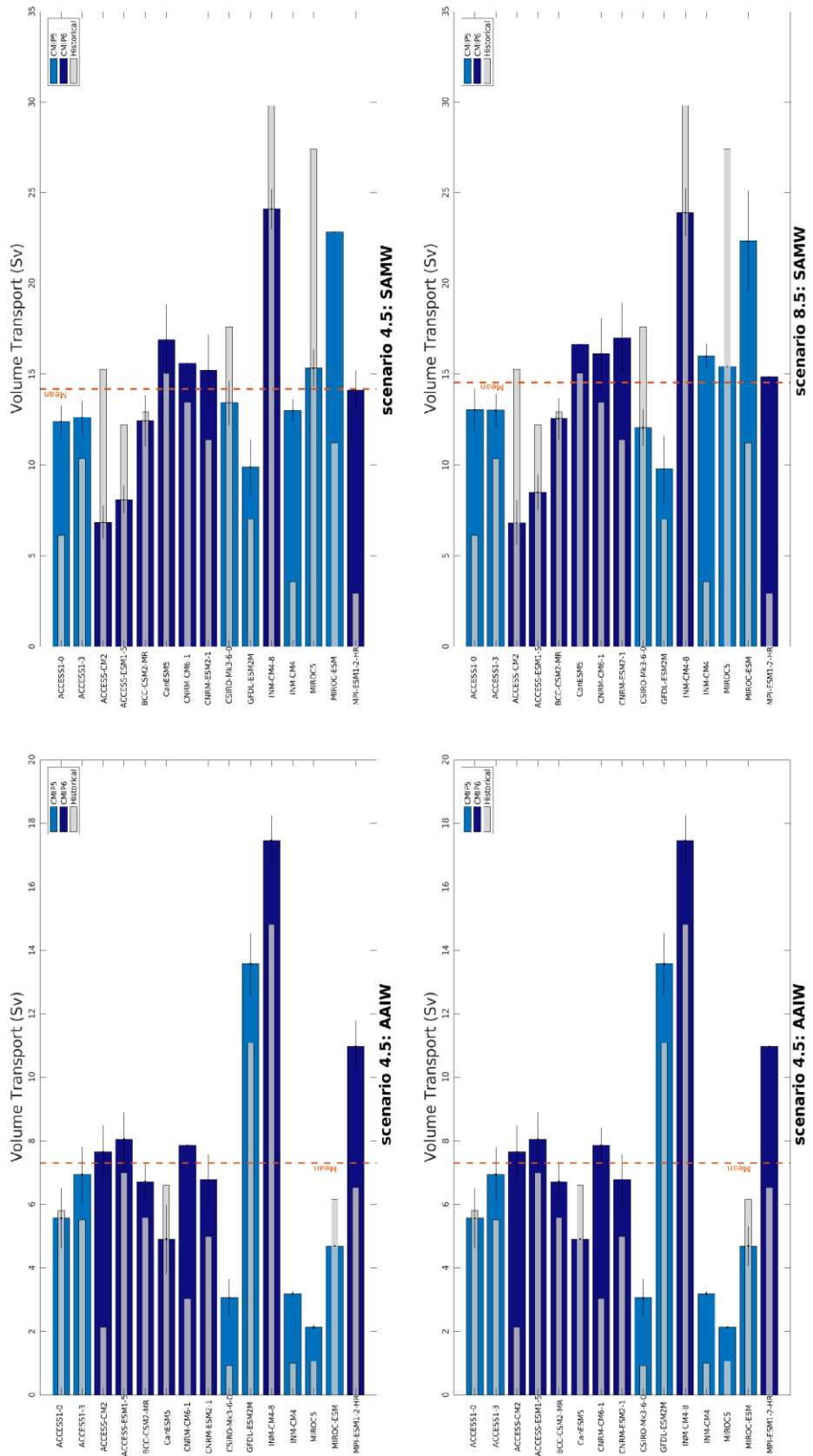


Figure 5.8. Same as Figure 2, but for future projections. At the top (bottom) the S4.5 (RS8.5) scenario. The dark blue bars represent CMIP6 and the light blue CMIP5 models. The mean

historical export for each model (Figure 2) are shown in gray bars. The average transports are highlighted in dashed orange lines, reaching values of 7.5 Sv for AAIW and 14 Sv for SAMW in S4.5, and values of 7.9 Sv for SAMW and 14.8 Sv in S8.5.

century with a rate of ~ 0.011 Sv year $^{-1}$. Thus the mitigation scenario resulted in important changes for air-sea fluxes and, consequently, to water mass behavior. The trends for S4.5 are minimal, whereas the catastrophic S8.5 scenario yields significant trends in the export of these intermediate water masses.

To address the mechanism by which these flux components impact AAIW and SAMW transports in the projections and test if they change from the previous scenarios, we again calculated a multivariate correlation between the exports and air-sea fluxes with these future scenarios (Figure 5.10). The multimodel mean coefficients from PiControl and Historical are also shown in figure 5.10 for comparison with the multimodel mean coefficients for the future scenarios. The R^2 values (not show here) do not yield relevant changes from the PiControl and Historical results presented above, with most models reaching values higher than 0.4. In the case of AAIW the models BCC-CSM2-MR, CanESM5, GFDL-ESM2M, MIROC5 and MIROC-ESM reach values higher than 0.6, while for SAMW this is true for models ACCESS1-3, ACCESS-CM2, ACCESS-ESM1-5, INM-CM4-8 and MIROC-ESM. Most models presented a slightly weaker correlation in the scenario S4.5 than in S8.5.

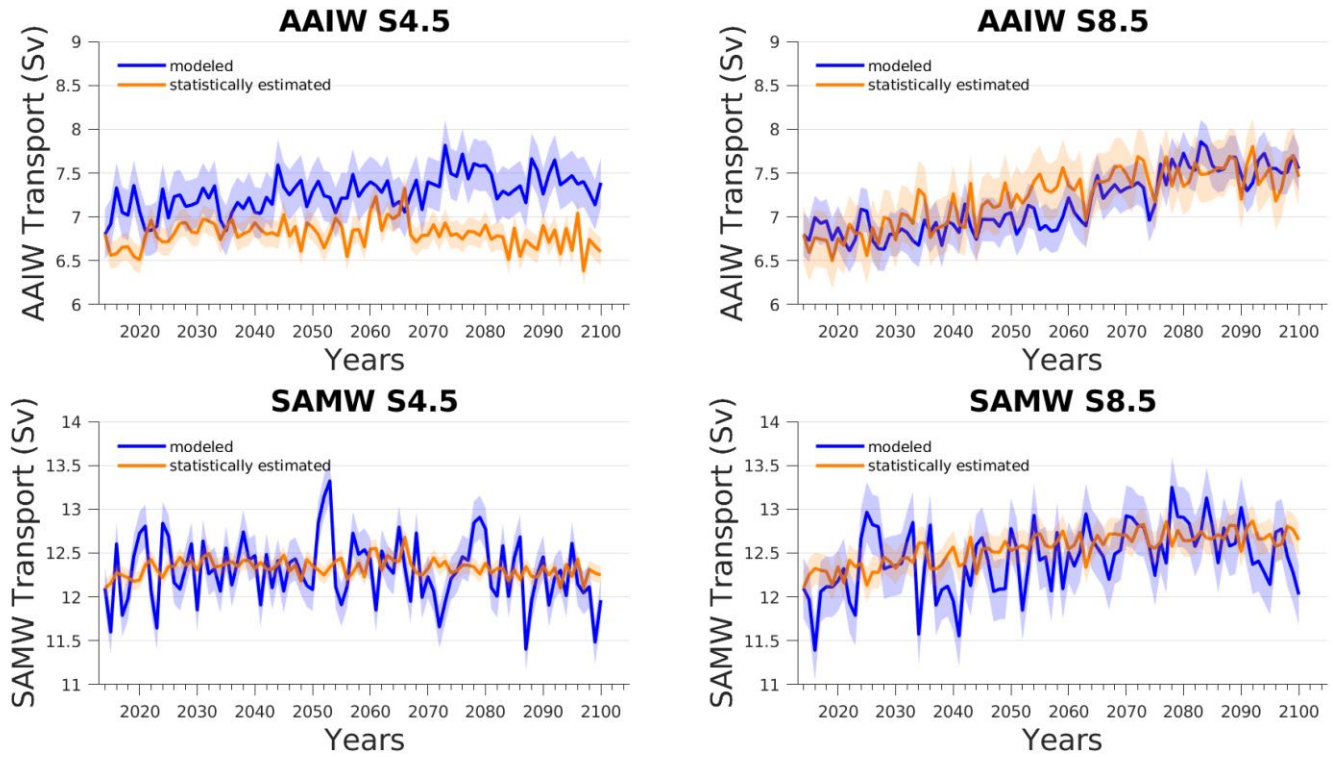


Figure 5.9. 21st century projections for transports of AAIW (top) and SAMW (bottom). The scenario S4.5 are presented on the left and S8.5 on the right. In blue are shown the exports calculated with temperature, salinity, and velocity outputs from future scenario experiment and in orange are the exports estimated for the future scenarios using the future fluxes and correlation coefficients derived from the PiControl/Historical. The shading gives the standard deviation of the ensemble.

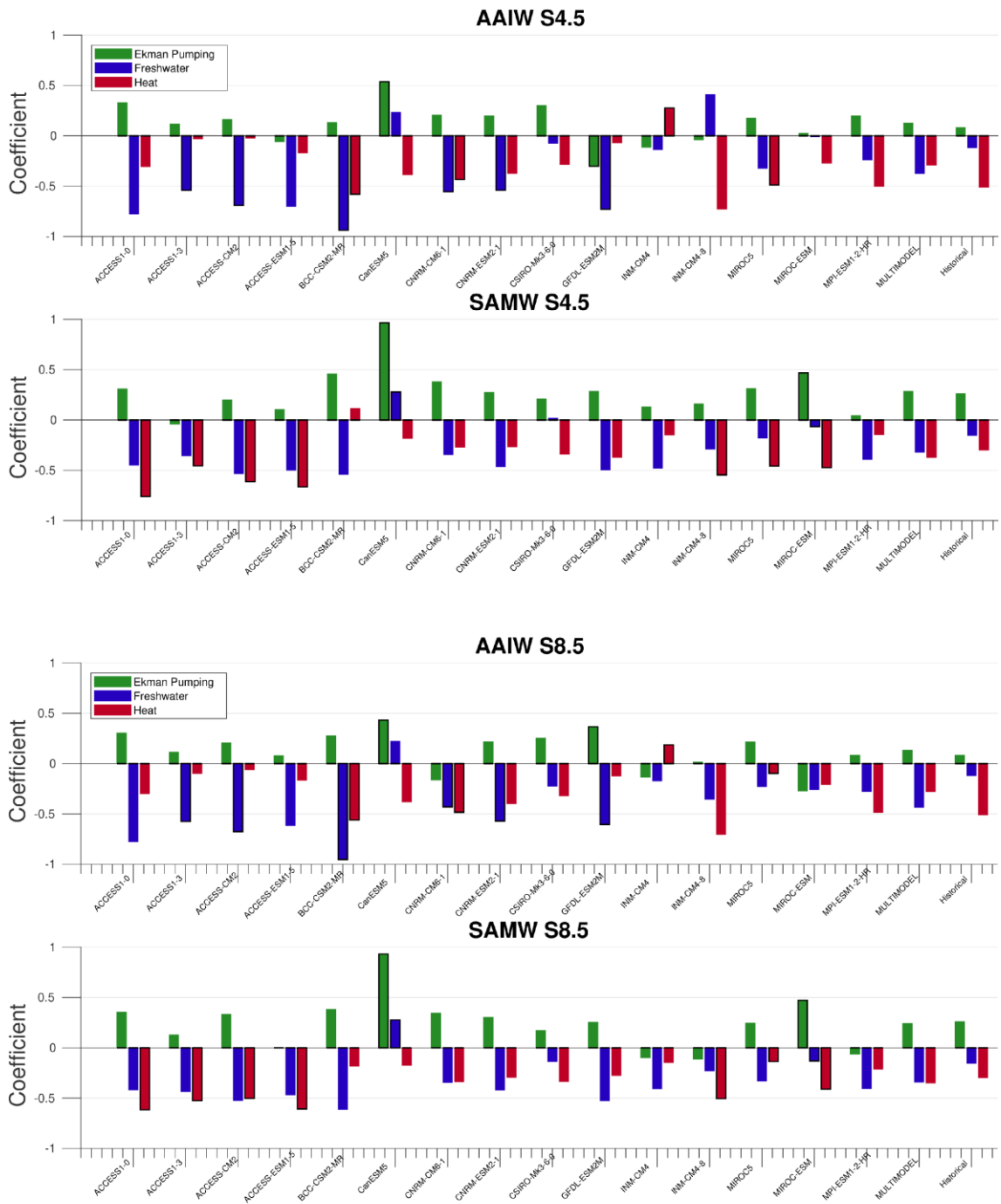


Figure 5.10. Multivariate regression coefficients for each model analyzed in the future scenario runs. The green bars represent the coefficients for Ekman pumping, blue for freshwater flux, and red for heat flux. The top two panels are, respectively, AAIW and SAMW coefficients for S4.5; and the bottom two panels are the same but for S8.5 scenario. The bars with a black contour represent the coefficients with partial correlations higher than 0.3 and multivariate R² values higher than 0.5.

5.2.5.4 Predictability

To estimate the prediction skill of AAIW and SAMW export computed with the coefficients from a multivariate regression based on a long term period, we projected the transports up to the end of the 21st century using the coefficients from PiControl and Historical results (Figure 5.6) and the fluxes from the future scenarios. In this way, we can provide a comparison between the transports calculated using these coefficients with what the models actually show (Figure 5.9), and thereby assess the robustness of our derived climate statistical relationships with respect to sensitivity on the background state.

Figure 5.11 shows in orange the multimodel mean volume transport of AAIW and SAMW predicted from the coefficients computed with the multivariate regression presented in Section 3.2. The predictions are initialized using the last year of the historical experiment for the initial state. The predicted water mass transports generally track the actual transports, lacking trends in the mitigation scenario (S4.5) and significantly trending in the most catastrophic scenario (S8.5). In the scenario S4.5, AAIW transport oscillates around ~6.7 Sv. Meanwhile in scenario S8.5, AAIW transports have a consistent trend to the end of 21st century, going from ~6.6 Sv to about ~7.5 Sv at a rate of ~0.012 Sv year⁻¹ (Table 3). The SAMW transports in scenario S4.5 oscillate around ~12.3 Sv, the same way as modeled, though with less variability. Like AAIW, the scenario S8.5 SAMW transports have a significant trend, with an increase from ~12.2 Sv to ~12.7 Sv by the end of 21st century, which implies a rate of ~0.008 Sv year⁻¹ (Table 5.2). Though SAMW and AAIW transports are rather steady in S4.5, they both do show modest peaks between 2060 and 2070. These are attributable to flux variability as can be

inferred from Figure 5.7, hence reinforcing the relative importance of heat flux in the PiControl/Historical results (Figure 5.6).

Table 5.2. Trends of water mass export for the future scenarios. AAIWm and SAMWm are the export trends calculated with temperature, salinity, and velocity model outputs from future scenario experiment (blue lines in Figure 11), while AAIWs and SAMWs are the export trends statistically estimated for the future scenarios using the future fluxes and correlation coefficients derived from the PiControl/Historical (orange lines in Figure 11). The p-value of the trend fit is given in parentheses, with a value less than 0.05 implying significance.

	Trend (Sv year^{-1})			
	AAIWm	AAIWs	SAMWm	SAMWs
Scenario 4.5	0.006 (10^{-6})	0.001 (0.12)	0.002 (0.09)	0.002 (0.15)
Scenario 8.5	0.010 (10^{-7})	0.012 (10^{-6})	0.010 (10^{-5})	0.008 (10^{-5})

Further correlating the statistically predicted water mass exports with calculated future multi-model means results in an R^2 for AAIW of 0.45 for S4.5 and 0.05 for S8.5. The R^2 for SAMW is 0.18 for S4.5 and 0.22 for S8.5. With the exception of AAIW in S4.5, the trends are reasonably estimated from coefficient reconstructions (Table 5.2). However based on R^2 values it is only this AAIW S4.5 case where the predictive skill is modest, and it is rather poor for the other cases. While the coefficients from PIcontrol and the historical analyses do not provide good predictive skill of the monthly transport variability, they are useful for projecting trends through the end of 21st century. Though the predicted variability is uncorrelated due to changing statistical relationships between transport and fluxes, it is an important result that the inter-annual to decadal projected variability is consistent with the modeled transport, as can be seen by the overlapping standard deviations in figure 5.9.

5.2.6 Conclusions

Consistent with the findings of [Sallée et al. \[2013\]](#), the mean volume transports of AAIW and SAMW at 30°S are highly variable across models, with simulated values that can be quite different from observed ones. Vertical resolution seems to be important in this regard, as models with higher vertical resolution generally show better performance in simulating AAIW/SAMW transports. Moreover, this seems to be independent of the vertical coordinate type used. We present here that the mean transports are also highly correlated to mean Ekman pumping across models. In contrast, the monthly transport variability from a single model is not adequately explained by the wind stress curl variability. Hence, one needs to consider other factors, such as freshwater and heat fluxes, in order to better explain the observed monthly variability.

The volume transport of AAIW and SAMW in the PiControl and Historical experiments have significantly higher R^2 values whenever the multivariate regression used considers Ekman pumping, heat flux, and freshwater flux together. Nevertheless, there is a dominance of heat flux for explaining the AAIW transport variance. There is not a dominant component for explaining SAMW variability, but Ekman pumping does appear as the most important flux. This is in agreement with Rintoul et al. (2002) that showed that Ekman transport dominates the SAMW property variability. Some models do not present a high R^2 due to intrinsic ocean process that can modulate the variability. Previous studies showed examples of such processes, such as formation of large polynya [e.g. [Heuze et al. 2013](#); [Azaneu et al. 2014](#)]. Moreover, the nonstationary coefficients computed for future scenarios, or lags changing with time, could also explain the observed differences in the correlations.

Most models had regression coefficients that were in agreement with theoretical expectations for how intermediate layer water export from the Southern Ocean is impacted by atmosphere-ocean fluxes [Marshall & Radko \[2003\]](#). There is more AAIW and SAMW export with increasing wind stress and buoyancy loss. This implies that though most models are exporting too much intermediate water, they are likely forming these water masses in consistency with theoretical expectations. However, there is also higher variability in the regression coefficient magnitudes across models (Figure 5.6). Also, it is intriguing that heat and freshwater, both drivers of buoyancy, present such different partial correlations. We credit this to the fact that our regressions are not local and there are differences in the sensitivities to local zones of water mass formation. There are regional variations in fluxes as well as ocean locations impacting the subduction pools. These regional variations and relationships should be explored in future work.

Almost all the fluxes analyzed present a significant linear trend for the 21st century future scenario simulations, with the only exception being the heat flux for the S4.5 scenario. Moreover, for all cases the S8.5 scenario shows stronger trends, reinforcing the importance of mitigation actions to achieve lower impacts in the climate system by the end of the 21st century. Changes in the fluxes impact the transport of AAIW and SAMW with the same pattern: higher trends in S8.5 compared to S4.5. This is different to that found by [Sallée et al. \[2013\]](#), where it was shown that water masses freshened, but exhibited small differences in the future mean export. It is important to emphasize that here we are considering also the outputs of the PiControl experiment and using some different CMIP5 models (here we used all models that presented the necessary data for the

experiments PiControl, historical, RCP4.5 and RCP8.5) and also augmented the analyses with CMIP6.

The AAIW and SAMW volume transports have significant trends in the S8.5 scenario. Regressions using the coefficients from Historical and PiControl and future fluxes are able to capture these trends. However, these statistical projections are not highly correlated to the transports calculated directly from the model output densities and velocities in the future scenarios. Thus, the linear response of water mass exports to fluxes are changing significantly in the 21st century. This non-stationary result means that climate models, as opposed to statistical models, are necessary for skillful deterministic predictions. Moreover, it demands that climate models must be properly initialized (i.e. they must represent the present state) and emphasizes the importance of validating climate model outputs with data.

Biases in the representation of intermediate layer water masses must be considered when studying the ocean circulation influence on the climate system. Some models show more realistic representation of water mass volume transports, but the reason is still unclear and should be further investigated. Here, we show high correlations to air sea exchanges, and thus one must look to fluxes as a possible explanation. One possible cause for export differences is resolution (table 5.1), as Lee et al. (2011) have shown that increasing model resolution can improve the representation of buoyancy fluxes and stratification in the Southern Ocean. However, we find that the correlation of export to air-sea fluxes does not show a sensitivity to model resolution. Perhaps the differences in resolution between the models tested here is insufficient to yield a relevant improvement in AAIW and SAMW export. Other things to consider in future works are differences

in how air-sea fluxes are parameterized in these models. Here we showed the water mass transport multimodel mean of CMIP6 models are more consistent with [Talley \[2003\]](#) results inferred from *in situ* data than previous generation models, but a large spread around the mean is still present. Considering the importance of the intermediate ocean layer to climate, the formation and export of these water masses should continue to be investigated with the goals of understanding the system and guiding improvements in coupled climate model fidelity.

5.1.7 Acknowledgments

This study is a contribution to the activities of the INCT-CRIOSFERA (CNPq grant 465680/2014-3 and FAPERGS grant 17/2551-0000518-0), the Southern Ocean Carbon and Climate Observations and Modeling (SOCCOM) and the Brazilian High Latitudes Oceanography Group (GOAL). The GOAL has been funded by the Brazilian Antarctic Program (PROANTAR) through the Brazilian Ministry of the Environment (MMA), the Brazilian Ministry of Science, Technology, Innovation MCTI), the Council for Research and Scientific Development of Brazil (CNPq;442628/2018-8), and CAPES Foundation (AUXPE 1995/2014). The CMIP outputs are available via Deutsches Klimarechenzentrum Data Center Portal (<http://esgf-data.dkrz.de>). We acknowledge the climate modeling groups for producing and making available their outputs. M. M. Mata acknowledges CNPq fellowship 306896/2015-0. L. Almeida acknowledges CAPES fellowships 88887.368463/2019-00 and 88887.370051/2019-00 in the scope of the CAPES-PRINT/FURG Project. M Mazloff acknowledges NSF awards PLR-1425989, OPP-1936222, OCE-1924388 and NASA award 80NSSC20K1076.

Capítulo VI: Análise Regional das AAIW/SAMW

O segundo manuscrito, de autoria de Almeida L., Mazloff M., Mata M.M., é intitulado “*On the regional distribution of Intermediate and Mode Water formation in the Southern Ocean in coupled climate models*” e foi recentemente submetido ao periódico “*Journal of Geophysical Research: Oceans*” e está em revisão no momento da apresentação desta tese.

6.1 Síntese do artigo

As massas de água AAIW/SAMW formam-se em algumas regiões específicas do oceano Austral, resultantes da combinação dos ventos de oeste, característicos da região, e mudanças na flutuabilidade destas águas devido aos fluxos de calor e água doce na interface ar-mar, que resultaram em uma subducção destas águas para profundidades inferiores à da camada de mistura. Neste artigo foram investigados os aspectos regionais da formação e exportação destas massas de água nos modelos CMIP6 através de correlações multivariadas em área entre os transportes de volume e os fluxos oceano-atmosfera ao sul de 30°S. Foi encontrado que a região com as maiores correlações é o leste do setor índico do oceano Austral. Todavia, outras regiões também apresentaram correlações significativas, como a área próximo à Passagem de Drake e ao sul da África. Estas regiões coincidem com as áreas de formação apresentadas na literatura, o que sugere que os modelos CMIP6 estão formando estas massas de água nas regiões corretas. Também, foi verificado as regiões por onde as AAIW/SAMW estão sendo exportadas para norte, ambas apresentando um padrão semelhante, com os maiores transportes nas bordas nos oceanos, principalmente nas bordas leste. Considerando, ainda, os cenários futuros, não foram encontradas mudanças significativas, tanto em relação às regiões de formação, como as regiões de exportações das massas de água, apresentando apenas pequenos decréscimos nos valores das correlações.

6.2 Artigo 2

On the Regional distribution of Southern Ocean Intermediate and Mode Water Formation in Coupled Climate Models

Lucas Almeida¹, Matthew R. Mazloff², Mauricio M. Mata¹

1 Laboratório de Estudos dos Oceanos e Clima - LEOC, Programa de Pós-Graduação em Oceanologia – PPGO, Instituto de Oceanografia, Universidade Federal do Rio Grande-FURG, Rio Grande, RS, Brazil

2 Scripps Intuition of Oceanography, University of California San Diego, San Diego, CA, USA

Corresponding author: Lucas Almeida, lucasralm@gmail.com

Key Points:

- AAIW and SAMW are formed with spatial accuracy in the models.
- AAIW/SAMW are mostly exported in the boundaries of the basins oceans
- The formation processes and patterns persist in future climate change scenarios.

Submitted to Journal of Geophysical Research: Oceans – in review

6.2.1 Abstract

The Southern Ocean provides a route to sequestering heat and carbon dioxide from the atmosphere to the deep ocean. Part of the heat uptake occurs during the formation of Antarctic Intermediate Water (AAIW) and Subantarctic Mode Water (SAMW). Formation of these waters occurs as part of the upper limb of the Meridional Overturning Circulation (MOC), and is fundamental to the global climate balance. AAIW and SAMW are formed in specific regions of the SO from a combination of intense winds and buoyancy fluxes that lead to convection, thick mixed layers, and then wind-driven subduction. AAIW and SAMW then flow northward and ventilate the intermediate layers of the subtropical gyres. Here we investigate regional aspects of the AAIW and SAMW formation in CMIP6 models through multivariate correlation analysis between the meridional transport of these water masses and air-sea fluxes. Specifically we consider Ekman pumping, freshwater fluxes, and heat fluxes. First, we show that the highest correlations are found in the eastern Indian sector of the SO. The results also show high correlations to air-sea fluxes in the southeast Pacific and south of Africa, suggesting a good representation of AAIW/SAMW formation regions in CMIP6 models. Analysis of the meridional transports of the water masses at 30°S shows that AAIW/SAMW are exported from the same regions of the SO. We also consider IPCC future scenarios (SSP4.5 and SSP8.5) to evaluate the possible changes in those regional aspects by the end of 21st century, performing the same multivariate correlation between projected water mass exports and air-sea fluxes. We find the same pattern of formation regions as in the historical runs with a slight decrease in correlation coefficients, but with changes in terms of transport intensity.

6.2.2 Plain Language Summary

The ocean plays a fundamental role in the climate system storing and transporting significant amounts of heat and carbon. In particular, water mass changes that occur in the Southern Ocean play an important role in setting the interior properties of the global ocean. Here, we use a set of climate models to investigate aspects of the system affecting that oceanic transport and storage, focusing on the intermediate layer water masses. These intermediate waters that are exported from the Southern Ocean to the rest of the global oceans are known as Antarctic Intermediate Water (AAIW) and Subantarctic Mode Water (SAMW). The main goal of this study is to determine the regions that those water masses are forming and their variability and how those water masses aspects may be impacted in the future due to climate change. We find that AAIW and SAMW are mostly subducted in the same regions in current and future projections, and with most climate models showing the correct formation areas according to present knowledge. As with the observed ocean, climate models show AAIW/SAMW being exported to the north primarily in the western side of the ocean basins. In the future scenarios we do not detect drastic changes as the formation regions remain the same, but there are some notable differences from the historical period, especially in terms of transport intensity.

6.2.3 Introduction

The Southern Ocean provides a route to sequestering heat and carbon dioxide from the atmosphere to the deep ocean [[Sabine et al. 2004](#); [Sallée et al. 2012](#)]. According to [Roemmich et al. \[2015\]](#) this region accounts for 67% - 98% of the observed heat content increase in the global ocean. Part of the heat storage

occurs during the formation of Antarctic Intermediate Water (AAIW) and Subantarctic Mode Water (SAMW). This formation is an important component of the upper limb of the Meridional Overturning Circulation (MOC) and plays a fundamental role in the global climate balance [Talley et al. 2003; Pahnke et al. 2008]. These water masses are also linked to the global carbon and nutrients cycles [Sarmiento et al. 2004; Sabine et al. 2004; Sallée et al. 2012]. The AAIW/SAMW are formed in specific regions of the SO, where intense winds combined with buoyancy fluxes between atmosphere and ocean result in thick mixed layers [deBoyer et al. 2004]. Those processes lead to AAIW/SAMW subduction and the subsequent ventilation of the subtropical gyres at intermediate layers [Sallée et al. 2010].

The processes governing the formation rates of AAIW and SAMW are still not well characterized, but several mechanisms have been proposed [Zhu et al. 2018]. The residual mean theory applied by Marshall [2003] combines patterns of wind forcing, buoyancy forcing, and stratification to infer the MOC, and thus subduction magnitudes to intermediate layers. According to this framework, the volume of AAIW and SAMW exported from the Southern Ocean should be strongly associated with wind stress and air-sea fluxes of freshwater and heat. Some studies have quantified the volume transport of water masses exported from the Southern Ocean in previous Coupled Modeling Intercomparison Project (CMIP) simulations. It has been shown that there are large biases in the export of AAIW in CMIP5 models [Sallée et al. 2013; Zhu et al. 2018]. Moreover, Sallée et al. [2013] studied the mean water mass transport across 30°S in a multi-model ensemble and related it to mean outcrop region, heat and freshwater fluxes. Recently, Almeida et al. [2021] showed a high correlation of AAIW and SAMW

transports across 30°S with the wind stress and air-sea fluxes in CMIP models of generation 5 and 6 (CMIP5 and CMIP6), suggesting reasonable formation processes of these water masses in most of those models. However, there remains a knowledge gap regarding the regional spatial aspects of the AAIW/SAMW formation (e.g. locations, spatial variability) in those CMIP models. Several studies have shown that Southern Ocean intermediate water formation occurs in proximity to the Subantarctic Front, supplied by the Circumpolar Deep Water (CDW) [Sloyan et al. 2001; Hartin et al. 2011]. Here, we investigate regional aspects of the AAIW and SAMW formation in the CMIP6 models, assessing the meridional transport of these water masses and then comparing with air-sea fluxes across the Southern Ocean. We are especially interested in the mechanisms that are forcing the formation and exports and how they are varying at time and space between models. Finally, Climate and Earth System Models (ESMs) are important tools for making quantitative climate projections to the end of 21st century, enabling assessment of the impact of different scenarios of anthropogenic activity on climate [Bracegirdle et al. 2020]. Utilizing these projections in CMIP6 we also estimate potential future changes of AAIW and SAMW formation spatial patterns and rates under different scenarios of climate change.

6.2.4 Materials and Methods

6.2.4.1 Models

Outputs from 17 CMIP models from version 6 [Eyring et al. 2016] are used in this study. Atmospheric and oceanic component variables were downloaded from the *Deutsches Klimarechenzentrum Data Center portal* (<https://esgf-data.dkrz.de>).

The list of models and respective resolutions is presented in Table 6.1. To analyse the models performance and the natural time variability, we used monthly averages of the ocean state from the “historical” runs, which is a scenario forced by natural and anthropogenic factors during the 20th century. We also use the CMIP6 models future scenario runs to estimate the behavior of AAIW and SAMW source regions up to the end of the 21st century. These future runs are generated using prescribed radiative forcing values from the Shared Socioeconomic Pathways (SSP; [Eyring et al. 2016](#)). In this case, we use the scenarios 4.5 W.m⁻² (SSP4.5) and 8.5 W.m⁻² (SSP8.5) which are the medium range and the most catastrophic ones, respectively.

Table 6.1. Climate Coupled Models used in this study. Some details for each model are presented: name, ocean and atmospheric horizontal resolution, ocean vertical coordinate and number of levels, the origin institution and main reference.

Model	Ocean (Lat x Lon)	Atmospheric (Lat x Lon)	Vertical (levels)	Institution	Reference
ACCESS-CM2	1.00° x 1.00°	1.88° x 1.25°	50	CSIRO	Dix et al. (2019)
ACCESS-ESM1-5	1.00° x 1.00°	1.88° x 1.25°	50	CSIRO	Ziehn et al. (2019)
BCC-CSM2-MR	1.00° x 1.00°	1.13° x 1.10°	40	BCC	Wu et al., (2018)
CESM2	1.12° x 0.46°	0.90° x 1.25°	60	CESM	Danabasoglu et al. (2019)
CMCC-CM2-SR5	1.00° x 1.00°	0.90° x 1.25°	50	CMCC	Cherchi et al. (2019)
CanESM5	1.00° x 1.00°	2.81° x 2.81°	45	CCCma	Swart et al. (2019)
CanESM5-CanOE	1.00° x 1.00°	2.81° x 2.81°	45	CCCma	Swart et al. (2019)
CNRM-CM6-1	1.00° x 1.00°	1.40° x 1.40°	75	CERFACS	Volodoire (2018)

CNRM-ESM2-1	$1.00^\circ \times 1.00^\circ$	$1.40^\circ \times 1.40^\circ$	75	CERFACS	Seferian (2018)
GISS-E2-1-G	$1.25^\circ \times 1.00^\circ$	$2.50^\circ \times 2.00^\circ$	32	GISS	NASA/GISS (2018)
INM-CM4-8	$1.00^\circ \times 0.56^\circ$	$2.00^\circ \times 1.50^\circ$	48	INM	Volodin et al. (2019)
MIROC6	$1.00^\circ \times 0.70^\circ$	$0.70^\circ \times 0.70^\circ$	62	AORI	Tatebe & Watanabe (2018)
MPI-ESM1-2-HR	$0.44^\circ \times 0.44^\circ$	$0.94^\circ \times 0.94^\circ$	40	MPI	Schupfner et al. (2019)
MPI-ESM1-2-LR	$0.44^\circ \times 0.44^\circ$	$2.00^\circ \times 2.00^\circ$	40	MPI	Mauritsen et al. (2019)
MRI-ESM2-0	$1.00^\circ \times 0.50^\circ$	$1.13^\circ \times 1.13^\circ$	61	MRI	Yukimoto et al. (2019)
NESM3	$0.98^\circ \times 0.49^\circ$	$1.90^\circ \times 1.90^\circ$	46	NUIST	Cao et al. (2018)
UKESM1-0-LL	$1.00^\circ \times 1.00^\circ$	$1.00^\circ \times 1.00^\circ$	75	MOHC/UK	Tang et al. (2019)

6.2.4.2 Definition of Water Masses

The AAIW and SAMW exported from the Southern Ocean in each CMIP model may be found in different density classes than observed in the real ocean. Thus, to identify these water masses, we applied the methodology presented in [Sallée et al. \[2013\]](#) to find the most appropriate potential densities for each respective CMIP model and for each experiment analyzed in this study. The method defines the water masses by hydrographic properties, as follows: AAIW is associated with a salinity minimum in the circumpolar belt region [[Tomczak 2007](#)], while the SAMW is related to stratification minimum, and hence Potential Vorticity (PV) minimum.

The process first identifies a salinity minimum location (S_{\min}) with a local salinity maxima directly above ($S_{\max(\text{above})}$) and below ($S_{\max(\text{below})}$). The limits of AAIW are, in terms of density space, a quarter of the distance between S_{\min} and S_{above} (S_{below}) for the upper (lower) end, as shown in the following equations:

$$\sigma_2(\text{acima}) = (3\sigma_2(S_{\min}) + \sigma_2(S_{\max(\text{acima})})) / 4 \quad (1)$$

$$\sigma_2(\text{abaixo}) = (3\sigma_2(S_{\min}) + \sigma_2(S_{\max(\text{abaixo})})) / 4 \quad (2)$$

The procedure above was carried out for each model at 30°S, where the total thickness H and transport of AAIW VH were calculated.

To identify the SAMW, we analyzed the PV at 30°S. First, the upper limit of AAIW is identified as being the lower limit of SAMW. Then, we search for a minimum PV level associated with a density vertical gradient smaller than 0.1 kg.m⁻³. The SAMW layer is determined as having an upper density limit that contains at least 90% of the total local PV minimum.

After determining the upper and lower potential density limits, it is straightforward to calculate the SAMW thickness, H , and export, VH for each climate model.

To obtain the total volume of each water mass crossing 30°S, we vertically integrate the monthly mean meridional velocity over each water mass layer. Thus, we determine the total intermediate and modal water volume transport at 30°S as a monthly time-series. This time series is then used to investigate the formation process in CMIP models.

6.2.4.3 Air-sea Fluxes

The Ekman pumping (W_e) is calculated from the zonal and meridional components of surface wind stress, as the following Equation 3:

$$W_e = \nabla_x \left(\frac{\tau}{\rho_0 f} \right) \quad (3)$$

where τ is the wind stress component, ρ_0 is the reference seawater density and f is the Coriolis parameter. A monthly average Ekman pumping time series is obtained from all grid cells of each model considering the whole the Southern Ocean between latitudes 30°S and 70°S.

The total ocean and atmosphere heat exchange is also calculated for the entire Southern Ocean between latitudes 30°S and 70°S in each model. The total heat flux, Q , is given by:

$$Q = -hfss - hfsls + rlds + rlus + rsds + rsus \quad (4)$$

Where $hfss$ and $hfsls$ are the sensible and latent heat fluxes, $rlds$ and $rlus$ are the downwelling and upwelling net longwave radiation, $rsds$ and $rsus$ are the downwelling and upwelling net shortwave radiation, respectively.

Finally, the freshwater fluxes are calculated by the difference between precipitation and evaporation, $F = P - E$, over the same area. A salinity restore is necessary as global climate models typically drift over decadal timescales [Griffies et al. 2016], so all models used salinity surface restoring with different implementations [Danabasoglu et al. 2014; Rahaman et al. 2020], which potentially influence the estimates of freshwater fluxes. However, it is important to highlight that we do not expect a strong impact on our results as the typical restoring timescales are far longer than the monthly variability considered in the present study.

We also calculate the September mean MLD for each grid point of each model using the same definition as [Sallée et al. \[2013\]](#), which is a potential density difference criterion of 0.03 kg m^{-3} from the surface. We also calculated the MLD with the Roemmich-Gilson Argo Climatology [[Roemmich et al. 2009](#)], using the September mean from 2004 to 2018, aiming to compare the model results with the true ocean.

6.2.4.4 Multivariate Regression Procedure

To identify the regions that have more correlation between the air-sea fluxes and the AAIW/SAMW transport a multivariate regression procedure is performed using the same lag months from [Almeida et al. \[2021\]](#), which are no lags for Ekman pumping, 2 months for freshwater fluxes and 3 months for heat fluxes. To enable direct comparison of all variables of interest (VH , W_e , F , Q), we remove the mean from the time series, and then normalize by dividing the time series by its standard deviation. The multivariate regression was computed to each point in latitude and longitude for all three fluxes to the spatially integrated water mass transport timeseries across 30°S .

To enable direct comparison of all variables of interest (VH , W_e , F , Q), we remove the mean from the time series, and then normalize by dividing the time series by its standard deviation. We then carry out a multi-variate regression to inform how much the variation of water masses transport, $y = VH$, can be explained by the Ekman Pumping and fluxes of freshwater and heat:

$$y = Ex + \varepsilon \quad (5)$$

Here E is the matrix of predictor variables (W_e , F , Q), and thus size $NT \times 3$, where NT is the length of the time series, and x is a 3×1 vector of regression

coefficients. As shown in [Wunsch \[2006\]](#), the solution for x that minimizes the squared residuals, ε , is

$$x = (\mathbf{E}^T \mathbf{E})^{-1} \mathbf{E}^T y \quad (6)$$

The normalized variance of VH that can be explained by (W_e , F , Q) is:

$$R^2 = 1 - (y - \mathbf{E}x)^T (y - \mathbf{E}x) (y^T y)^{-1} \quad (7)$$

with $R^2 = 1$ implying 100% of the variance can be explained.

We also carry out this analysis for each independent predictor variable alone to evaluate if one variable can do a similar job explaining the variance as to what is accomplished using all three. We also test which time lags best explain the water mass transports for each individual component.

The fluxes analyzed are not completely independent between themselves. To address this problem, we calculate partial correlations in an attempt to infer the level of independence between the forcing components. To achieve this goal, we first remove the signal correlated with other variables before determining R^2 . Thus, we first determine the component of y that is orthogonal to the two other predictor variables (e.g. W_e , F) via regression, and then determine the variance explained, R^2 , of this residual signal, y' , that can be explained by the remaining predictor (e.g. Q). For example, to assess the partial correlation of the Ekman pumping with the water mass exports, we first remove the signal of export correlated to freshwater and heat fluxes, and then determine an R^2 for the residual export signal with Ekman pumping. The same was done for each flux component.

$$y' = y - \mathbf{E}_{ij}x \quad (8)$$

$$R_p^2 = 1 - (y' - \mathbf{E}_k x)^T (y' - \mathbf{E}_k x) (y'^T y')^{-1} \quad (9)$$

where the $E_{ij}x$ is the multivariate regression using 2 predictor variables, i and j , and Equation 10 gives the R^2 value for the partial correlation of the third variable, k .

6.2.5 Results

6.2.5.1 Sothern Ocean characteristics

The latitudinal averaged (between 30°S and 70°S) air-sea fluxes vary widely across longitudes as shown in figure 6.1. The Ekman pumping is positive in most areas, consistent with an integration to the very south of the Southern ocean, where the Circumpolar Deep Water (CDW) is upwelling to the surface. An exception is the Indian Sector, where the values are positive close to the coast and negative in the middle ocean. The representation of Ekman pumping across models is consistent in most areas, showing a standard deviation smaller than 0.5 m s⁻² (green shadow in figure 6.1), with the Indian sector being having the largest spread. The freshwater flux (blue line in figure 6.1) is consistent across models, with standard deviations in all regions less than 0.18 10⁻⁵ kg m⁻² s⁻¹. The Atlantic and Indian sectors show a similar pattern with strongest negative values in the western portion that decreases towards the east. The variability in the Pacific sector is small when compared to the other areas, except close to South America. The heat flux is a different story, however, with the models showing wide ranges of values and thus high standard deviations in most regions. Nevertheless, they agree in terms of flux direction (i.e., the signal) in most cases. The heat flux, represented by the red line in figure 6.1, also presents a higher zonal variability, where the Atlantic sector shows positive values in most regions (the only exception is near the African coast), while the Pacific and Indian sectors show negative values, representing heat flux from the ocean to the atmosphere.

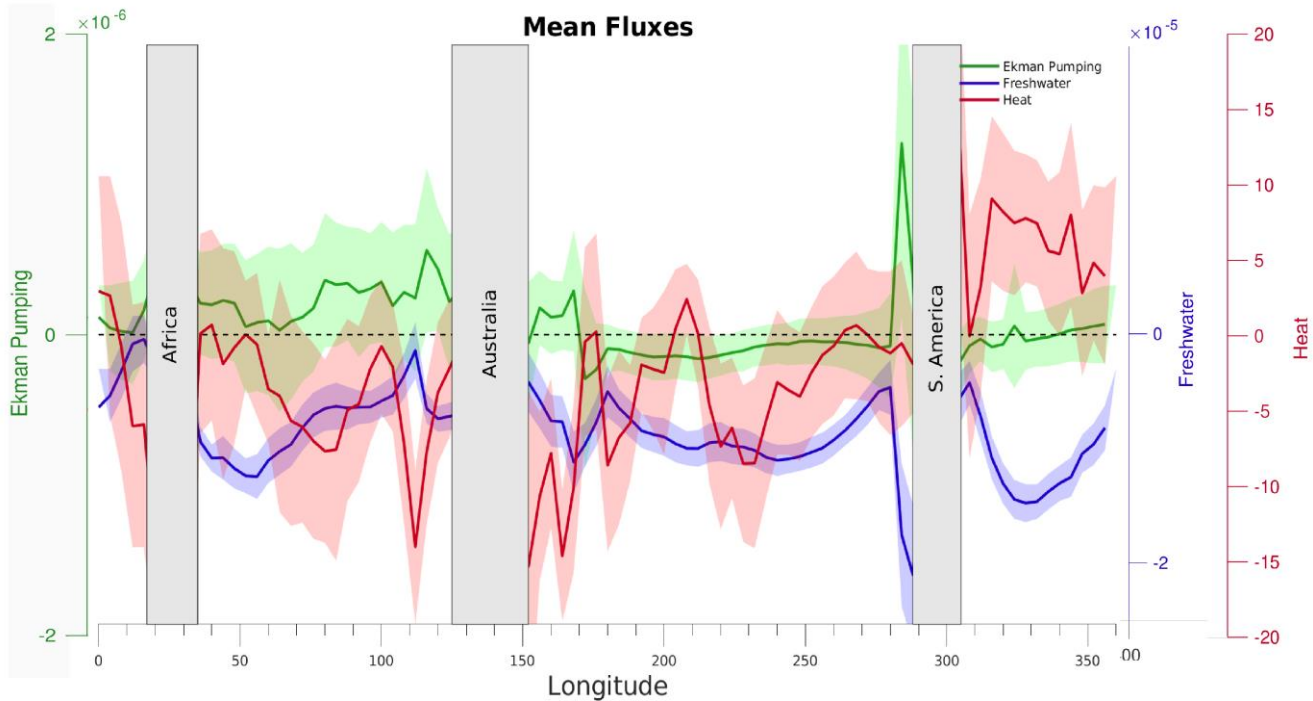


Figure 6.1. Cross-model mean of the air-sea fluxes between 30°S and 70°S. The green line denotes Ekman pumping (m.s^{-1}), the blue line represents the freshwater flux ($\text{kg.m}^{-2}.s^{-1}$), and the red line represents the heat flux (W.m^{-2}). The shadows are the standard deviation for the respective color.

The mixed layer depth (MLD) is another diagnostic of the SO state with a fundamental relationship to intermediate and mode water formation. [Sallée et al. \[2010\]](#) states that these water masses acquire their physical and biogeochemical properties in circumpolar bands of thick mixed layers before they are subducted and flow northwards to ventilate the subtropical gyre thermoclines. [Hong et al. \[2021\]](#) showed that biases in the representation of SAMW formation regions are directly linked to MLD bias in the CMIP6 models. [Downes et al. \[2010\]](#) pointed out that CMIP models from previous generations showed a bias in the SO MLD representation. Moreover, [Sallée et al. \[2013\]](#) showed strong MLD variability across CMIP3 and CMIP5 models. They also diagnosed that most models had a winter MLD too shallow and stratified when compared with observations.

Some CMIP6 models present an improvement in the representation of buoyancy advection and stratification, and thus more realistic MLDs [[Lee et al. 2011](#)]. The winter MLD (annual September mean) for each model is shown in figure 6.2. We find a high cross-model variability, with some models presenting too shallow a winter MLD compared with the Argo product, as was found in CMIP5 models [[Sallée et al. 2013](#)]. That is the case for CESM2, CNRM-CM6-1, CNRM-ESM2-1, CanESM5-CanOE, CanESM5, GISS-E2-1-G and MPI-ESM1-2-LR, and these models also show reduced intermediate and mode water mass formation [[Almeida et al. 2021](#)]. However, there are other models that show a deeper MLD, which is closer to what is expected for the SO. These models are ACCESS-CM2, BCC-CSM2-MR, CMCC-CM2-SR5 and UKESM1-0-LL. It is important to highlight that most models present a large latitudinal band of the deepest MLD, that could lead to the overestimation of AAIW/SAMW transports.

Mixed Layer Depth

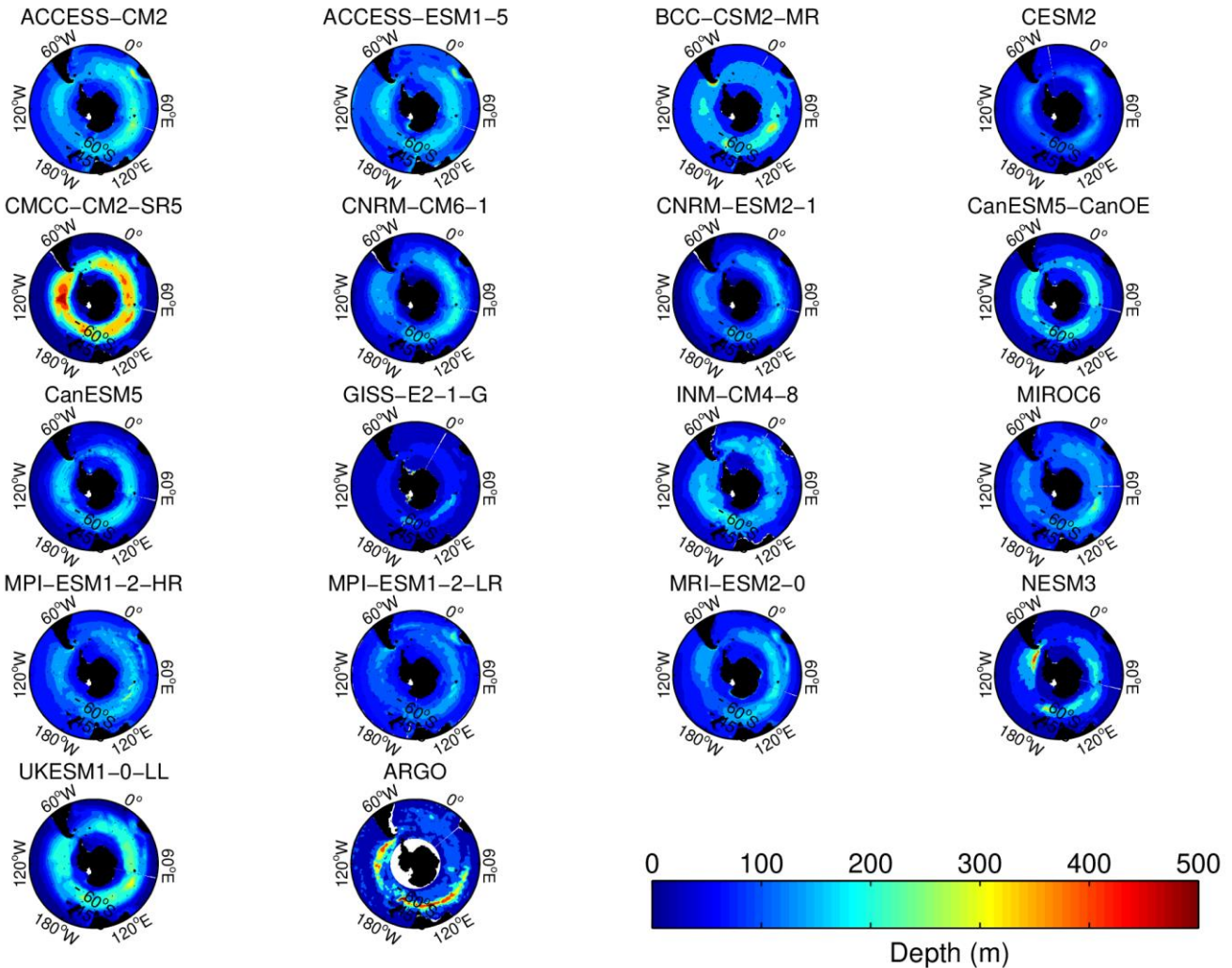


Figure 6.2. Winter mixed-layer depth (in meters) averaged over the historical experiment for each model, the last one is the winter mixed-layer estimated with the Argo climatology, using the September mean from 2004 to 2018.

6.2.5.2 Regional Formation of AAIW/SAMW

AAIW is mainly subducted at the Subantarctic Front (SAF; [Sloyan et al. 2001](#)). It is primarily supplied by the upwelled Circumpolar Deep Water (CDW) that flows northward forced by Ekman transport. SAMW is formed north of AAIW formation region, in the wintertime where the MLD is deepest [[Sallée et al. 2010](#)]. These waters decrease temperature and increase density from west to east [[Sallée et](#)

al. 2006]. Several studies have identified the formation zones of intermediate waters in the southeast of Atlantic, Pacific and Indian ocean sectors of SO [e.g. Hartin et al. 2011; Downes et al. 2017; Gao et al. 2018; Boland et al. 2021].

The multivariate correlation of the AAIW/SAMW transport with the buoyancy fluxes and Ekman pumping are presented in figure 6.3. The region with the strongest correlation for both water masses is the southeastern Indian Ocean, reaching R^2 values of 0.5 for AAIW and 0.6 for SAMW. This is a typical formation region for SAMW [e.g. Sallée et al. 2006; Sallée et al. 2010; Boland et al. 2021]. It is interesting to note that AAIW is mainly centered between 40°S and 55°S while SAMW is centered further to the north of 40°S, which suggest the typical position of SAF along this latitudinal band. These are also the region of highest model spread, as shown by the standard deviation in the Figure 6.3, reaching values of 0.15 for SAMW. Moreover, most models presented the deepest region of MLD in the southeast part of the Indian sector.

The southeastern Pacific sector is also recognized as an important formation region of intermediate and mode water masses [e.g. Sallée et al. 2010; Hartin et al. 2011]. Here, the models have a R^2 of around 0.4 for AAIW, in the southeast Pacific and 0.5 close to 40°S (Figure 6.3). SAMW reach values of R^2 of 0.6 at the location of the SAF in the multi-model mean circulation. This area of the Pacific here identified as being correlated with forcing is similar to the areas of AAIW/SAMW formation presented by Hartin et al. [2011] from an analysis of chlorofluorocarbons distribution. A realistic representation of water mass formation in these regions by the models is especially important considering that the densest mode water variety is expected to be formed here [Holte et al. 2013]

and then to be exported north to Pacific Ocean and also to Atlantic Ocean through Drake Passage [Sallée et al. 2010].

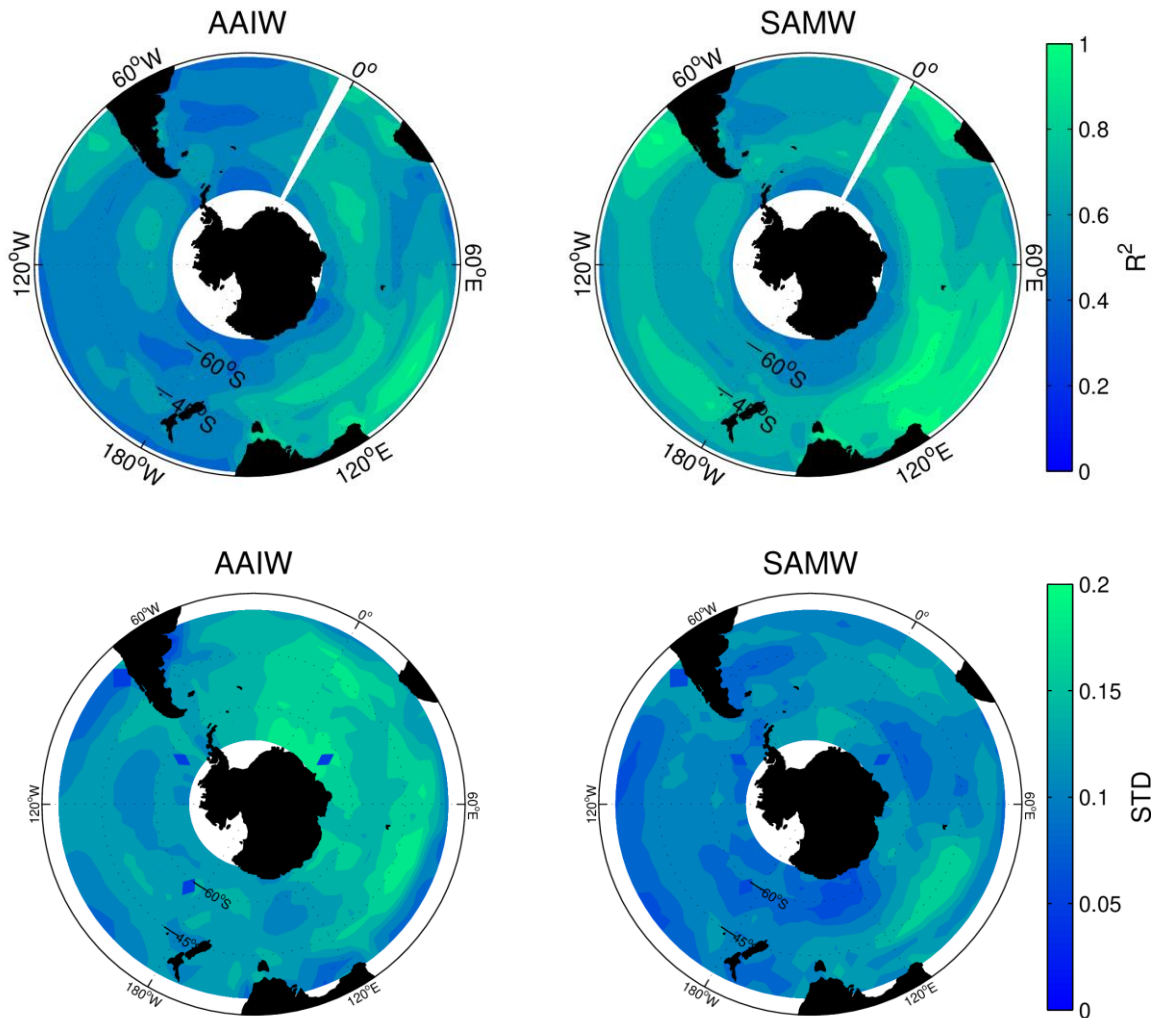


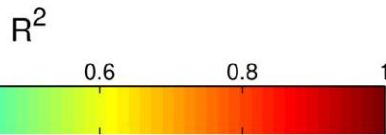
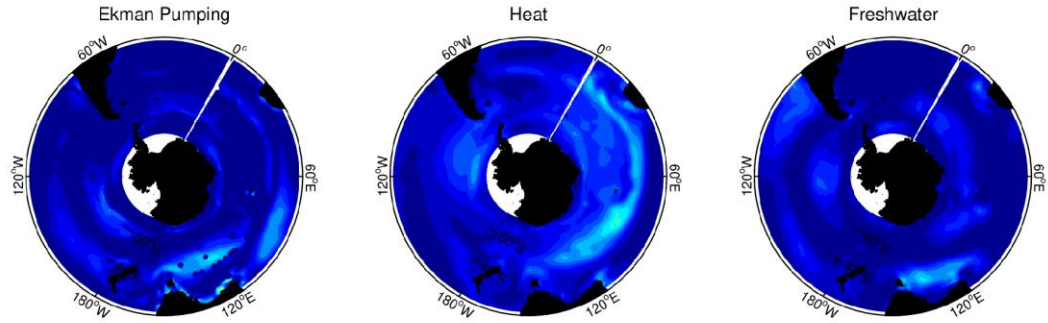
Figure 6.3. The top two panels are the multi-model mean R^2 from the multivariate correlation for each water mass (AAIW left and SAMW right) using the historical experiment. The multivariate correlation are between the Export of each water masses and the combination of Ekman pumping, freshwater flux and heat flux. The bottom panels are the standard deviation between the R^2 result of each model.

In the Atlantic sector the models presented a small correlation between AAIW/SAMW and the fluxes, where the pools are shallower and smaller when

compared to other sectors [Boland et al. \[2021\]](#). This is consistent with the fact that the Atlantic sector has shallower MLDs [\[Downes et al. 2017\]](#). One of the pools of formation lies in the west of the South Atlantic, between 60°W and 0° [\[Boland et al. 2021\]](#). However, most models do not present a high correlation in this areas ($R^2 < 0.2$, figure 6.3), the exceptions ($R^2 > 0.4$) are CanESM5, CMCC-CM2-SR5, CNRM-ESM2-1, GISS-E2-1-G, MPI-ESM1-2-HR and MRI-ESM2-0 for AAIW and ACCESS-ESM1-5, CNRM-CM6-1, CNRM-ESM2-1, MPI-ESM-1-2-LR and MRI-ESM2-0 for SAMW. The multi-model mean presents a higher correlation in the area close to South Africa, reaching a R^2 of 0.5 for both water masses (figure 6.3). That can be due to the strength of Agulhas leakage governing the export of intermediate water in the region. In most models, the Atlantic sector presented the lowest correlation values and therefore lower variability when compared to the rest of SO, possibly as a consequence of a change in the buoyancy flux (switching to a positive heat flux) in this area (figure 6.1).

To explore the main cause of the values of the multivariate correlation we plot the individual correlations of each flux component and the water mass exports (figure 6.4). The results highlight the expected regions for the AAIW variability, with the heat fluxes showing high values in the Indian sector, and the Ekman Pumping and freshwater flux in the region south of Australia. Meanwhile SAMW shows a strong dominance of the heat fluxes in the entire circumpolar region. For both water masses a combination of the three forcing results in a higher variance explained of the exports of each water mass, implying each component is important to the export (Figure 6.3).

R^2 AAIW Historical



R^2 SAMW Historical

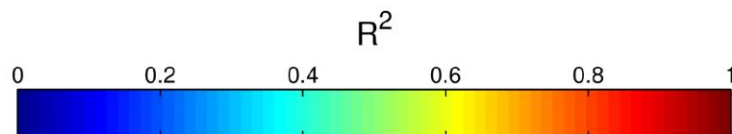
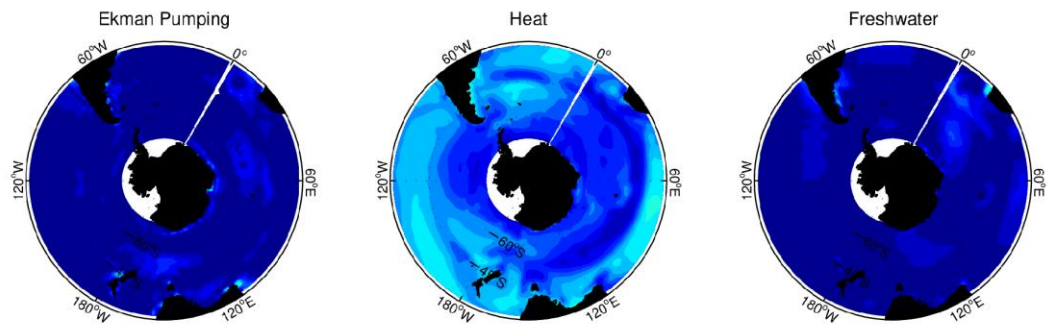


Figure 6.4. The top three panels are the individual correlations of Ekman pumping, heat and freshwater fluxes with the export of AAIW. The bottom panels are the same correlation but with the SAMW transport.

6.2.5.3 Meridional Transports

The intermediate and mode water masses are subducted in specific regions of the Southern Ocean (pools) and then are exported to the interior [Sallée et al. 2010]. In this section, we aim to investigate the regions where AAIW/SAMW are being exported to the north of their formation areas in the CMIP6 models. The Figure 6.5 shows the model mean transport (Sv) of these water masses at 30°S at each point of longitude. The transports are positive (northward direction) in almost the entire section, with the exception being some weak poleward flows at eastern boundaries and also some strong ones at western boundaries. These Southern Hemisphere western boundary currents are the Agulhas current (Indian), the East Australian current (Pacific) and the Brazil current (Atlantic). Both water masses here analyzed present quite similar transports across longitudes, but with some specific differences as shown in the bottom panel of figure 6.5. Both present the strongest transports in the western boundaries, with Atlantic being weakest when compared to the other sectors. In the open ocean regions the transports are northward and average around 1 - 2 Sv per degree of longitude. The main differences are found in the eastern boundaries, especially in the Atlantic sector where the Agulhas leakage occurs. In that region AAIW presents a weak transport (~1 Sv), while SAMW reaches values of about ~5 Sv, making this an important area of mode water export in the models analyzed. The opposite is found in the Indian sector eastern boundary, with AAIW presenting a higher transport (~4 Sv) and SAMW presenting a lower transport. In the east Pacific Ocean, SAMW slowly increases export towards South America, reaching values of ~5 Sv, while AAIW shows a small decrease at similar longitudes.

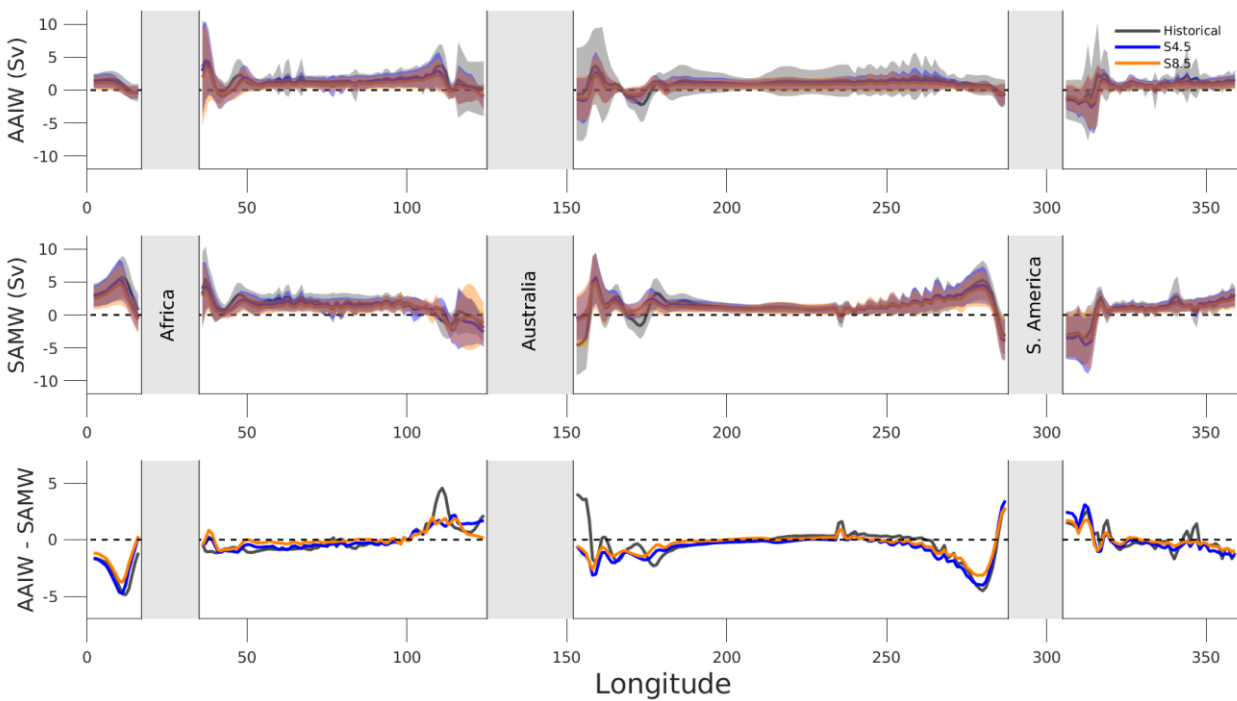


Figure 6.5. The top two panels are the multi-model mean of meridional transport at 30°S in the layers of AAIW (top panel) and SAMW (middle panel), with positive values representing a northward export. The last panel is the difference between the transport of AAIW and SAMW. Each color represents one experiment, gray are historical, blue are SSP4.5 and orange are SSP8.5.

The eastern Pacific, close to the Drake Passage, is an important mixing region for both water masses, with a higher decadal variability, intrinsically related to El Niño Southern Oscillation (ENSO) and the Southern Annular Mode (SAM, [Naveira et al. 2009](#)). Here, the models presented a high correlation between the water masses exports and the air-sea fluxes, suggesting that in these location the air-sea forcing are impacting the water masses export. In the Eastern Pacific sector, AAIW are not being exported, as showed in the upper panel of figure 6.5. While SAMW presented a strong northward export from this region, reaching values about 7 Sv, in agreement with the results of [Jones et al. \[2016\]](#).

The southeast Indian Ocean is an important region where Indian intermediate water mixes with waters from the Pacific Ocean [[Talley et al. 1996](#)]. This area

presented the strongest multivariate correlation (figure 6.3) in the multi-model mean for both water masses, and also had largest model spread. The heat flux individual correlations (figure 6.4) presents higher values in the region, however to reach such high values it is necessary to also consider the Ekman pumping and freshwater fluxes. The high multivariate correlation do not reflect the local meridional exports (figure 6.5) as we do not identify this area as an important export region in the models. In the SAMW layer the volume transport has negative values, probably associated with a "anomalous" effect of Leeuwin Current in the SAMW layers. Above this layer, AAIW is being transported north from the east Indian region, reaching values close to ~4 Sv, consistent with the transport of this water mass from the Perth Basin filling out the intermediate basin of Indian sector [Yao et al. 2017].

6.2.5.4 Future Scenarios

The multivariate correlation of AAIW/SAMW transports with the buoyancy fluxes and Ekman pumping in the future scenario SSP4.5 (top) and the correlation difference from the historical experiment (bottom) are presented in figure 6.6. The pattern of the multivariate correlation in this scenario is quite similar to the historical run, but with a small increase of the correlation in the higher correlation areas of AAIW formation. The individual correlations (not shown for future scenarios) revealed that it is due to a increase in the correlation of Ekman pumping, mainly in the Indian southeast region, implying the increasing westerlies are the main cause of the variability of AAIW to the end of 21st century in the scenario SSP4.5. Conversely, SAMW presents a small correlation decrease over the whole SO, caused by a diminished correlation to heat fluxes. The region with the strongest correlation for both water masses are also the

southeast Indian Ocean, reaching R^2 values of 0.6, where SAMW are predominantly formed north of AAIW formation. This is also the region with the greatest difference from historical experiments, reaching R^2 differences of 0.2, mainly for AAIW. The other water mass formation regions are also present in this scenario, with the southeastern Pacific reaching correlation values of 0.5 for AAIW and 0.6 for SAMW, respectively. Similar values are found for the Indian sector, but over a somewhat larger area. A small correlation in the east of the Atlantic sector close to Africa is also evident, where AAIW shows a slightly increased correlation while SAMW has the opposite behavior.

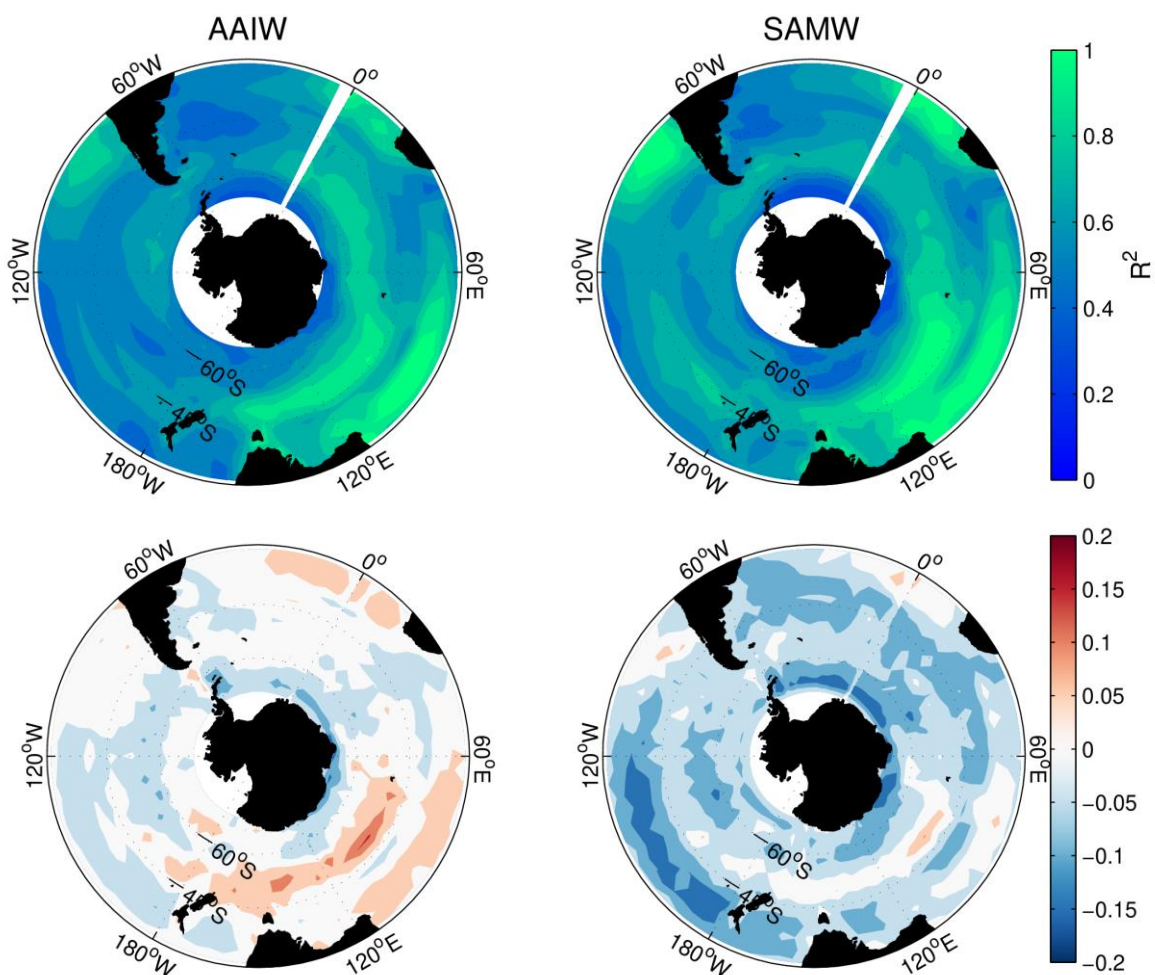


Figure 6.6. The top two panels are the multi-model mean R^2 from the multivariate correlation for each water masses (AAIW left and SAMW right) using the mitigation future scenario (SSP4.5). The multivariate correlation are between the Export of each water masses and the combination

of Ekman pumping, freshwater and heat fluxes. The bottom panels are the difference between these R^2 and the multivariate correlation in the historical experiment, where positive values means a correlation increase for the future scenario.

Furthermore, we also calculate the same multivariate correlation of AAIW/SAMW transport with the buoyancy fluxes and Ekman pumping in the more catastrophic future scenario SSP8.5. The results are shown in figure 6.7, where the top panel is the multivariate correlation and the bottom panel the differences from the historical experiment.

In this SSP8.5 scenario the differences from the historical runs increase in all the regions and the correlations have smaller values. However, the regional pattern remains the same as in the previous scenario: with the east of Indian sector showing the strongest correlations, now reaching values close to 0.5, while the southeastern Pacific and Atlantic have smaller but still relevant correlations of about ~0.4 (but for a smaller area). The decrease of the R^2 correlation varies from 0 to 0.2 in the SO, with the Pacific Ocean being the most affected region. The individual components of the correlation shows that in the case of AAIW, the differences are mainly caused by a small decreased correlation to the Ekman pumping and freshwater fluxes. While for SAMW the differences from the historical experiment are caused by a strong decrease of the heat correlation. This result agrees with [Almeida et al. \[2021\]](#) who found that the correlation coefficients to winds and freshwater increases for AAIW in the future scenarios and that the heat fluxes dominate the correlation for SAMW.

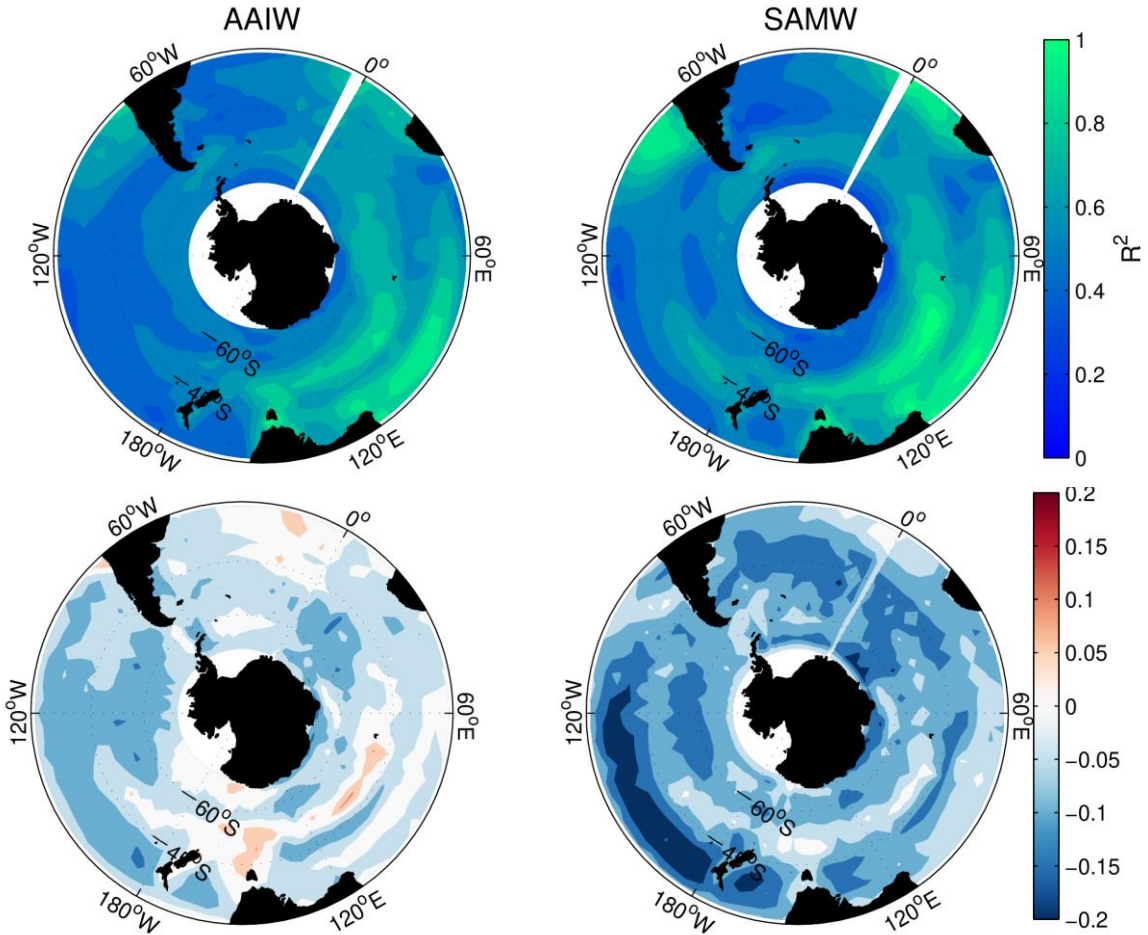


Figure 6.7. The top two panels are the multi-model mean R^2 from the multivariate correlation for each water masses (AAIW left and SAMW right) using the mitigation future scenario (SSP8.5). The multivariate correlation are between the Export of each water masses and the combination of Ekman pumping, freshwater flux and heat flux. The bottom panels are the difference between these R^2 and the correlation in the historical experiment.

These correlation differences could reflect the export of AAIW/SAMW, as shown in the meridional transports (Figure 6.5) where the blue lines are the transport of the mitigation scenario (SSP4.5) and the orange the catastrophic one (SSP8.5). First, the pattern of the transport are similar to the one presented for the historical experiment (gray lines). The AAIW are mainly exported northward, both in the eastern and western boundaries of the Indian sector and also the western boundary of the Pacific and Atlantic sector. At the same time, SAMW flows northward in only in the western boundary of the Indian sector, both sides of the

Pacific and in the eastern boundary of the Atlantic Ocean. The transport values (Sv) are also quite similar, in most sections they overlap each other. For AAIW the higher differences are in both boundaries of Indian Ocean, where the transport presented a slight decrease and in the Agulhas current domain where the transports increase in the future scenarios. In the SAMW case, the main differences are close to the coast of South America, in the Pacific side, the transports decrease in the future scenarios and in the Atlantic side the volume transport presented an increase in the southern flow associated with the Brazil current.

The difference between the water masses are shown in the last panel of Figure 6.5. As expected, the higher differences are concentrated in the longitudes of stronger transport of each water mass. In most longitudes, the zonal sections show small differences between the water masses from the historical to the future scenarios. A small decrease in the east Pacific sector is dominated by a change in SAMW flux, and a change in the east Indian sector reflects AAIW presenting a stronger transport. An opposing pattern is observed in the west Pacific sector and west Atlantic sector, where the differences with respect to the historical runs increase in the future scenario for both water masses.

6.2.6 Conclusions

There are numerous process that influence the subduction of waters to the intermediate layers of the SO and the subsequent northward export of these water masses. These include the westerlies forcing Ekman pumping, convection in mixed layers due to air-sea fluxes, and mixing processes along the circumpolar region [e.g. [McCartney et al. 1982](#); [Sloyan et al. 2001](#); [Sallée et al. 2010](#)]. Some

studies have revealed a strong correlation between these mean process in couple climate models [e.g. [Sallée et al. 2013](#); [Almeida et al. 2021](#)]. Here, we adopted a regional approach to understand where the AAIW/SAMW exports are sensitive to air-sea exchanges forcing and how this areas change in the future scenarios in the SO using CMIP6 models.

The Ekman pumping and the buoyancy flux analysis showed high meridional variability in the historical experiment (figure 6.1), reflecting a variability in the regions where the water masses of interest are being subducted. The MLD also presented a high cross-model variability, as was found in the previous generation CMIP5 [[Sallée et al. 2013b](#)]. As with this previous generation, some of the models still had too shallow winter MLDs. However, some of the models here analyzed simulated the MLD more realistically, with a deeper winter MLD (ACCESS-CM2, ACCESS-ESM1-5, BCC-CSM2-MR, CMCC-CM2-SR5 and UKESM1-0-LL). At this point we cannot identify what is causing these differences in the MLD results. It could be due to differences in the position and strength of the westerlies, parameterizations in the models, the refinement of spatial resolution or, more likely, a combination of these multiple factors. However, resolution alone is not the cause, considering that some models with a better horizontal resolution and at least with the same vertical resolution did not perform as well as other models (e.g. comparing the higher resolution MPI-ESM1-2-HR to the lower resolution MPI-ESM1-2-LR).

The multivariate correlation between the volume export of AAIW/SAMW and Ekman pumping, freshwater and heat fluxes showed the regions that are impacting the transport of these water masses. The correlation distribution patterns are quite similar between AAIW/SAMW, but with some differences

between them. For example, SAMW presented a correlation slightly higher and in most regions more northerly than AAIW. Most models presented a high correlation to SAMW in areas previously described in the literature as the regions of SAMW formation [e.g. [Aoki et al. 2007](#); [Sallée et al. 2010](#)]: the southeastern Indian Ocean, south of New Zealand and in the southeast Pacific. Moreover, these are the same regions associated with AAIW formation, plus the polar zone to the southeast Pacific, where changes in the Bellingshausen Sea have been associated to properties changes of these water mass [[Naveira et al. 2009](#)]. Despite all the uncertainties in the representation of SO MLD, we find the correct pattern of relationships of the water mass transports with the air-sea fluxes suggesting the CMIP6 models seem to have an accurate representation of the AAIW/SAMW source/export regions.

The water masses formation pools are not located necessarily where the water masses will be exported northward, as showed in the case of SAMW in [Sallée et al. \[2010\]](#). The meridional transport at 30°S (figure 6.5) unveiled the regions where AAIW/SAMW are being exported northward to eventually ventilate the interior of the south hemisphere subtropical gyres. The western boundary of the three oceans sectors showed a peak in the volume transport for both water masses, which is associated with advection from the swift subtropical western boundary currents. We also detected an AAIW northward transport in the east of Indian sector, while for SAMW additional flows are found in the east of the Atlantic the Pacific Oceans.

The regions with the highest correlation of AAIW/SAMW exports do not change from the historical experiment to the future scenarios here analyzed. However, the correlation intensity changes, and surprisingly in a different way for the future

scenarios. In the mitigation scenario (SSP4.5) the correlations became higher typically by 0.1 in the main AAIW formation regions (from the historical scenario), while SAMW correlations decrease, mostly in the Pacific sector formation area by almost 0.2. The latter can be related to a warmer surface in the outcroup region in the future scenarios [Hong et al. 2021], in agreement with the individual correlation that showed a higher difference for the heat flux. The most catastrophic scenario (SSP8.5) showed a correlation (R^2) decrease for both water masses across the whole SO. We suggest that the main cause is the significant trend in the forcing (Ekman Pumping and buoyancy fluxes) in this scenario, which is not detected in the SSP4.5 as shown in Almeida et al. [2021]. Moreover, the strong poleward shift of the westerlies [Downes et al. 2017] in the catastrophic scenarios can also play a major role in that process. We found that the individual correlations showed a significant decrease in the Ekman pumping correlation for the AAIW transport. The differences in the meridional volume transports in AAIW/SAMW layers are almost undetectable, suggesting that this aspect of the circulation remains stable in future scenarios.

Several studies have shown some bias in the process of formation and transformation of AAIW/SAMW in coupled climate model [e.g Sallée et al. 2013b; Zhu et al. 2018; Almeida et al. 2021]. This could result from some model intrinsic issues, such as MLD bias [Sallée et al. 2013b], model transport variability [Sallée et al. 2013] or resolution limitations [Lee et al. 2011]. In this sense, we have shown in the present study that CMIP6 models can represent the source regions of these water masses quite accurately. The formation regions tend to be mainly in the southeast of Indian Ocean, but we also find a strong correlation in the southeast Pacific Ocean as well. Also, these regions do not seem to change in

the future scenarios considered. Due to the importance of the intermediate layer of the ocean to climate, the change properties of AAIW/SAMW should continue to be investigated in future scenarios of the climate models, with an emphasis on the regional properties.

6.2.8 Acknowledgments

This study is a contribution to the activities of the INCT-CRIOSFERA (CNPq grant 465680/2014-3 and FAPERGS grant 17/2551-0000518-0), the Southern Ocean Carbon and Climate Observations and Modeling (SOCCOM) and the Brazilian High Latitudes Oceanography Group (GOAL). The GOAL has been funded by the Brazilian Antarctic Program (PROANTAR) through the Brazilian Ministry of the Environment (MMA), the Brazilian Ministry of Science, Technology, Innovation MCTI), the Council for Research and Scientific Development of Brazil (CNPq;442628/2018-8), and CAPES Foundation (AUXPE 1995/2014). The CMIP outputs are available via Deutsches Klimarechenzentrum Data Center Portal (<http://esgf-data.dkrz.de>). We acknowledge the climate modeling groups for producing and making available their outputs. The RG Argo climatology data were collected and made freely available by the International Argo Program and the national programs that contribute to it. (<http://www.argo.ucsd.edu>, <http://argo.jcommops.org>). The Argo Program is part of the Global Ocean Observing System. M. M. Mata acknowledges CNPq fellowship 306896/2015-0. L. Almeida acknowledges CAPES fellowships 88887.368463/2019-00 and 88887.370051/2019-00 in the scope of the CAPES-PRINT/FURG Project. M Mazloff acknowledges NSF awards PLR-1425989, OPP-1936222, OCE-1924388 and NASA award 80NSSC20K1076.

Capítulo VII: Síntese da Discussão e Conclusões

Neste trabalho foram investigadas as representações das massas de água AAIW e SAMW nos modelos CMIP. Primeiramente foram quantificados os transportes de volume em 30°S, identificando os modelos com valores mais próximos de estimativas *in situ*, e quais os fluxos oceano-atmosfera de maior importância para explicar a variabilidades destes transportes, em cenários presentes e também de mudanças climáticas futuras. Na segunda etapa do trabalho foram identificadas as áreas onde as massas de água estão se formando, comparou-se este resultado com estimativas do oceano real e verificou-se se estas regiões fontes são modificadas nos cenários futuros considerados.

Os modelos estudados apresentaram uma alta variabilidade em relação aos transportes médios de volume das AAIW/SAMW em 30°S, com relevantes diferenças dos resultados de trabalhos com dados *in situ* na mesma região. Em relação à AAIW, os modelos apresentaram resultados médios de 2 a 18 Sv, enquanto para SAMW obteve-se de 3 a 30 Sv. Neste contexto, a resolução vertical parece ter um papel chave (independentemente do tipo de coordenada vertical utilizada no esquema numérico), onde os modelos que apresentaram valores mais próximos ao esperado foram os de mais alta resolução vertical como, por exemplo, os *CNRM-CM6-1*, *CNRM-ESM2-1* e *EC-Earth3-Veg*, todos com 75 níveis verticais. Em uma correlação multi-modelo, foi constatado que os transportes de volume médio são altamente correlacionados com as médias de bombeamento de Ekman, mas individualmente apenas esta variável não explica a variabilidade mensal destes transportes. Para tal, é necessário levar em conta as outras forçantes, como fluxos de calor e de água doce.

A média dos transportes de volume foi de 6,15 Sv para AAIW e 11,29 Sv para SAMW. Levando-se em conta apenas os modelos geração CMIP6, os transportes médios de volume das AAIW e SAMW foram de 7 Sv e 10 Sv, respectivamente. Isto resulta em 17 Sv de transporte na camada intermediária sendo exportado do oceano Austral, valor ainda alto se comparado com os 10 Sv apontados em [Talley et al. \[2003\]](#), mas mais próximo dos 14 Sv relatados por [Ferster et al. \[2018\]](#), ambos estudos realizados utilizando dados *in situ*. Os valores ainda são superestimados nos modelos do CMIP6, mas parecem ter melhorado nesta nova geração, o que pode ser por conta de uma melhor representação das forçantes atmosféricas. [Beadling et al. \[2018\]](#) apontam para uma consistente melhora na representação do estresse do vento, enquanto

[Bracegirdle et al. \[2018\]](#) mostraram que os modelos CMIP6 tiveram significante melhora na representação dos jatos de oeste na região do oceano Austral. As correlações multivariadas apresentaram um R^2 mais alto quando se compara os transportes de volume das AAIW/SAMW nos experimentos *PiControl* e *Historical*, com os três fluxos combinados (Bombeamento de Ekman, calor e água doce). Todavia, ressalta-se que, no caso da AAIW, o fluxo de calor foi o dominante em relação aos demais, enquanto para a SAMW não houve uma dominância tão clara, com o bombeamento de Ekman apresentando as maiores correlações. Alguns poucos modelos não apresentaram um R^2 significativo como, por exemplo, o *GISS-E2-1-H* para ambas as massas de água, *MRI-CGCM3* para AAIW e *ACCESS-CM2* para SAMW, possivelmente devido a processos oceanográficos intrínsecos que podem afetar a variabilidade dos transportes [[Sallée et al. 2013](#)]. Além disso, o fato de os coeficientes das correlações apresentarem comportamento não-estacionário ao longo do tempo também pode influenciar nos casos de baixas correlações.

Apesar de os modelos estarem superestimando os transportes de água na camada intermediária, eles parecem formar estas massas de água pelas razões corretas. Os modelos, predominantemente, apresentaram coeficientes de regressão de acordo com o que se espera pela teoria da formação das AAIW/SAMW de [Marshall & Radko \[2003\]](#). Eles apresentam maiores transportes de volume concomitantemente com o incremento de estresse dos ventos de oeste e quando há diminuição da flutuabilidade, ou seja, quando aumenta de densidade devido às variações na temperatura e/ou salinidade. Apesar disso, há alta variabilidade entre as magnitudes dos coeficientes quando se compara os resultados de cada modelo.

Analizando os cenários futuros, conclui-se que praticamente todos os fluxos considerados são significantemente impactados no final do século XXI. O teste de tendência não foi significante apenas no caso do fluxo de calor no cenário 4.5 ($p\text{-valor} > 0,05$). Em todos os casos, o cenário 8.5 apresentou as mudanças mais drásticas. O bombeamento de Ekman é intensificado, em módulo, com um acréscimo na média em torno de 1 cm s^{-1} , o fluxo de água doce apresenta um decréscimo, devido ao aumento da evaporação do oceano em um ambiente mais quente e, consistente com isto, o fluxo de calor aumentou de aproximadamente 2,2 para $3,7 \text{ W m}^{-2}$.

Estas mudanças impactam diretamente a formação e a exportação das AAIW e SAMW, com um padrão semelhante, com mudanças mais drásticas sendo observadas no cenário mais catastrófico, mas com padrões variados ao longo dos modelos. Na maioria dos modelos aqui analisados, constata-se um aumento nos transportes nos cenários futuros, mas em alguns casos, houve diminuição nestas exportações, como *MIROC-ESM* e *CanESM5* para AAIW, e *ACCESS-CM2*, *ACCESS-ESM1-5*, *BCC-CSM2-MR*, *CSIRO-Mk3.6.0*, *INM-CM4-8* e *MIROC5* para SAMW. Estudos apontam que as mudanças climáticas parecem intensificar os ventos de oeste, resultando em um maior bombeamento de Ekman na região circumpolar [Goyal et al. 2021]. Porém, também se estima que estes jatos podem ser deslocados mais para sul, o que poderia resultar em menor quantidade de exportação para norte das AAIW/SAMW. Logo, ainda é difícil prever o comportamento destas massas de água, mas elas certamente são impactadas nos futuros cenários.

Neste trabalho também foi testada a capacidade dos coeficientes das regressões dos experimentos *PiControl* e *Historial* replicarem os transportes calculados a

partir das saídas dos modelos nos cenários futuros. As estimativas dos coeficientes apresentaram tendências similares às saídas dos modelos, porém elas não acompanharam as variações inter-anuais, resultando em correlações baixas entre estes resultados. Portanto, conclui-se que estatisticamente os coeficientes não são estacionários. Além disso, estes coeficientes tendem a mudar nos cenários futuros, com os resultados apontando para uma maior importância do fluxo de água doce para a AAIW, superando o calor em dominância. No caso na SAMW, observa-se um aumento da importância de ambos os fluxos de flutuabilidade em ambos cenários futuros.

Após constatada a validade das correlações multivariadas destas forçantes (bombeamento de Ekman, fluxos de calor e água doce) com os transportes das águas da camada intermediária nos modelos CMIP, foi possível utilizar esta mesma metodologia para identificar as regiões do oceano Austral onde estas massas de água estão se formando e como estas áreas podem mudar nos cenários futuros. Para isto, é importante destacar que outros fatores também influenciam nesta formação como, por exemplo, a representação nos modelos da profundidade da camada de mistura no inverno (*Mixed Layer Depth* - MLD), que está diretamente ligada com a intensidade e posição dos ventos de oeste [[Sallée et al. 2012](#)].

Para a identificação destas regiões, primeiro se analisou a variabilidade espacial dos fluxos de interesse, onde foi constatado que todos apresentam uma alta variabilidade meridional no experimento *Historical*, o que resulta em diferentes regiões de formação das AAIW/SAMW. A MLD também varia muito entre os modelos, onde vários apresentam profundidades muito rasas para o inverno austral, problema que persiste das gerações anteriores, como apontado por

[Sallée et al. \[2013\]](#). Porém, alguns possuem profundidades mais condizentes com os valores esperados, como é o caso do ACCESS-CM2, ACCESS-ESM1-5, BCC-CSM2-MR, CMCC-SR5 e UKESM1-0-LL. Neste trabalho, não foi possível identificar as causas que fazem um modelo desempenhar bem em relação a MLD, sendo este um excelente tópico para trabalhos futuros tanto na atual como nas futuras gerações do CMIP.

Neste trabalho, foram consideradas como regiões de formação das AAIW/SAMW as áreas que apresentaram altas correlações multivariadas entre os transportes de volume de água destas massas e os fluxos oceano-atmosfera considerados. Foi encontrado um padrão espacial das correlações bastante semelhante entre ambas massas de água, mas com pequenas diferenças. Como esperado, a SAMW apresentou as regiões de formação levemente ao norte da AAIW, assim como ocorre no oceano real. Estas regiões foram predominantemente o sudeste do oceano Índico, o sul da Nova Zelândia e a região a oeste da Passagem de Drake. Estas áreas estão de acordo com trabalhos prévios que utilizaram dados *in situ* [e.g. [Aoki et al. 2007](#), [Sallée et al. 2010](#)]. Apesar das intensidades dos ventos de oeste, dos fluxos de calor e água doce não serem compatíveis com os valores reais e a subestimação do MLD, seus padrões de distribuição no oceano Austral parecem estar de acordo com o oceano real, o que leva a formação das AAIW/SAMW nas áreas esperadas.

No trabalho de [Sallée et al. \[2010\]](#), foi evidenciado que as regiões de formação das águas intermediárias não necessariamente são as mesmas áreas onde estas massas serão exportadas para norte. No presente trabalho foi exibido o transporte meridional na camada intermediária ao longo de todo o transecto de 30°S, onde foi possível detectar as intensas correntes de oeste predominantes

para sul nos três grandes oceanos e, na borda destas correntes, há fluxos para norte de ambas as massas de água estudadas. Foi possível identificar, também, um fluxo da AAIW no leste do oceano Índico e da SAMW no leste do oceano Atlântico e oeste do Pacífico. A partir destas regiões, estas massas de água irão ventilar a camada intermediária, pelo menos no hemisfério sul, dos três grandes oceanos. Este padrão não é alterado nos cenários futuros, sendo transportado para o norte das mesmas regiões em ambos os cenários analisados, constatando-se apenas pequenas mudanças de intensidade em algumas áreas.

Nos cenários futuros, os padrões das correlações não mudam para as massas de água, sendo as regiões de formação as mesmas em ambos os cenários. Porém, ocorrem alterações nos valores de R^2 , o que pode ser considerado esperado já que, como mostrado anteriormente, os coeficientes não são estacionários e mudam ao longo do tempo. O que surpreende é que essas diferenças podem apresentar sinais diferentes em cada um dos cenários. Para a AAIW, no cenário 4.5, a correlação aumentou em torno de 0,1 nas regiões de formação, enquanto para a SAMW houve um declínio desta mesma correlação. Já no cenário 8.5 ambas as massas de água apresentaram correlações mais baixas quando comparadas às do experimento *Historical*. Sugere-se que as causas disso são as drásticas mudanças nos fluxos, apresentando tendências significativas neste cenário mais catastrófico.

Erros nas representações das águas AAIW e SAMW nos GCMs devem ser considerados ao estudar a influência dos oceanos nas mudanças climáticas. Estudos mostram alguns destes erros nos processos de formação e transformação destas águas como, por exemplo, [Sallée et al. \[2013\]](#) e [Zhu et al. \[2018\]](#). No presente trabalho, também são apontados alguns pontos em que

estas representações ainda necessitam melhorar. Alguns modelos apresentam valores de transporte mais próximos do real, mas é difícil identificar o que faz um modelo desempenhar melhor que outro neste quesito. [Lee et al. \[2011\]](#) mostraram que melhorias nas resoluções espaciais dos modelos podem resultar em uma melhor representação dos fluxos de flutuabilidade e estratificação do oceano Austral. Porém, nas análises aqui realizadas, a resolução não parece ser determinante para a intensidade das correlações, talvez sendo necessário um incremento ainda maior das resoluções para resultarem em melhores resultados na exportação das massas de água estudadas. O presente trabalho também apontou pontos positivos na representação das AAIW/SAMW nos modelos CMIP como, por exemplo, eles estão formando as massas de água pelas razões corretas de acordo com teorias prévias. Além disso, as regiões de formação são bastante acuradas, o que significa que o padrão de distribuição dos fluxos relevantes também está acurado, representando um passo importante no desenvolvimento destes GCMs. Aqui também se destaca a importância dos GCMs, pois o fato dos coeficientes das correlações multivariadas, computados neste trabalho, não serem estacionários implica que previsões do comportamento destes processos não são possíveis com estatística básica, sendo necessários uso destes complexos modelos que levam em conta diversos fatores do sistema climático.

Como resultado final deste trabalho, foi confirmada a hipótese inicial, demonstrando-se que o bombeamento de Ekman e fluxos oceano-atmosfera de calor e água doce, que influenciam a formação e transporte das massas de água AAIW e SAMW, estão sendo significativamente impactados pelas mudanças climáticas em curso. Consequentemente, estas forçantes estão causando

alterações nos transportes de volume destas massas de água levando, potencialmente, a alterações no ciclo natural da circulação oceânica e dos padrões climáticos. Com isto, espera-se ter contribuído com o entendimento dos processos que envolvem a formação e exportação das águas da camada intermediaria do oceano Austral. Mais ainda, devido à importância destas massas de água no balanço climático global, conclui-se ser necessário o continuo acompanhamento das mudanças de suas propriedades, atentando-se para a regionalidade de cada área dos oceanos. Enfim, é esperado que este trabalho contribua para uma melhor performance dos GCM's das próximas gerações e estimativas futuras cada vez mais acuradas.

Capítulo VIII: Recomendações para trabalhos futuros

Neste trabalho foram demonstradas algumas características das massas de água AAIW e SAMW nos modelos CMIP. Foi possível identificar as superestimações de suas exportações, a variabilidade temporal dos fluxos dominantes nestes processos, as principais regiões onde os fluxos impactam nos transportes e as possíveis mudanças para os cenários futuros. Aqui, recomenda-se, para trabalhos futuros que visem estudar as AAIW/SAMW nos modelos CMIP, a estimativa da quantidade de calor e dióxido de carbono que estas massas de água estão carregando para a camada intermediária dos oceanos quando passam pela subducção no oceano Austral. Um balanço médio geral em 30°S destas quantidades é importante para avaliar o equilíbrio do sistema e estimar como isto pode mudar nos cenários futuros. Além disso, em

uma perspectiva regional, é possível identificar quais das regiões apontadas no presente trabalho (Capítulo 7) estão capturando e armazenando maiores quantidades de calor e CO₂, sendo assim chaves para entender a dinâmica climática global. Porém, aqui não foi possível identificar o que faz cada modelo apresentar boas performances relacionados à alguns processos, por exemplo, por que alguns modelos conseguem apresentar MLDs razoáveis enquanto outros superestimam suas profundidades, portanto uma profunda investigação neste sentido se faz necessário.

Portanto, é importante que estas massas de água continuem sendo analisadas nos GCMs e sua representatividade do oceano real então aperfeiçoada pelos grupos modeladores em relação às suas parametrizações. Finalmente, que estas águas sejam continuamente monitoradas *in situ* para possibilitar um maior entendimento de seus processos e uma comparação mais adequada com as saídas futuras simulações do sistema terrestre.

Referências Bibliográficas

Almeida, L., Mazloff, M. R., & Mata, M. M. (2021). The impact of southern ocean ekman pumping, heat and freshwater flux variability on intermediate and mode water export in cmip models: Present and future scenarios. *Journal of Geophysical Research: Oceans*. doi: 10.1029/2021JC017173

Aoki, S., Hariyama, M., Mitsudera, H., Sasaki, H., & Sasai, Y. (2007). Formation regions of subantarctic mode water detected by ofes and argo profiling floats. *Geophysical Research Letters*, 34(10). doi: 10.1029/2007GL029828

AORI, A. (2013). CCSM, NIES, JAMSTEC. WCRP CMIP5: The MIROC team MIROC5 model output collection. *Earth System Grid Federation*. Armour, K. C., Marshall, J., Scott, J. R., Donohoe, A., & Newsom, E. R. (2016). Southern ocean warming delayed by circumpolar upwelling and equatorward transport. *Nature Geoscience*, 9(7), 549–554. <https://doi.org/10.1038/ngeo2731>

Azaneu, M., Kerr, R., & Mata, M. M. (2014). Assessment of the representation of Antarctic bottom water properties in the ECCO2 reanalysis. *Ocean Science*, 10(6), 923–946. <https://doi.org/10.5194/os-10-923-2014>

Beadling, R. L., Russell, J. L., Stouffer, R. J., Goodman, P. J., & Mazloff, M. (2019). Assessing the quality of Southern Ocean circulation in CMIP5 AOGCM

and Earth system model simulations. *Journal of Climate*, 32(18), 5915–5940.

<https://doi.org/10.1175/jcli-d-19-0263.1>

Beadling, R. L., Russell, J. L., Stouffer, R. J., Mazloff, M., Talley, L. D., Goodman, P. J., et al. (2020). Representation of Southern Ocean properties across Coupled Model Intercomparison Project generations: CMIP3 to CMIP6. *Journal of Climate*, 33(15), 6555–6581. <https://doi.org/10.1175/jcli-d-19-0970.1>

Bi, D., Dix, M., Marsland, S., O'Farrell, S., Sullivan, A., Bodman, R., . . . others (2020). Configuration and spin-up of access-cm2, the new generation australian community climate and earth system simulator coupled model. *Journal of Southern Hemisphere Earth Systems Science*, 70(1), 225–251.

Boland, E. J., Jones, D. C., Meijers, A. J., Forget, G., & Josey, S. A. (2021). Local and remote influences on the heat content of southern ocean mode water formation regions. *Journal of Geophysical Research: Oceans*, 126(4).
Doi:46010.1029/2020JC016585

Bracegirdle, T., Holmes, C., Hosking, J., Marshall, G., Osman, M., Patterson, M., & Rackow, T. (2020). Improvements in circumpolar southern hemisphere extratropical atmospheric circulation in CMIP6 compared to CMIP. *Earth and Space Science*, 7. <https://doi.org/10.1029/2019EA001065>

Bracegirdle, T. J., Shuckburgh, E., Sallee, J.-B., Wang, Z., Meijers, A. J. S., Bruneau, N., et al. (2013). Assessment of surface winds over the Atlantic, Indian,

and Pacific Ocean sectors of the southern ocean in CMIP5 models: Historical bias, forcing response, and state dependence. *Journal of Geophysical Research: Atmospheres*, 118(2), 547–562. <https://doi.org/10.1002/jgrd.50153>

Cao, J., Wang, B., Yang, Y.-M., Ma, L., Li, J., Sun, B., Wu, L.(2018). The nuiST earth system model (NESM) version 3: description and preliminary evaluation. *Geoscientific Model Development*, 11(7), 2975–2993.

CCCM, & CCCm. (2015). CANESM2 model output prepared for CMIP5 1pctco₂, served by ESGF. World Data Center for Climate (WDCC) at DKRZ. <https://doi.org/10.1594/WDCC/CMIP5.CCE2c1>.

Cherchi, A., Fogli, P. G., Lovato, T., Peano, D., Iovino, D., Gualdi, S., (2019). Global mean climate and main patterns of variability in the CMCC-CM2 coupled model. *Journal of Advances in Modeling Earth Systems*, 11(1), 185–209.

Collier, M., & Uhe, P. (2012). CMIP5 datasets from the Access1. 0 and Access1. 3 coupled climate models.

Danabasoglu, G., Yeager, S. G., Bailey, D., Behrens, E., Bentzen, M., Bi, D., et al. (2014). North Atlantic simulations in coordinated ocean-ice reference experiments phase II (core-II). Part I: Mean states. *Ocean Modelling*, 73, 76–107. <https://doi.org/10.1016/j.ocemod.2013.10.005>

Danabasoglu, G., Lawrence, D., Lindsay, K., Lipscomb, W., & Strand, G. (2019). NCAR CESM2 model output prepared for CMIP6 historical .Earth System Grid Federation, Version, 20190912, 485.

de Boyer, C. M., Madec, G., Fischer, A. S., Lazar, A., & Iudicone, D (2004). Mixed layer depth over the global ocean: An examination of profile data and a profile-based climatology. *Journal of Geophysical Research: Oceans*, 109(C12).

<https://doi.org/10.1029/2004JC002378>

Dix, M., Bi, D., Dobrohotoff, P., Fiedler, R., Harman, I., Law, R., et al. (2019). CSIRO-ARCCSS access-CM2 model output prepared for CMIP6 CMIP 1pctco2. Earth System Grid Federation. <https://doi.org/10.22033/ESGF/CMIP6.4230>

Downes, S. M., Bindoff, N. L., & Rintoul, S. R. (2010). Changes in the subduction of southern ocean water masses at the end of the twenty-first century in eight ipcc models. *Journal of climate*, 23(24), 6526–6541. doi: 10.1175/2010JCLI3620.1485

Downes, S. M., Langlais, C., Brook, J. P., & Spence, P. (2017). Regional impacts of the westerly winds on southern ocean mode and intermediate water subduction. *Journal of Physical Oceanography*, 47(10), 2521–2530. doi:48810.1175/JPO-D-17-0106.1

Dunne, J., John, J., Adcroft, A., et al. (2014). NOAA GFDL GFDL-ESM2G, ESMhistorical experiment output for CMIP5 AR5, served by ESGF. Earth System Grid Federation. <https://doi.org/10.22033/ESGF/CMIP6.3924>

EC-Earth. (2019). EC-earth-consortium EC-EARTH3-veg model output prepared for CMIP6 CMIP 1pctco2. Earth System Grid Federation. <https://doi.org/10.22033/ESGF/CMIP6.4507>

Eyring, V., Bony, S., Meehl, G. A., Senior, C. A., Stevens, B., Stouffer, R. J., & Taylor, K. E. (2016). Overview of the coupled model inter- comparison project phase 6 (CMIP6) experimental design and organization. Geoscientific Model Development, 9(LLNL-JRNL-736881). <https://doi.org/10.5194/gmd-9-1937-2016>

Ferster, B. S., Subrahmanyam, B., Fukumori, I., & Nyadjro, E. S. (2018). Variability of southern ocean transports. Journal of Physical Oceanography, 48(11), 2667–2688. <https://doi.org/10.1175/jpo-d-18-0055.1>

Gao, L., Rintoul, S. R., & Yu, W. (2018). Recent wind-driven change in subantarctic mode water and its impact on ocean heat storage. Nature Climate Change, 8(1), 49558–63. doi: 10.1038/s41558-017-0022-8

GFDL. (2018). WCRP CMIP5: Geophysical fluid dynamics laboratory (GFDL) GFDL-ESM2M model output collection. Earth System Grid Federation. <http://catalogue.ceda.ac.uk/uuid/bd8dc8fbc4034bde98b108079ee0ec55>

Giorgetta, M., Jungclaus, J., Reick, C., Legutke, V., Brovkin, S., Crueger, T., Esch, M., et al. (2012). CMIP5 simulations of the max Planck institute for meteorology (MPI-M) based on the MPI-ESM-LR model: The historical experiment, served by ESGF. Earth System Grid Federation.
<https://doi.org/10.1594/Wdcc/CMIP5.MXELhi>

Goyal R., Sen Gupta, A, Jucker, M., England, M.H. (2021) Historical and projected changes in the southern hemisphere surface westerlies. Geophysical Research Letters, 48 (4). <https://doi.org/10.1029/2020GL090849>

Griffies, S. M., Danabasoglu, G., Durack, P. J., Adcroft, A. J., Balaji, V., Böning, C. W., et al. (2016). OMIP contribution to CMIP6: Experimental and diagnostic protocol for the physical component of the ocean model intercomparison project. Geoscientific Model Development, 9(9), 3231–3296.
<https://doi.org/10.5194/gmd-9-3231-2016>

Hartin, C. A., Fine, R. A., Sloyan, B. M., Talley, L. D., Chereskin, T. K., & Happell, J. (2011). Formation rates of subantarctic mode water and antarctic intermediate water within the south pacific. Deep Sea Research Part I: Oceanographic Research Papers, 58(5), 524–534. <https://doi.org/10.1016/j.dsr.2011.02.010>

Heuzé, C., Heywood, K. J., Stevens, D. P., & Ridley, J. K. (2013). Southern Ocean bottom water characteristics in CMIP5 models. Geophysical Research Letters, 40(7), 1409–1414. <https://doi.org/10.1002/grl.50287>

Holte, J. W., Talley, L. D., Chereskin, T. K., & Sloyan, B. M. (2013). Subantarctic mode water in the southeast pacific: Effect of exchange across the subantarctic front. *Journal of Geophysical Research: Oceans*, 118(4), 2052–2066. doi:50810.1002/jgrc.20144

Hong, Y., Du, Y., Qu, T., Zhang, Y., & Cai, W.(2020). Variability of the subantarctic mode water volume in the south Indian Ocean during 2004–2018. *Geophysical Research Letters*, 47(10). doi: 10.1029/2020GL087830512

Hong, Y., Du, Y., Xia, X., Xu, L., Zhang, Y., & Xie, S.-P.(2021). Subantarctic mode water and its long-term change in CMIP6 models. *Journal of Climate*, 51434(23), 9385–9400. doi: 10.1175/jcli-d-21-0133.1

Jeffrey, S., Rotstain, L., Collier, M., Dravitzki, S., Hamalainen, C., Moeseneder, C., et al. (2013). Australia's CMIP5 submission using the CSIRO-Mk3.6 model. 63, 1–14. <https://doi.org/10.22499/2.6301.001>

Lee, M.-M., Nurser, A. J. G., Stevens, I., & Sallée, J.-B. (2011). Subduction over the Southern Indian Ocean in a high-resolution atmosphere-ocean coupled model. *Journal of Climate*, 24(15), 3830–3849. <https://doi.org/10.1175/2011JCLI3888.1>

Marshall, J., & Radko, T. (2003). Residual-mean solutions for the Antarctic circumpolar current and its associated overturning circulation. *Journal of Physical Oceanography*, 33(11), 2341–2354. [https://doi.org/10.1175/1520485\(2003\)033](https://doi.org/10.1175/1520485(2003)033)

Mauritsen, T., Bader, J., Becker, T., Behrens, J., Bittner, M., Brokopf, R.,(2019). Developments in the MPI-M earth system model version 1.2 (MPI-ESM1.5) and its response to increasing CO₂. *Journal of Advances in Modeling Earth Systems*, 11(4), 998–1038.

McCartney, M. S. (1977). Subantarctic mode water. *Deep-Sea Research*, 24, 103–119.

McCartney, M. S. (1982). The subtropical recirculation of mode waters. *J. Mar. Res*, 40(427.4), 64.

Meinshausen, M., Smith, S. J., Calvin, K., Daniel, J. S., Kainuma, M., Lamarque, J.-F., et al. (2011). The RCP greenhouse gas concentrations and their extensions from 1765 to 2300. *Climatic Change*, 109(1–2), 213.

<https://doi.org/10.1007/s10584-011-0156-z>

METO, M. O., & Rede Clima, B. N. o. G. C. C. R. (2013). INPE: HadGEM2-ES model output prepared for CMIP5 historical, served by ESGF. World Data Center for Climate WDCC at DKRZ. <https://doi.org/10.1594/WDCC/CMIP5.IEGEHI>

NASA/GISS. (2018). NASA-GISS GISS-E2.1H model output prepared for CMIP6 CMIP piconcontrol. Earth System Grid Federation.

<https://doi.org/10.22033/ESGF/CMIP6.7381>

Naveira Garabato, A. C., Jullion, L., Stevens, D. P., Heywood, K. J., & King, B. A. (2009). Variability of Subantarctic Mode Water and Antarctic Intermediate Water in the Drake Passage during the late-twentieth and early-twenty-first centuries. *Journal of Climate*, 22(13), 3661–3688. doi: 10.1175/2009JCLI2621.1

Pahnke, K., Goldstein, S. L., & Hemming, S. R. (2008). Abrupt changes in Antarctic intermediate water circulation over the past 25,000 years. *Nature Geoscience*, 1(12), 870–874. <https://doi.org/10.1038/ngeo360>

Park, S., & Shin, J. (2019). SNU SAM0-UNICON model output prepared for CMIP6 CMIP piconrol. Earth System Grid Federation. <https://doi.org/10.22033/ESGF/CMIP6.7791>

Rahaman, H., Srinivasu, U., Panickal, S., Durgadoo, J. V., Griffies, S. M., Ravichandran, M., et al. (2020). An assessment of the Indian Ocean mean state and seasonal cycle in a suite of interannual core-II simulations. *Ocean Modelling*, 145, 101503. <https://doi.org/10.1016/j.ocemod.2019.101503>

Rintoul, S. R., & Bullister, J. L. (1999). A late winter hydrographic section from Tasmania to Antarctica. *Deep Sea Research Part I: Oceanographic Research Papers*, 46(8), 1417–1454. [https://doi.org/10.1016/S0967-0637\(99\)00013-8](https://doi.org/10.1016/S0967-0637(99)00013-8)

Rintoul, S. R., & England, M. H. (2002). Ekman transport dominates local air-sea fluxes in driving variability of subantarctic mode water.

Journal of Physical Oceanography, 32, 1308–1321.

[https://doi.org/10.1175/15200485\(2002\)032](https://doi.org/10.1175/15200485(2002)032)

Roemmich, D., Church, J., Gilson, J., Monselesan, D., Sutton, P., & Wijffels, S. (2015). Unabated planetary warming and its ocean structure since 2006. *Nature Climate Change*, 5(3), 240–245. <https://doi.org/10.1038/nclimate2513>

Rong, X. (2019). CAMS CAMS CSM1.0 model output prepared for CMIP6 CMIP 1pctco2. Earth System Grid Federation.

<https://doi.org/10.22033/ESGF/CMIP6.9701>

Sabine, C. L., Feely, R. A., Gruber, N., Key, R. M., Lee, K., Bullister, J. L., et al. (2004). The oceanic sink for anthropogenic CO₂. *Science*, 305(5682), 367–371. <https://doi.org/10.1126/science.1097403>

Sallée, J.B., Wienders, N., Speer, K., & Morrow, R.(2006). Formation of sub-antarctic mode water in the southeastern Indian Ocean. *Ocean Dynamics*, 56(5),558525–542. doi: 10.1007/s10236-005-0054-x

Salle, J. B., Speer, K., Rintoul, S., & Wijffels, S. (2010). Southern ocean thermocline ventilation. *Journal of Physical Oceanography*, 40(3), 509–529.

Salle, J. B., Matear, R., Rintoul, S., & Lenton, A. (2012). Localized subduction of anthropogenic carbon dioxide in the southern hemisphere oceans. *Nature Geoscience*, 5. <https://doi.org/10.1038/NGEO1523>

Salle, J.-B., Shuckburgh, E., Bruneau, N., Meijers, A. J., Bracegirdle, T. J., Wang, Z., & Roy, T. (2013). Assessment of Southern Ocean water mass circulation and characteristics in CMIP5 models: Historical bias and forcing response. *Journal of Geophysical Research: Oceans*, 118(4), 1830–1844.

Sallée, J.B., Shuckburgh, E., Bruneau, N., Meijers, A. J., Bracegirdle, T. J., Wang, Z. (2013b). Assessment of southern ocean mixed-layer depths in cmip5 models: Historical bias and forcing response. *Journal of Geophysical Research: Oceans*, 118(4), 1845–1862. doi: 2169-9275/13/10.1002/jgrc.20157

Sarmiento, J. L., Gruber, N., Brzezinski, M., & Dunne, J. (2004). High-latitude controls of thermocline nutrients and low latitude biological productivity. *Nature*, 570427(6969), 56–60.

Schupfner, M., Wieners, K.-H., Wachsmann, F., Steger, C., Bittner, M., Jungclaus, J., et al. (2019). DKRZ MPI-ESM1.2-HR model output prepared for CMIP6 scenarioMIP SSP126. Earth System Grid Federation.
<https://doi.org/10.22033/ESGF/CMIP6.4397>

Seferian, R. (2018). CNRM-CERFACS CNRM-ESM2-1 model output prepared for CMIP6 CMIP AMIP. Earth System Grid Federation.
<https://doi.org/10.22033/ESGF/CMIP6.3924>

Sen Gupta, A., Santoso, A., Taschetto, A. S., Ummenhofer, C. C., Trevena, J., & England, M. H. (2009). Projected changes to the Southern Hemisphere ocean and sea ice in the IPCC AR4 climate models. *Journal of Climate*, 22(11), 3047–3078. <https://doi.org/10.1175/2008jcli2827.1>

Sloyan, B. M., & Rintoul, S. R. (2001). Circulation, renewal, and modification of antarctic mode and intermediate water. *Journal of physical oceanography*, 31(4), 5791005–1030.

Stramma, L., & England, M. (1999). On the water masses and mean circulation of the South Atlantic Ocean. *Journal of Geophysical Research*, 104(C9), 20863–20883. <https://doi.org/10.1029/1999jc900139>

Swart, N. C., Cole, J. N., Kharin, V. V., Lazare, M., Scinocca, J. F., Gillett, N. P., et al. (2019). CCCMA CANESM5 model output prepared for CMIP6 scenarioMIP SSP126. Earth System Grid Federation. <https://doi.org/10.22033/ESGF/CMIP6.3683>

Talley, L. (1996). Antarctic intermediate water in the South Atlantic. pp. 219–238, Springer.

Talley, L. D. (2003). Shallow, intermediate, and deep overturning components of the global heat budget. *Journal of Physical Oceanography*, 33(3), 530–560. [https://doi.org/10.1175/1520-0485\(2003\)033](https://doi.org/10.1175/1520-0485(2003)033)

Talley, L. D., Reid, J. L., & Robbins, P. E. (2003). Data-based meridional overturning streamfunctions for the global ocean. *Journal of Climate*, 16(19), 3213–3226. [https://doi.org/10.1175/1520-0442\(2003\)016](https://doi.org/10.1175/1520-0442(2003)016)

Tang, Y., Rumbold, S., Ellis, R., Kelley, D., Mulcahy, J., Sellar, A., Jones, C. (2019). Model UKESM1.0-LL model output prepared for CMIP6 CMIP historical. Earth System Grid Federation, 10.

Tatebe, H., & Watanabe, M. (2018). MIROC MIROC6 model output prepared for CMIP6 CMIP historical. Earth System Grid Federation. <https://doi.org/10.22033/ESGF/CMIP6.5603>

Taylor, K. E., Stouffer, R. J., & Meehl, G. A. (2012). An overview of CMIP5 and the experiment design. *Bulletin of the American Meteorological Society*, 93(4), 485–498. <https://doi.org/10.1175/bams-d-11-00094.1>

Tomczak, M. (2007). Variability of Antarctic intermediate water properties in the South Pacific Ocean. *Ocean Science*, 3, 363–377. <https://doi.org/10.5194/os-3-363-2007>

Volodire, A., Sanchez-Gomez, E., y Mlia, D. S., Decharme, B., Cassou, C., Senesi, S., et al. (2013). The CNRM-CM5. 1 Global climate model: Description and basic evaluation. *Climate Dynamics*, 40(9–10), 2091–2121. <https://doi.org/10.1007/s00382-011-1259-y>

Voldoire, A. (2018). CNRM-CERFACS CNRM-CM6-1 model output prepared for CMIP6 CMIP AMIP. Earth System Grid Federation.
<https://doi.org/10.22033/ESGF/CMIP6.3922>

Voldoire, A., Saint-Martin, D., Sénési, S., Decharme, B., Alias, A., Chevallier, M., and others (2019). Evaluation of CMIP6 deck experiments with CNRM-CM6-1. Journal of Advances in Modeling Earth Systems, 11(7), 2177–2213.

Volodin, E. M., Dianskii, N. A., & Gusev, A. V. (2010). Simulating present-day climate with the INMCM4.0 coupled model of the atmospheric and oceanic general circulations. Izvestiya: Atmospheric and Oceanic Physics, 46, 414–431.

<https://doi.org/10.1134/S000143381004002X>

Volodin, E., Mortikov, E., Gritsun, A., Lykossov, V., Galin, V., Diansky, N., et al. (2019). INM INM-CM4-8 model output prepared for CMIP6 CMIP piconet. Earth System Grid Federation. <https://doi.org/10.22033/ESGF/CMIP6.5080>

Wang, Z. (2013). On the response of southern hemisphere subpolar gyres to climate change in coupled climate models. Journal of Geophysical Research: Oceans, 118(3), 1070–1086. <https://doi.org/10.1002/jgrc.20111>

Watanabe, S., Hajima, T., Sudo, K., Nagashima, T., Takemura, T., Okajima, H., et al. (2011). MIROC-ESM: Model description and basic results of CMIP5-20C3M experiments. Geoscientific Model Development Discussions, 4. <https://doi.org/10.5194/gmdd-4-1063-2011>

Wu, T., Chu, M., Dong, M., Fang, Y., Jie, W., Li, J., et al. (2018). BCC BCC-CSM2MR model output prepared for CMIP6 CMIP ESM-HIST. Earth System Grid Federation. <https://doi.org/10.22033/ESGF/CMIP6.2901>

Wunsch, C. (2006). Discrete inverse and state estimation problems: With geophysical fluid applications. Cambridge University Press.
<https://doi.org/10.1017/cbo9780511535949>

Yao, W., & Shi, J. (2017). Pacific-indian interocean circulation of the antarctic intermediate water around south australia. *Acta Oceanologica Sinica*, 36(7), 4–14.606. doi: 10.1007/s13131-017-1078-z

Yukimoto, S., Adachi, Y., Hosaka, M., Sakami, T., Yoshimura, H., Hirabara, M., et al. (2012). A new global climate model of the Meteorological Research Institute: MRI-CGCM3—Model Description and Basic Performance—. *Journal of the Meteorological Society of Japan*, 90A, 23–64. <https://doi.org/10.2151/jmsj.2012-a02>

Yukimoto, S., Koshiro, T., Kawai, H., Oshima, N., Yoshida, K., Urakawa, S., and others (2019). Mri-esm2.0 model output prepared for cmip6. Earth System Grid Federation, available at, 10.

Zhang, J., Wu, T., Shi, X., Zhang, F., Li, J., Chu, M., et al. (2018). BCC BCC-ESM1 model output prepared for CMIP6 CMIP historical. Earth System Grid Federation. <https://doi.org/10.22033/ESGF/CMIP6.2949>

Zhu, C., Liu, Z., & Gu, S. (2018). Model bias for south Atlantic Antarctic intermediate water in CMIP5. Climate Dynamics, 50(9–10), 3613–3624. <https://doi.org/10.1007/s00382-017-3828-1>

Ziehn, T., Chamberlain, M., Lenton, A., Law, R., Bodman, R., Dix, M., et al. (2019). CSIRO access-ESM1.5 model output prepared for CMIP6 CMIP 1pctco2. Earth System Grid Federation. <https://doi.org/10.22033/ESGF/CMIP6.4231>